ORNL/TM-8385

ornl

OAK
RIDGE
NATIONAL
LABORATORY

UNION
CARBIDE

Evaluation of Tubular Ceramic Heat Exchanger Materials in Basic Coal Ash from Coal-Oil-Mixture Combustion

M. K. Ferber
V. J. Tennery

Fossil
Energy
Program

OPERATED BY
UNION CARBIDE CORPORATION
FOR THE UNITED STATES
DEPARTMENT OF ENERGY

Printed in the United States of America. Available from
National Technical Information Service
U.S. Department of Commerce
5285 Port Royal Road, Springfield, Virginia 22161
NTIS price codes—Printed Copy: A06 Microfiche A01

ORNL/TM-8385

METALS AND CERAMICS DIVISION

EVALUATION OF TUBULAR CERAMIC HEAT EXCHANGER MATERIALS IN BASIC COAL ASH FROM COAL-OIL-MIXTURE COMBUSTION

M. K. Ferber and V. J. Tennery

Date Published - October 1982

Work sponsored by the Department of Energy,
Pittsburgh Energy Technology Center

Prepared by the
OAK RIDGE NATIONAL LABORATORY
Oak Ridge, Tennessee 37830
operated by
UNION CARBIDE CORPORATION
for the
DEPARTMENT OF ENERGY
Under Contract W-7405-eng-26

CONTENTS

ABSTRACT 1
INTRODUCTION 2
METHODOLOGY AND MATERIALS 5
RESULTS AND DISCUSSIONS 27
Visual, Dimensional, and Radiographic Examinations 27
Microstructure, Microcomposition, and X-ray Phase Analysis 39
α-SiC 41
CVD and CVR SiC 49
KT, SC-2, and NC 430 SiC 55
AD 998 Al_2O_3 64
Sialon Ceramics 68
Coal Slag 70
Thermal Expansion 75
Helium Permeability 79
FRACTURE STRENGTH 82
SUMMARY AND CONCLUSIONS 86
ACKNOWLEDGMENTS 88
REFERENCES 89

EVALUATION OF TUBULAR CERAMIC HEAT EXCHANGER MATERIALS IN BASIC COAL ASH FROM COAL-OIL-MIXTURE COMBUSTION

M. K. Ferber and V. J. Tennery

ABSTRACT

In a continuing study of the long-term chemical and structural stability of candidate heat exchanger ceramics, tubes of ten different structural ceramic materials were exposed to the hot combustion gases from a coal-oil-mixture (COM) fuel in the Ceramic Recuperator Analysis Facility (CRAF) at an outer tube wall temperature of about 1240°C for about 240 h. Air flow through each tube produced a temperature gradient across and along the tube wall, thereby simulating the conditions in a tubular heat exchanger element. As-received and exposed materials and solidified coal slag were examined by optical microscopy, scanning electron microscopy, electron microprobe, energy-dispersive x-ray analysis, x-ray diffraction, x-radiography, and chemical analysis to identify degradation processes. Several important properties of the ceramics, including room-temperature helium permeability, room-temperature C-ring fracture strength, and thermal expansion from room temperature to 1100°C were measured for both as-received and exposed specimens.

The ten structural ceramics included six types of silicon carbide, a high-purity alumina, and three types of newly available sialons. Highly fluid basic coal slag deposited on the outer surfaces of the structural ceramic tubes during the coal combustion and all of the tubes lost significant fractions of their wall thickness. The extent of wall thinning was highly dependent upon the longitudinal position along the tube axis and the azimuthal angle measured on a plane perpendicular to the tube axis. The greatest loss of tube wall thickness tended to occur within the azimuthal angular range of about 45° centered about the upstream direction, that is, the tube surface normally oriented toward the combustor and about 180 mm from the air-inlet header block. This position was at about 70% of the tube length exposed in the test duct measured from the air-inlet header block. For the ten types of structural ceramics examined, the approximate percentage reduction in wall thickness varied from 78 to 7% on the upstream side of the tubes. Much less wall thinning occurred on the downstream (opposite) side of the tubes. On the upstream tube side,

the three siliconized SiC types exhibited wall thickness reductions from 19 to 33%, while the sintered α-SiC and CVD SiC had values of 16 and about 13% respectively. The CVR SiC had a loss of 7% while the high purity Al_2O_3 tube's value was 15%. The three types of sialon tubes had losses from 19 to 78%.

Exposure to the hot coal slag increased the room-temperature helium permeability of all the surviving tubes by about one order of magnitude. The room-temperature C-ring fracture strength for the five types of SiC and one type of Al_2O_3 ceramic decreased by about 3 to 60% due to the exposure. Siliconized types of SiC had strength reductions of approximately 38 to 61%. Sintered α-SiC showed the smallest strength reduction of 3%. The high purity Al_2O_3 had a strength loss of about 28%.

The corrosion process operative on the outer surface of the SiC tubes included formation of Fe and Ni silicides at the ceramic-slag interface with subsequent transport of the silicides from the interface into the coal-slag layer with resultant formation of pits or channels on the SiC surface. Corrosion of the Al_2O_3 included formation of an iron aluminate spinel layer on the Al_2O_3 tube at the ceramic-slag interface and its subsequent dissolution in the coal slag.

The thermal expansion of these materials did not change significantly due to the slag exposure. Remeasurement of specimens from earlier work (Test 2) showed that indicated expansion increases were artifacts due to the dilatometer used previously.

INTRODUCTION

The continued escalation of fuel costs has resulted in considerable research aimed at increasing fuel-use efficiencies in high-temperature combustion systems. Since fuel consumption decreases directly with increasing temperature of the combustion air used in the burners, substantial fuel savings can be realized by employing fixed-boundary heat exchangers (HXs) or recuperators to preheat the air.[1] Analyses[2,3] have shown that fuel consumption can be reduced by about 40% using recuperation to provide air preheat temperatures of 800°C or greater. Consequently, waste heat recovery from hot furnace gases in industries such as steel, aluminum, and glass provides an excellent opportunity for use of advanced

HX materials. Currently, most recuperator materials are restricted to metal alloys which are limited to operating temperatures of 800 through 900°C by oxidation and mechanical property constraints. Furthermore, the increased use of impure fuels such as residual oils by the process heat industries and process carry over in the combustion gases has led to additional corrosion problems in these alloy materials.[1] An alternative is to use selected structural ceramics which typically exhibit better corrosion resistance and strength at higher temperatures than current engineering alloys.

There has also been considerable interest in using high-efficiency energy conversion cycles to produce electricity from domestic fuels such as coal. These advanced fossil energy systems typically rely upon the direct firing of a gas turbine with fossil fuel combustion products. However, the use of relatively dirty fuels in gas turbine systems exposes the high-temperature alloys in the turbine to corrosive environments unless the combustion gas is cleaned thoroughly prior to its entry into the turbine. Extensive work in the United States in the past four years has shown cleanup to be a formidable task. A promising alternative to the direct-fired turbine is a high-temperature HX to isolate the hot gas turbine from the combustion gases. A pressurized secondary working fluid such as air, helium, or argon would be heated by the HX and then used to operate the turbine. This mode of operation requires HX materials that are corrosion resistant when exposed to highly reactive coal slags. These materials must also maintain sufficient strength to resist fracture under stresses generated from either the temperature differentials across the HX partition or the large internal secondary gas pressures.[4] Preliminary analyses of such systems indicate that turbine working fluid temperatures of at least 1000°C are required to provide attractive cycle conversion efficiencies. When combined with the corrosive nature of the coal combustion environment, these temperature levels preclude consideration of all known alloys. Consequently, structural ceramic materials such as those based upon SiC and Al_2O_3 appear to have significant potential for use in HXs in these advanced fossil energy systems.

One major limitation preventing the wide-scale use of structural ceramics in HX applications involving coal combustion has been the lack of information pertaining to the high-temperature chemical and physical stability of ceramic materials in the presence of corrosive coal slags. In response to this fundamental need, a program was established at ORNL with the expressed goal of better understanding the high-temperature behavior of structural ceramics in coal-slag combustion environments. In the initial studies, state-of-the-art ceramic materials were exposed for approximately 500 h to the combustion products of a No. 6 fuel oil. This test, which was conducted in the Ceramic Recuperator Analysis Facility (CRAF) at ORNL and designated as CRAF Test 1 (ref. 6), provided the necessary baseline data for these materials. In CRAF Test 2 (ref. 5), selected ceramic specimens were exposed again for about 500 h to the combustion products of an acidic-ash coal carried in a coal-oil mixture (COM). The COM was used as a convenient means for burning the coal in the CRAF burner. It should also be noted that the coal was chosen primarily on the basis of its ash chemistry since this chemistry ultimately dictated the corrosive nature of the coal-slag. In both tests, ambient air was forced through the ceramic tubular specimens to simulate thermal conditions for actual HX elements operating in a cross-flow arrangement. Changes in individual samples resulting from the exposure to the combustion environment were detected by conducting a thorough characterization of both the as-received and exposed materials. The characterization techniques included microstructural and x-ray phase analysis plus measurements of the thermal expansion, fracture strength, and helium permeability.

This report describes the results of CRAF Test 3 in which several candidate ceramic materials were exposed to the combustion products of a basic coal carried in a Venezuelan crude-derived No. 6 fuel oil. The materials included two tubes each of KT SiC and α-SiC (Carborundum); SC-2 SiC and AD-998 Al_2O_3 (Coors); plus one tube each of CVD SiC (Deposits and Composites); CVR SiC (Syntax); three types of sialon ceramics (GE-128, GE-129, and GE-130) (General Electric); and an NC-430 SiC tube (Norton) containing a proprietary butt-joint at tube midspan. During the exposure,

which lasted for approximately 240 h, the tubes were maintained at a nominal temperature of 1230°C.

METHODOLOGY AND MATERIALS

The CRAF is a unique facility dedicated to long duration exposures of candidate HX materials to hot combustion gases of fossil fuels. This unit is mounted on top of a furnace called the Refractory Test Facility (RTF), a refractory-lined test chamber fired with a forced-draft oil burner (Fig. 1). The RTF has a maximum thermal rating of 0.9 MW which is of a scale comparable to smaller combustor systems of interest for advanced fossil energy conversion systems. Details of the CRAF and RTF are given elsewhere.[4,5,6]

As noted previously, a total of 14 tubes of various structural ceramics was employed in CRAF Test 3: 2 tubes each of KT SiC, α-SiC, SC-2 SiC, and Al_2O_3 plus 1 tube each of CVD SiC, CVR SiC, three types of sialon ceramics, and an NC-430 SiC containing a butt-joint at tube midspan. A summary of all CRAF Test 3 tubular elements, their pretest dimensions, and the respective material's vendor appears in Table 1 while the various tubes (except the CVD SiC) are illustrated in Fig. 2. The large variability in the as-received dimensions of the ceramic tubes is quite evident. It would have been desirable to obtain tubes of more similar dimensions. However, for materials such as the sialon type, the time required to obtain tubes of more optimum dimensions would have resulted in delivery times in excess of program schedule constraints. Finally, the relatively large standard deviation values associated with the dimensional measurements of the CVD SiC, CVR SiC, and the three sialon tubes reflect the inherent problems existent with the fabrication technology of tubular elements of these ceramic materials. If these materials are to be considered for future HX applications, fabrication techniques for the preparation of long tubular elements must be more fully developed.

With the exception of the SC-2 SiC, CVR SiC, and the three sialons, complete descriptions of all materials listed in Table 1, including the

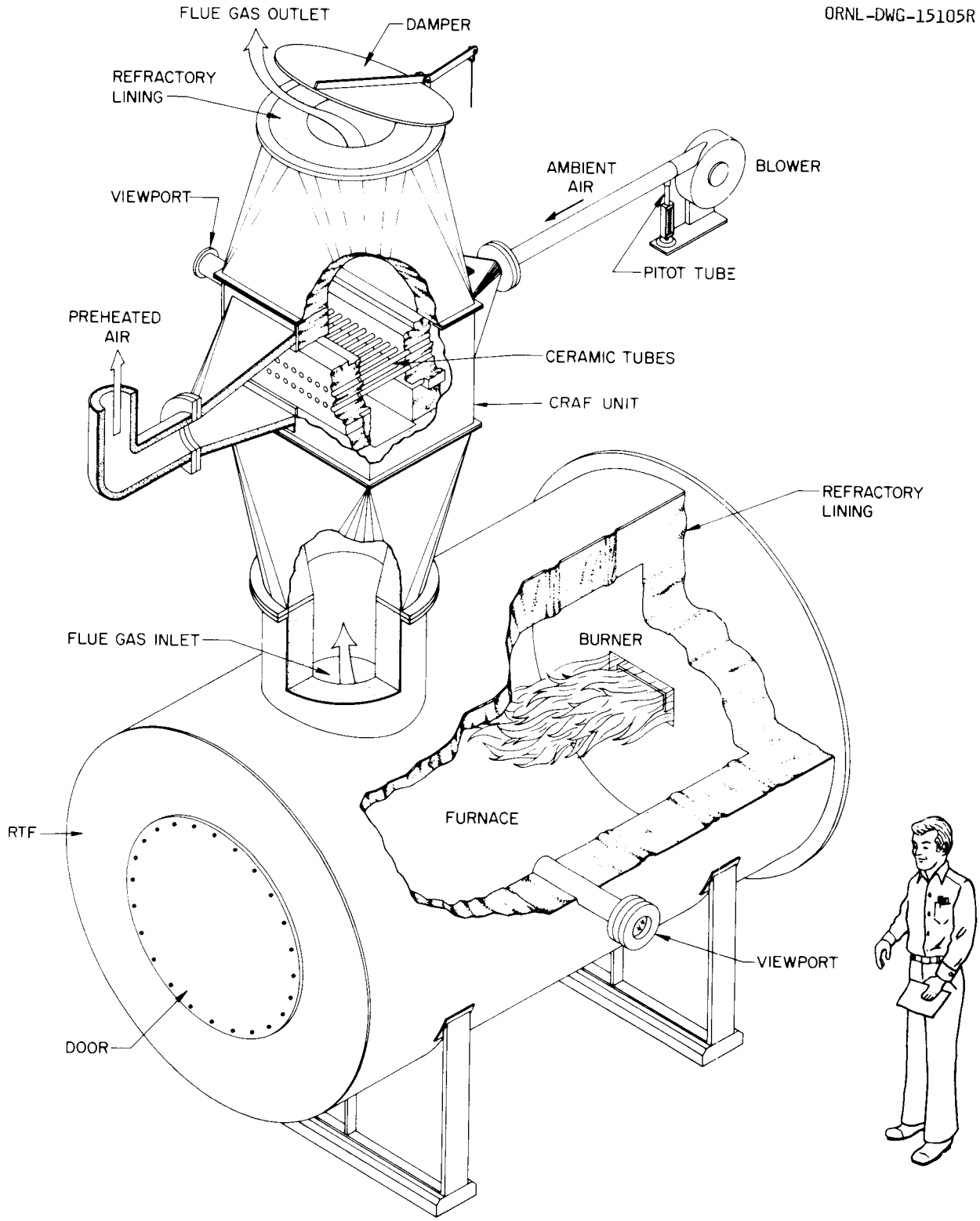

Fig. 1. Ceramic Recuperator Analysis Facility mounted on the Refractory Test Facility.

Table 1. Materials, dimensions, and sources of ceramic tubes exposed in CRAF Test 3

Materials	Tube designation	Dimensions, mm[a]			Source
		Length	OD[b]	ID[b]	
Siliconized SiC	1(a) KT SiC-1	308.3	26.05 ± 0.08	13.38 ± 0.10	1. Carborundum Co., Niagara Falls, N.Y.
	(b) KT SiC-2	306.2	26.10 ± 0.12	19.53 ± 0.14	
	2(a) SC-2 SiC-1	253.3	25.49 ± 0.09	19.24 ± 0.12	2. Coors Porcelain Co., Golden, Colo.
	(b) SC-2 SiC-2	253.3	25.23 ± 0.10	19.32 ± 0.09	
	3 NC 430 joint	304.8	25.07 ± 0.06	17.22 ± 0.13	3. Norton Co., Worcester, Mass.
Pressureless sintered SiC	(a) α-SiC-1	304.0	25.39 ± 0.06	18.66 ± 0.19	Carborundum Co., Niagara Falls, N.Y.
	(b) α-SiC-2	304.0	25.35 ± 0.06	18.67 ± 0.15	
High-purity alumina	(a) AD 998-1	304.8	25.11 ± 0.05	19.23 ± 0.17	Coors Porcelain Co., Golden, Colo.
	(b) AD 998-2	305.1	25.07 ± 0.05	19.53 ± 0.20	
Chemically vapor-deposited SiC	CVD SiC	320.0	24.90 ± 2.29	18.72 ± 0.18	Deposits and Composites, Herndon, Va.
Chemically vapor-reacted SiC	CVR SiC	306.4	26.30 ± 0.38	18.01 ± 0.53	Syntax Corp., Bay City, Mich.
Sialon	(a) GE-128	209.5	24.92 ± 0.46	17.76 ± 1.02	General Electric Co., Philadelphia
	(b) GE-129	223.5	26.87 ± 0.53	18.37 ± 0.66	
	(c) GE-130	219.9	28.30 ± 0.99	18.60 ± 0.99	

[a]Measurements of the outer and inner diameters (OD and ID, respectively) were made at both ends of each tube.

[b]The first number represents the average of at least six measurements, and the second number is the standard deviation.

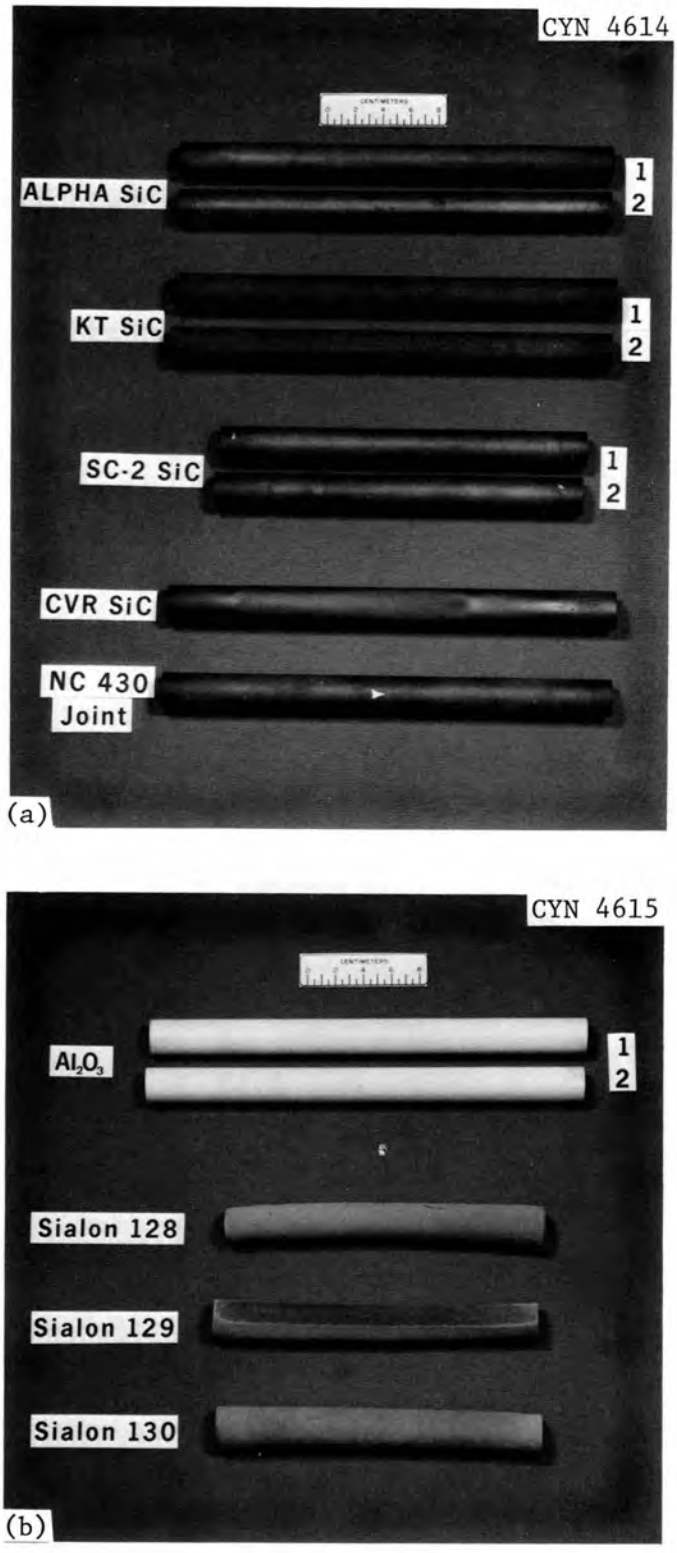

Fig. 2. Macroscopic views of tubes used in CRAF Test 3. (a) As-received SiC. (b) Al_2O_3 and sialon.

fabrication techniques, have been given elsewhere.[5,6] The SC-2 SiC is a siliconized silicon carbide quite similar to KT, NC 430, and Refel* SiC. Consequently, its microstructure consists primarily of silicon carbide in a silicon matrix. The CVR SiC is a new experimental material prepared by reacting silicon with a graphite mandrel at 1800°C and applying a layer of CVD SiC over the inner and outer tube surfaces.

The three sialon materials are based on compositions within the silicon-aluminum-oxygen-nitrogen system. In particular, they are composed primarily of β′-sialon which is a solid solution between Al_2O_3 and Si_3N_4.[7,8] Furthermore, these sialon ceramics can be fabricated into dense ceramics using conventional sintering techniques as long as a liquid phase is present at the sintering temperature. This can be accomplished by using formulations within the system Si_3N_4-SiO_2-Al_2O_3-AlN since these result in the presence of a liquid phase in equilibrium with β′-sialon at temperatures above 1700°C. Alternatively, additions of metal oxides such as MgO to the above formulation can react with the β′ constituent to form a liquid phase at a lower firing temperature. However, since these liquids can degrade the high-temperature properties of the ceramic, their presence must be minimized during the final stages of the densification process. Typical formulations for the GE-128, -129, and -130 sialons are given in Table 2.

Table 2. Typical formulations for the GE-128, -129 and -130 sialons

Sialon designation	Composition, wt%						
	Si_3N_4	Al_2O_3	AlN	SiO_2	CaO	MgO	Residual[a]
128	64.0	26.0	8.3	0.9	0.1	0.6	0.1
129	83.0	13.0	2.0	0.9	0.1	0.6	0.4
130	87.0	10.0	1.0	0.9	0.1	0.6	0.4

[a]Minor impurities often include Fe_2O_3 and TiO_2.

*Supplied by Pure Carbon Co., St. Marys, Penn.

The 14 pretest tubes were mounted in ceramic headers constructed of a high-alumina castable refractory. The openings in the ceramic headers were approximately 2-mm oversized in diameter and length to accommodate thermal expansion of the tubes. Tube-to-header sealing was accomplished using densely packed aluminosilicate fiber seals. Because the sialon and SC-2 SiC tubes were shorter than the 254-mm-width of the test duct, they were inserted, telescope fashion, into KT SiC sleeves (44.5-mm OD × 31.8-mm ID × 152.4-mm long) which in turn were mounted into the headers. In order to monitor the temperatures at the outer surfaces of the tubes, Pt vs Pt-10% Rh thermocouples were attached at the midspan of each tube on the downstream side (surface facing away from the burner). This thermocouple configuration is shown in Fig. 3(a). In addition, three holes were drilled in the α-SiC (tube 2) so that temperatures at the outer surface and near the inner tube wall could be measured at three positions along the downstream surface of the tube [(Fig. 3(b)]. The values of L_1, L_2, L_3, and L_o were 68.6, 149.9, 220.9, and 254 mm, respectively. This latter thermocouple configuration allowed measurement of the temperature gradients in the tubes resulting from the internal air flow during the actual high-temperature exposure. All thermocouples were protected from flue gas impurities by AD 998 alumina protection tubes and a high purity alumina cement applied to the junctions.

Figure 4 shows the downstream side of the tube-header array including the thermocouples prior to the installation of the array upon the RTF. The α-SiC tube with the special thermocouple configuration is also partially visible. Figure 5 illustrates the upstream side of the array mounted on the RTF prior to the installation of the top assembly onto the CRAF. During CRAF Test 3, the upstream surfaces of the tubes were the first to be contacted by the combustion products. In addition, secondary air supplied by an auxiliary fan flowed through the tubes during the exposure so that they operated as HX elements in a cross-flow mode (Fig. 6). The air velocity was measured with a Dwyer* pitot tube located in the 100-mm-ID pipe running from the exit of the secondary blower to the air inlet transition of the CRAF. The temperature of the preheated

*Product of Dwyer Instruments, Inc., Michigan City, Ind.

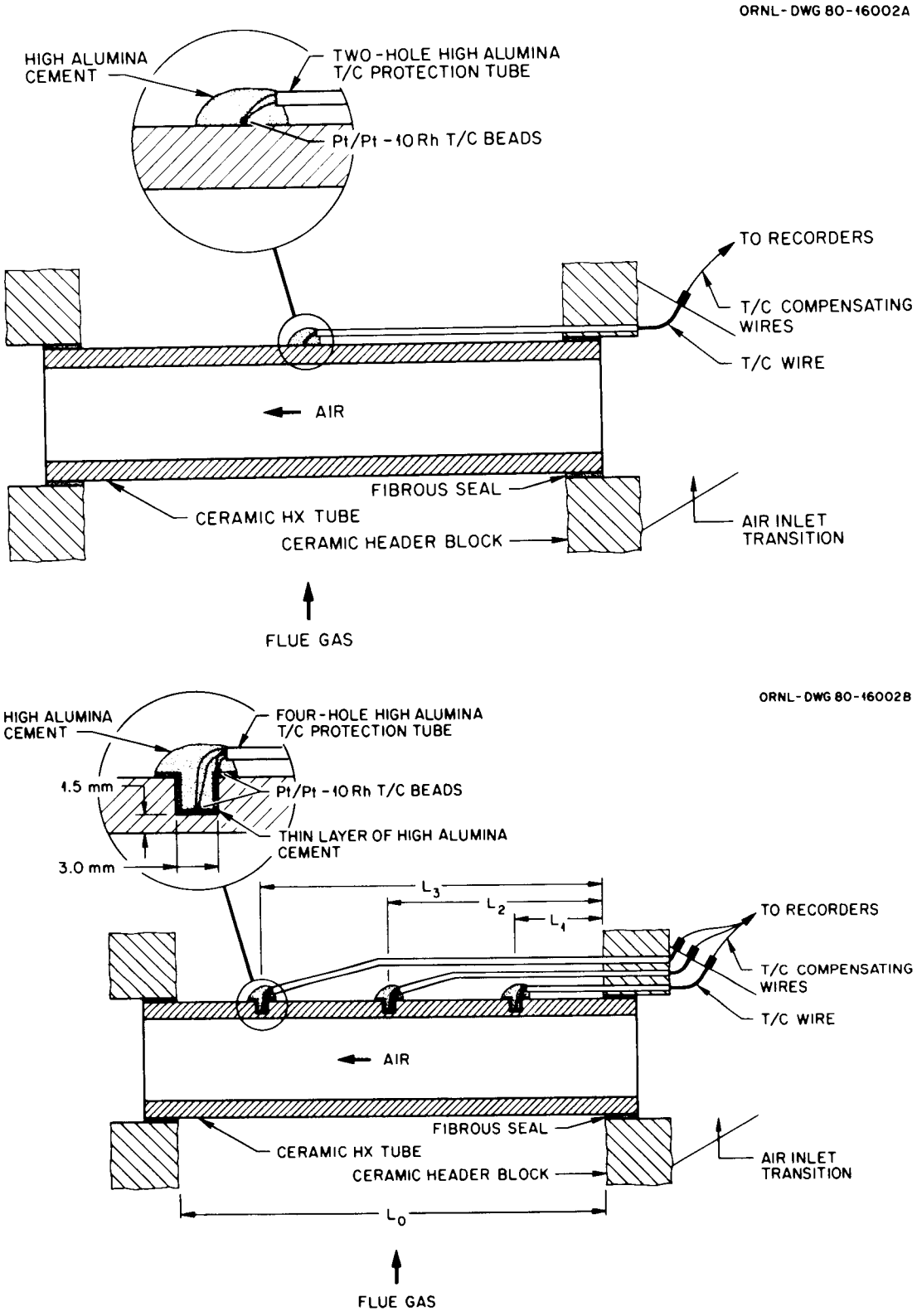

Fig. 3. Thermocouple configuration used to measure (a) downstream surface temperatures of tubular elements and (b) profiles along tube length and across tube wall in α-SiC.

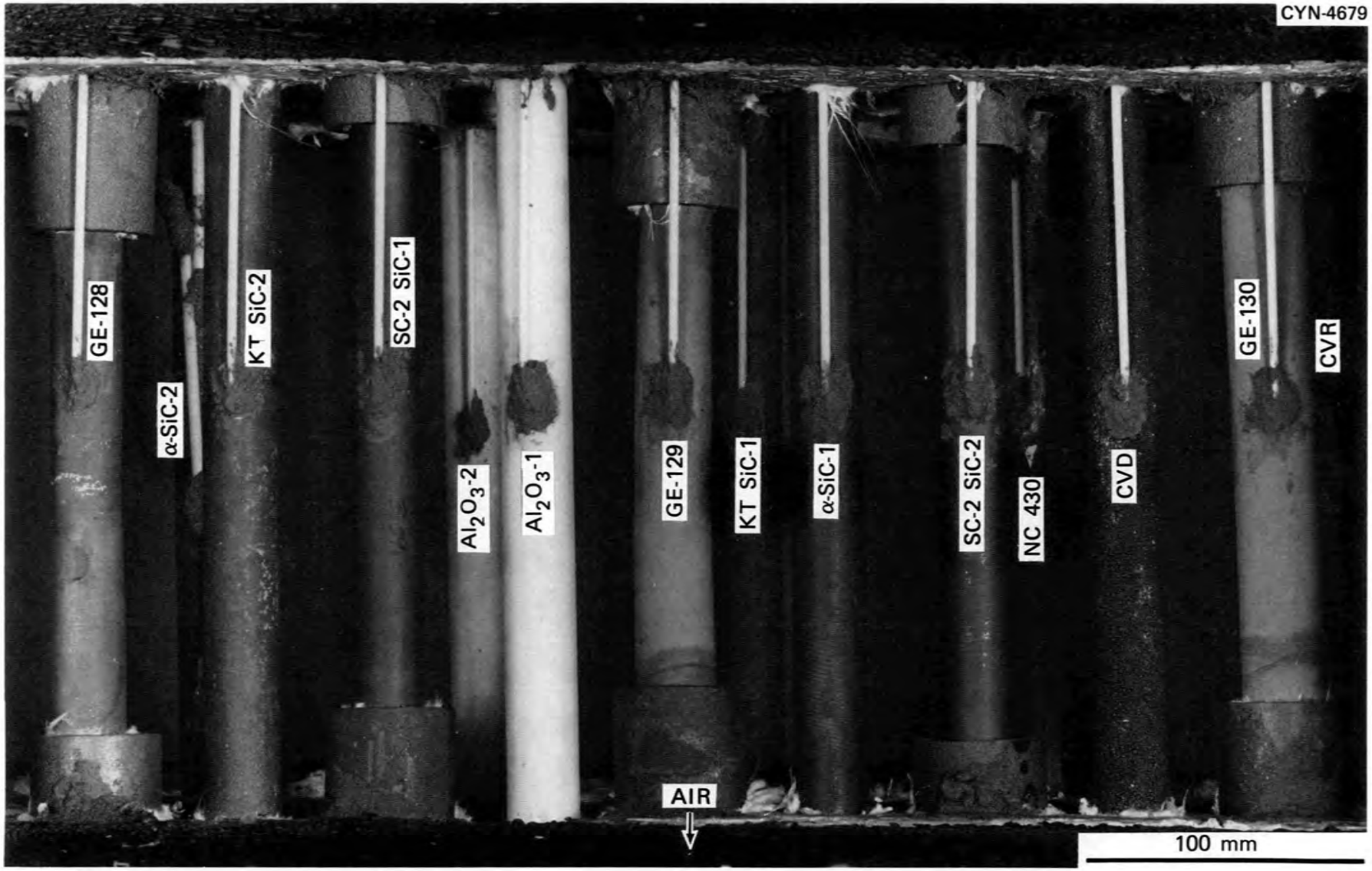

Fig. 4. Downstream side of pretest ceramic tubes before mounting on the flue gas duct of the Refractory Test Facility.

Fig. 5. Upstream surface of pretest ceramic tubes mounted in flue gas duct on the Refractory Test Facility. Flue gas flow direction into the page.

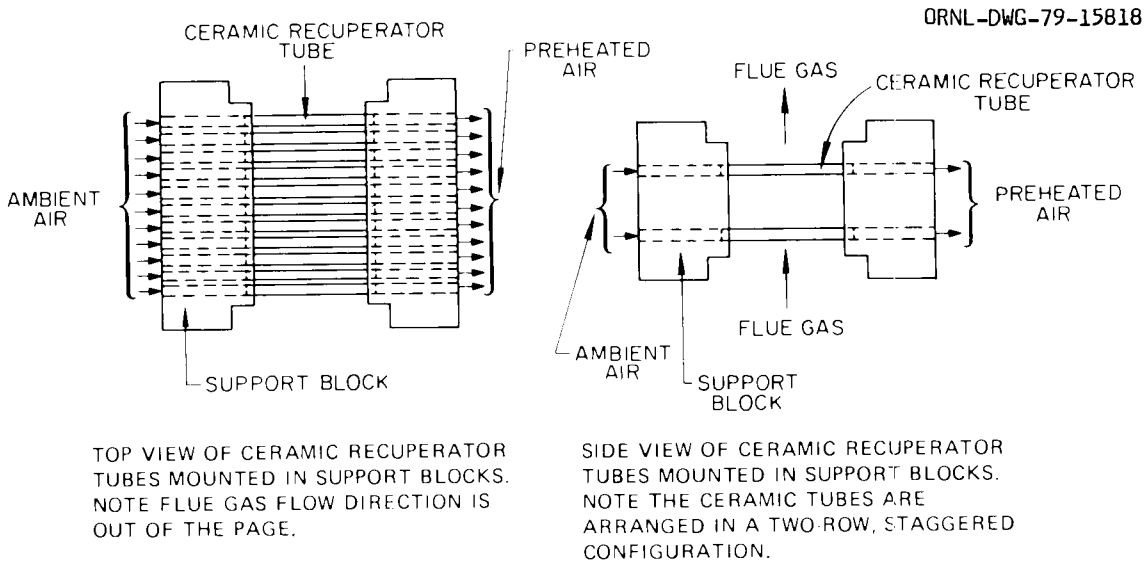

Fig. 6. Ceramic heat exchanger tubes mounted in ceramic support blocks.

secondary air exiting the tubes was measured with a water-cooled, radiation shielded suction pyrometer. This instrument, which was also used to measure the flue gas inlet and outlet temperatures, included a collection system for the flue gas condensables and noncondensables present in the flow path. Complete details are given elsewhere.[5,6]

The fuel used in the RTF was a COM which consisted of 20 wt % powdered coal in a Venezuelan crude-derived No. 6 fuel oil. The COM was used as a convenient means for burning coal in the existing burner in the RTF. This technique was quite successful in CRAF Test 2 in which the COM was a 10 wt % powdered bituminous coal in a Venezuelan No. 6 fuel oil.[5] The results of a chemical analysis of the coal used in the present study are given in Table 3. The coal was finely divided with 99.2% of the particles being smaller than 44 μm. The coal ash contained high concentrations of the equivalent oxides SiO_2, Fe_2O_3, Al_2O_3, CaO, and MgO. The relatively large quantities of CaO and MgO resulted in a fairly high base-to-acid ratio of 1.14. Consequently, the coal ash was expected to be quite fluid at the exposure temperatures achieved in CRAF Test 3. This expected behavior sharply contrasts with that obtained in CRAF Test 2 in

which the combustion of an acidic ash coal (base-to-acid ratio of 0.29) resulted in the formation of a very viscous refractory coal slag at the exposure temperature.

Table 3. Chemical analysis of coal in CRAFT Test 3 coal-oil mixture[a]

	Constituent	Equivalent oxide	wt%
Overall analysis	C		72.05
	S		0.62
	Ash		5.55
	Water		0.00
Ash analysis		SiO_2	24.47
		Fe_2O_3	8.87
		Al_2O_3	12.81
		CaO	25.12
		MgO	8.35
		SO_3	15.35
		P_2O_5	0.53
		Na_2O	0.76
		K_2O	0.42
		TiO_2	0.77
		SrO	0.14
		BaO	0.26
		Mn_3O_4	0.11
		Base/acid[b]	1.14

[a]Analysis provided by vendor.

[b]The base-to-acid ratio is defined as $(Fe_2O_3 + CaO + MgO + Na_2O + K_2O)/(SiO_2 + Al_2O_3 + TiO_2)$.

During this exposure experiment, the furnace was first heated to 770°C with natural gas and then to approximately 1440°C with the COM fuel at an average heating rate of 0.026°C/s (95.3°C/h). This resulted in a heating rate of about 0.024°C/s (87.5°C/h) in the vicinity of the tubes and a maximum tube temperature of 1230°C. However, the average tube temperature increased slightly with increasing exposure time due to a reduction in the secondary air velocity through the tubes. The corresponding temperature-time plots for the RTF furnace and tube array are shown in Figs. 7 and 8, respectively. Only two minor temperature excursions were encountered during the pumping and firing of the COM fuel. First, the RTF pump malfunctioned at about 13 h into the test resulting in a temperature drop of approximately 112°C in the vicinity of the tubes. Second, a temporary reduction in the flow of steam used to heat the COM fuel prior to

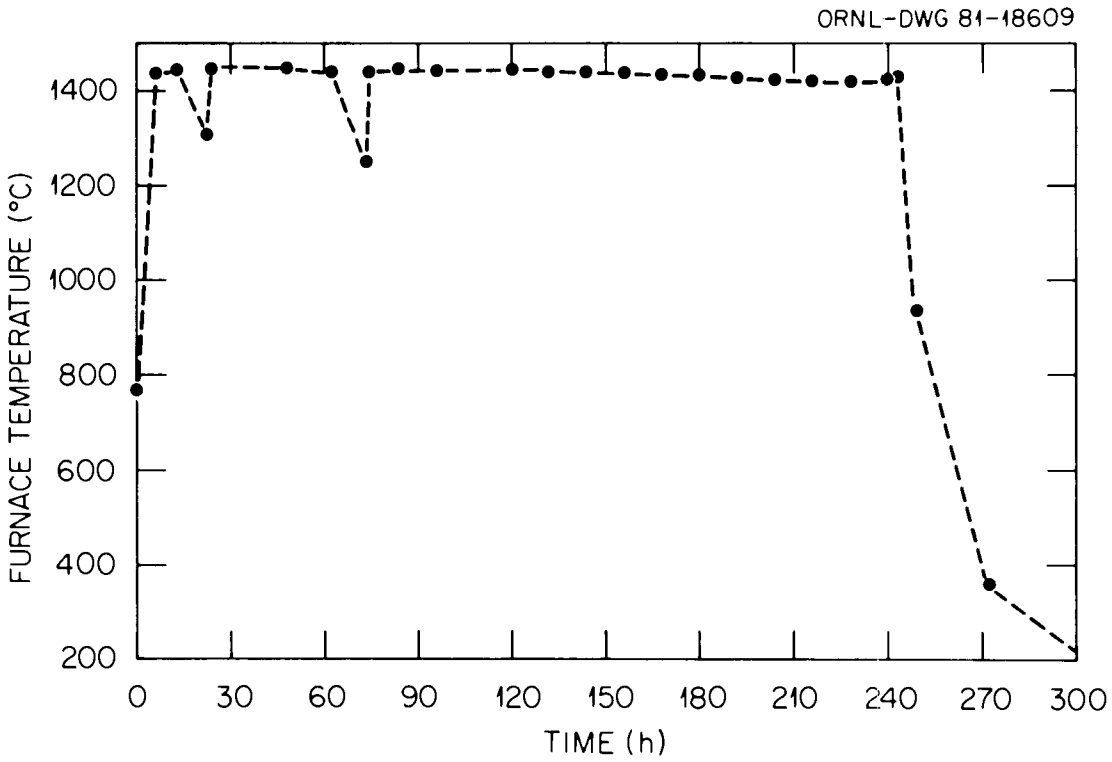

Fig. 7. Furnace temperature versus time showing minor temperature excursions in CRAF Test 3.

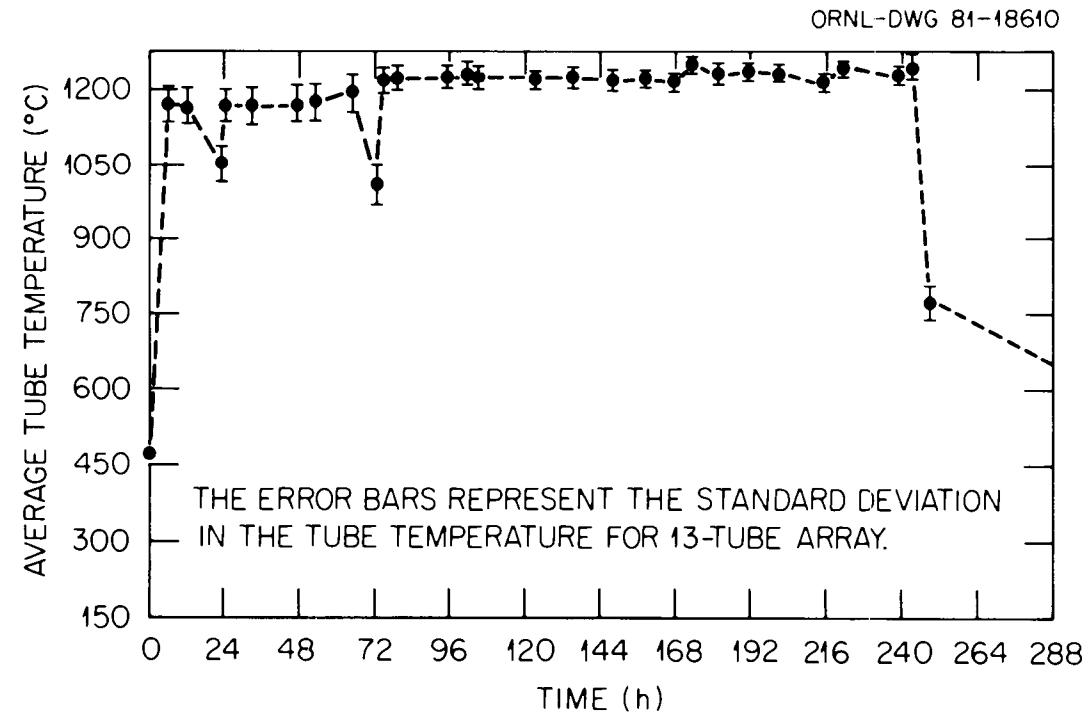

Fig. 8. Average tube temperature versus time showing the two thermal cycles experienced by tubular elements.

combustion led to a similar temperature reduction after about 66 h. Since the cooling rates experienced during those two excursions were fairly small, it is unlikely that the tubes were damaged due to thermal shock. Finally, as indicated in Figs. 7 and 8, the total exposure time at the maximum tube temperature was 240 h. During this time, approximately 16 m^3 (4200 gal) of COM fuel, including 3900 kg of coal and 214 kg of ash, were burned at a rate of 0.066 m^3/h (17.4 gal/h).

The temperatures in Fig. 8 represent the average values of outer surface temperatures measured at tube midspan along the downstream side. However, temperature gradients actually existed across the tube walls and along the length of the tubes due to the combined effects of heat transfer and secondary air flow. The nature of these gradients at two exposure times are illustrated for the α-SiC (tube 2) in Fig. 9. The variations between the two sets of temperature gradient profiles primarily reflect differences in the secondary air velocity (18.0 m/s at 55.9 h and 13.7 m/s at 101 h). For example, at a given position along the tube length, the

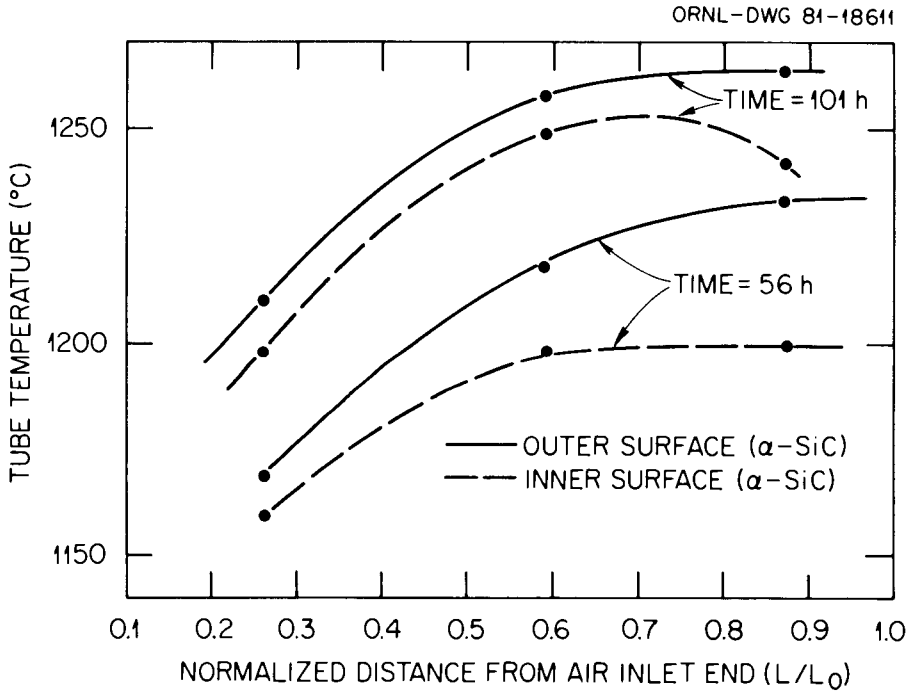

Fig. 9. Temperature profiles measured for α-SiC at two different exposure times.

temperature gradient across the wall was larger at the higher air velocity. This effect would be anticipated on the basis of increased heat flow across the wall at the greater internal air velocity. One would also expect the resulting thermal stresses to be significantly larger for this situation.

Visual observations of the tubular specimens during the exposure revealed the formation of a fluid coal-slag coating on all tubes after about 15 h. These coal-slag deposits formed a thin continuous layer on the downstream side of the tubes and a rather nonuniform coating on the upstream surfaces. This latter situation was apparently due to the disruption of the upstream slag layer by the direct impingement of the flue gas stream. Small liquid hemispherical-shaped coal-slag nodules were also present on the upstream tubular surfaces. Many of these nodules were observed to increase in size and then drip from the tubes indicating that the nodules were quite fluid at the CRAF Test 3 exposure temperature. The coal-slag features are illustrated for exposure times of 50 and 222 h in Figs. 10 and 11, respectively. Although the thickness of the slag covering on the tube surfaces did not change appreciably with increasing exposure time, there appeared to be more gas generation within the coal-slag deposits at the longer times as evidenced by the large number of small bubbles present in the slag in Fig. 11.

The temperatures of the flue gas entering and leaving the CRAF test section, the air temperature entering and leaving the tubes, and the air velocity were measured four times during the exposure. The results are summarized in Table 4. Also included are values for the effectiveness of the HX tube array, the heat transfer rate, and the heat flux through the tube walls. The actual calculations were based on the analyses given in ref. 2. The data in Table 4 illustrate the importance of the secondary air velocity upon the HX effectiveness, which is the ratio of the actual heat transferred by the HX tube array to the maximum amount of available heat. Although the heat transfer rate increased with increasing air velocity within the tubes, the HX effectiveness decreased, apparently due to a reduction in the time available for heat transfer between the hot flue gas and a given volume of air. Consequently, the effectiveness increased as

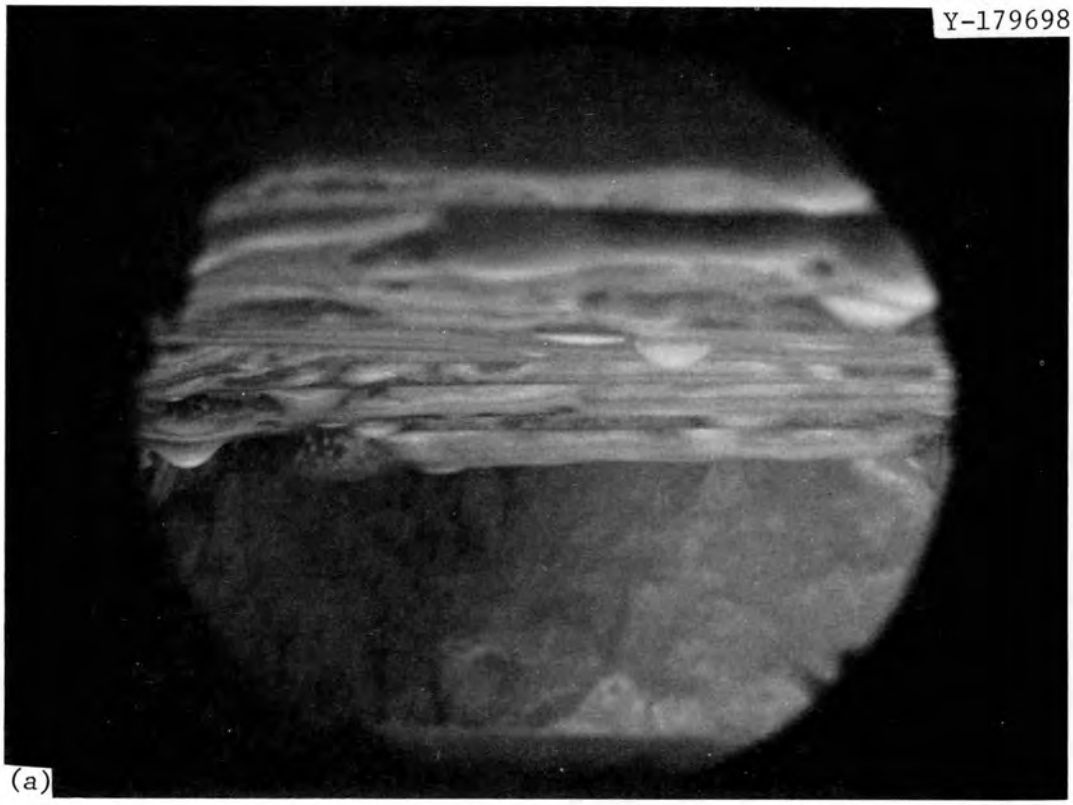

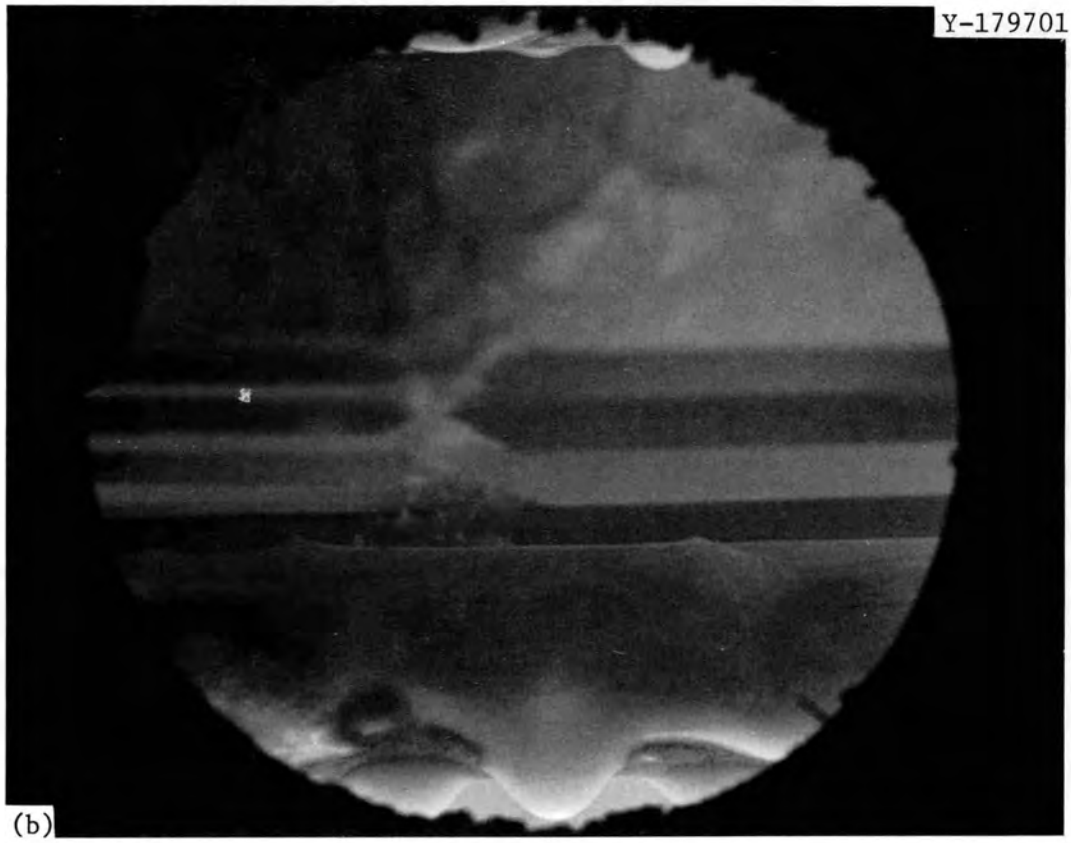

Fig. 10. Ceramic tubes at temperature after 50-h exposure showing coal-slag deposits. (a) Upstream side of upper tube row. (b) Downstream side of lower tube row.

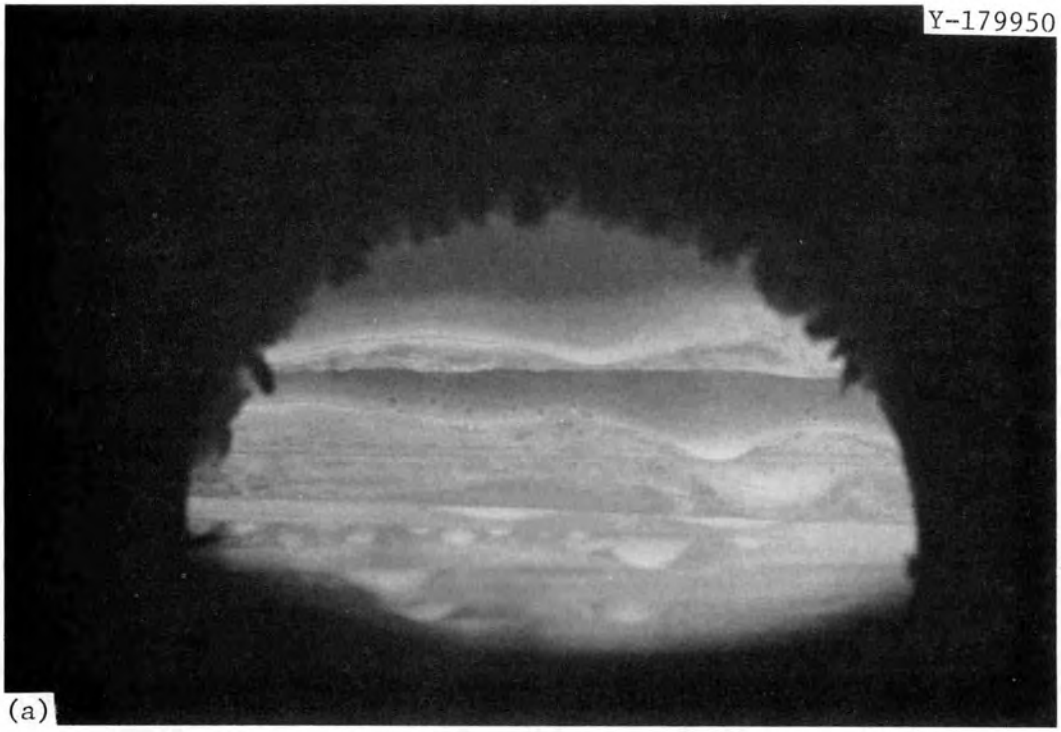

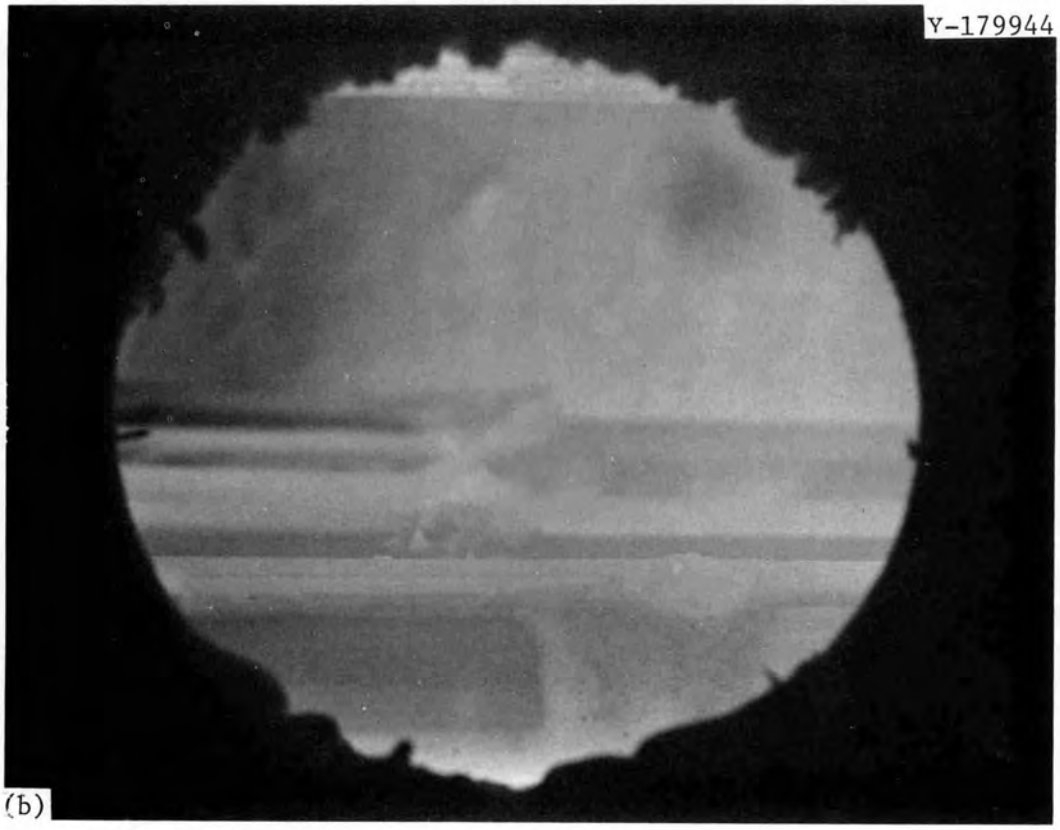

Fig. 11. Gas bubbles in slag deposits on ceramic tubes at temperature after 222-h exposure. (a) Upstream side of upper tube row. (b) Downstream side of lower tube row.

the air velocity was reduced within the range of values employed in this experiment. No attempt was made to optimize the HX effectiveness in CRAF Test 3, since the major purpose of this experiment was to evaluate the structural ceramics in the hot coal combustion environment.

Table 4. Calculated values of HX effectiveness, heat transfer rate, and heat flux at several exposure times

	Total tube exposure time, Ms (h)			
	0.19 (54)	0.37 (102)	0.62 (173)	0.80 (220)
Flue gas inlet, °C	1365.0	1389.0	1458.0	1418.0
Flue gas outlet, °C	1252.0	1290.0	1390.0	1378.0
Air inlet, °C	32.2	41.5	37.1	47.0
Air outlet, °C	275.0	327.0	360.0	353.0
Air velocity, m/s (ft/min)	18.0 (3550)	13.7 (2700)	11.6 (2290)	10.9 (2150)
HX effectiveness	0.18	0.21	0.23	0.22
Heat transfer rate kW (Btu/h)	32.9 (112×10^3)	29.4 (100×10^3)	25.6 (87×10^3)	23.7 (81×10^3)
Heat flux, kW/m^2	68.5	61.2	53.3	49.4
($Btu/in.^2h$)	(150)	(134)	(116)	(109)

The results of the chemical analyses of the COM fuel and the condensable flue gas samples, which were collected during the measurement of the flue gas inlet temperature, are given in Table 5. Since the individual elemental concentration did not vary significantly in specimens taken at various exposure times, only average concentrations are shown. The large quantities of Si, Fe, Al, and Ca present in both the condensable matter and COM fuel were probably associated with the coal ash while the high vanadium concentation came from the No. 6 fuel oil.[5] A comparison of the

Table 5. Results of chemical analyses of COM sample and flue gas condensables

Element	Average concentration, wt ppm	
	COM fuel[a]	Flue gas condensables[b]
Si	74	major
Fe	160	3000
Al	650	700
Ca	140	7000
Mg	53	900
S	1.27%	7000
P	88	400
Na	86	200
K	20	300
Ti	4.6	[c]
V	39	2000
Ni	34	300
Cr	3.1	300
Co	1.1	4
Cu	0.6	40
Mn	1.2	200
Pb	0.1	20
Zn	3.6	50
Zr	[c]	3
Ba	63	300
B	[c]	100
Sr	2.4	60

[a]Atomic absorption chemical analysis by Technical Laboratory, Chattanooga, Tenn.

[b]Spark source mass spectroscopy by Analytical Chemistry Division, ORNL.

[c]Not analyzed.

relative coal ash constituents reported by the vendor (Table 3) with those in Table 5 reveals some striking variations. For example, the ratios Si/Fe, Si/Al, and Si/Ca vary considerably in the three analyses. One would expect better agreement between the COM elemental analysis and the coal ash analysis in Table 3. This discrepancy suggests that inherent problems existed in the analytical measurement technique. However, the variations between the concentrations in the flue gas condensables and those in the COM may also be partly due to selective removal of certain elements from the flue gas during the combustion process.

Noncondensable flue gas samples were also collected during the measurement of the flue gas inlet temperatures. The average results of gas chromatographic analyses performed on samples collected at several exposure times are given in the following table. Approximately 15 vol % excess oxygen was present in the vicinity of the tubular elements which is comparable with environmental conditions in CRAF Tests 1 and 2.

Gas-chromatographic analysis of noncondensables

Component	Vol. %
O_2	15.1
N_2	80.6
CH_4	<0.02
CO	<0.02
CO_2	4.4

The as-received ceramic materials were characterized using techniques outlined in Table 6. The visual examinations and dimensional measurements provided an indication of any bulk changes in the ceramic tubes resulting from the long term exposure to the COM fuel combustion.

The as-received ceramic materials were characterized using techniques outlined in Table 6. The visual examinations and dimensional measurements provided an indication of any bulk changes in the ceramic tubes resulting from the long term exposure to the COM fuel combustion.

The radiographic examinations, microstructural characterization, x-ray

diffraction, and the analyses of microcomposition were used to determine physical and chemical changes in the tubular materials which could adversely affect their performance as structural HX materials. The details of the procedures and sample preparations required for these techniques are well established and, therefore, not reported here.

Table 6. List of analyses used to characterize the structural materials

A. Visual examination
B. Dimensional measurements
C. Radiographic nondestructive examinations
D. Helium permeability
E. Microstructural characterization
1. SEM
2. Optical microscopy (metallography)
F. X-ray diffraction
G. Microcomposition
1. Wet chemical analysis
2. Spark source mass spectroscopy
3. Fast neutron activation analysis
4. SEM energy dispersive X-ray analysis
H. Thermal expansion
I. Mechanical strength

The characterization also involved the determination of the helium permeability, thermal expansion, and C-ring fracture strength using specimens cut from both as-received and exposed tubes. The measurement of these properties, all of which constitute critical factors in the design of ceramic HXs, is discussed in detail elsewhere.[5,6]

The visual observations, dimensional measurements, radiographic examinations, and helium permeability measurements were made using the actual tubes subsequently employed in the CRAF for the 240-h exposure. However, the determination of the microstructural, x-ray diffraction,

microcompositional, thermal expansion, and mechanical strength characteristics of the pretest materials required the use of representative archive tubular samples since these procedures are destructive in nature. The detailed sectioning plans for the pre- and post-test analyses are outlined in Figs. 12 and 13, respectively. For the post-test sectioning, the C-ring strength specimens were oriented so that fracture occurred in

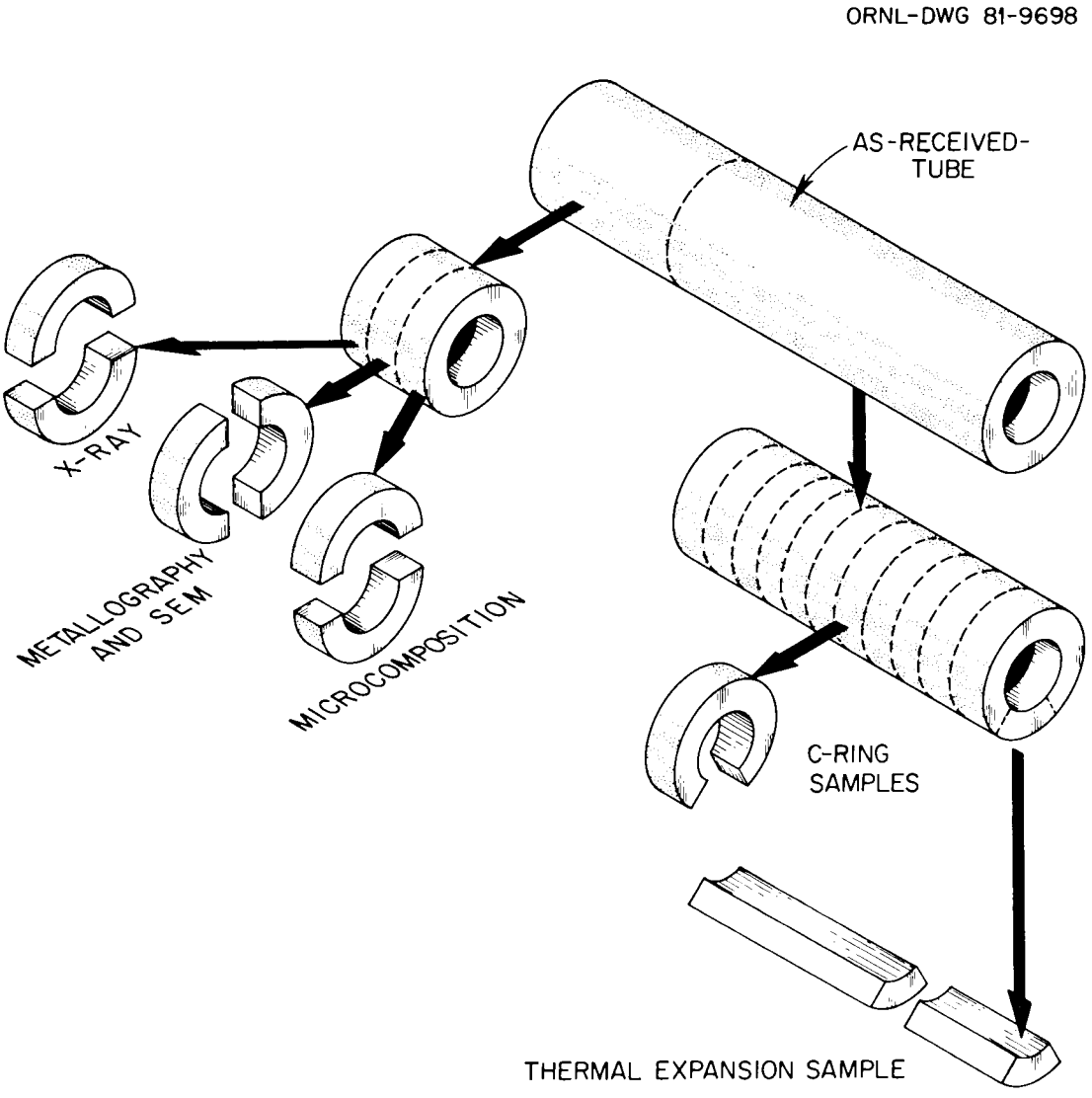

Fig. 12. Typical sampling plans for pretest characterization.

ORNL-DWG 81-18990

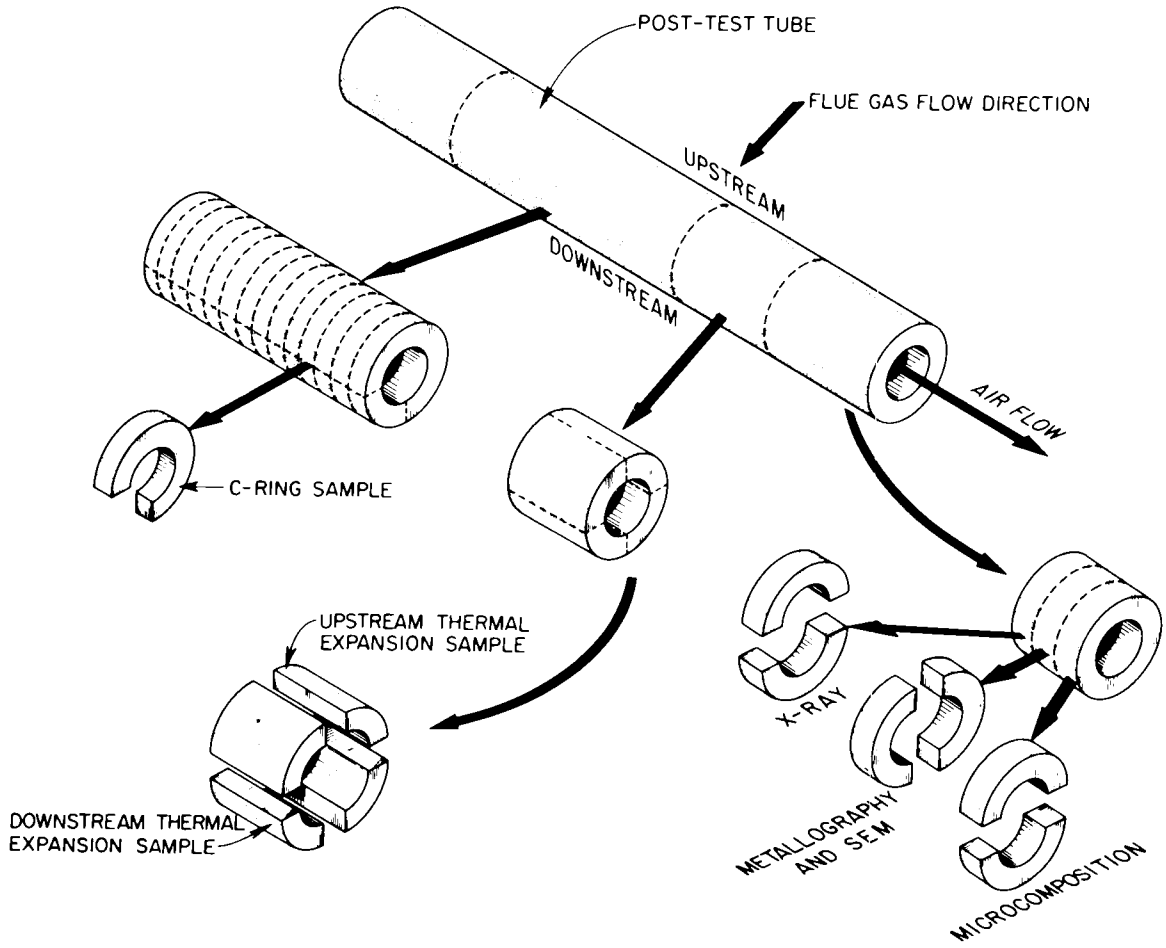

Fig. 13. Sampling plans for post-test characterizations.

the upstream region. Thermal expansion samples were prepared from both the upstream and downstream regions in an effort to detect differences in the extent of the ceramic-slag reaction. Analyses E–G (Table 6) were also used to characterize the coal-slag deposits remaining on the exposed tubes.

RESULTS AND DISCUSSION

VISUAL, DIMENSIONAL AND RADIOGRAPHIC EXAMINATIONS

All tubes except the CVD SiC were characterized before combustion-gas exposure by x-radiography. The results indicated the possible existence of several surface voids in the GE-128 sialon tube. In addition, there was considerable variation in the wall thickness of all three sialon specimens. The variations were apparently related to difficulties encountered during the fabrication of these tubular materials. In the case of the CVR SiC, the material density in the middle of the tube was substantially greater than that at the tube ends. A second phase material was also present along the inner wall of the tube, and its thickness increased significantly at the tube center. The radiographic examinations also revealed a longitudinal seam along one of the alumina tubes, which may have formed during the fabrication. Finally, excess material was observed along the inner wall of the NC 430 SiC tube in the vicinity of the joint. This material, which was relatively distinct from the bulk phase comprising the tube, was presumably used in the joining process. No visible defects were detected in any of the remaining tubes.

The tube-header array was visually examined following the exposure and subsequent cool down to ambient temperature. The upstream view of the tube-header array in Fig. 14 clearly shows the residual slag nodules that formed during the exposure (Figs. 10 and 11). For most tubes, these nodules which were located in the upstream surface region were displaced slightly toward the tube sides. This effect was apparently due to the combined effects of the aerodynamic forces exerted by the flue gas upon the fluid coal slag nodules and the gravitational effects. Figure 15, which illustrates the downstream view of the tubes in the header blocks, indicates that for most post-test tubes the residual, downstream-slag layer was considerably more uniform than that on the upstream side. As previously stated, this behavior was probably due to the fact that, during

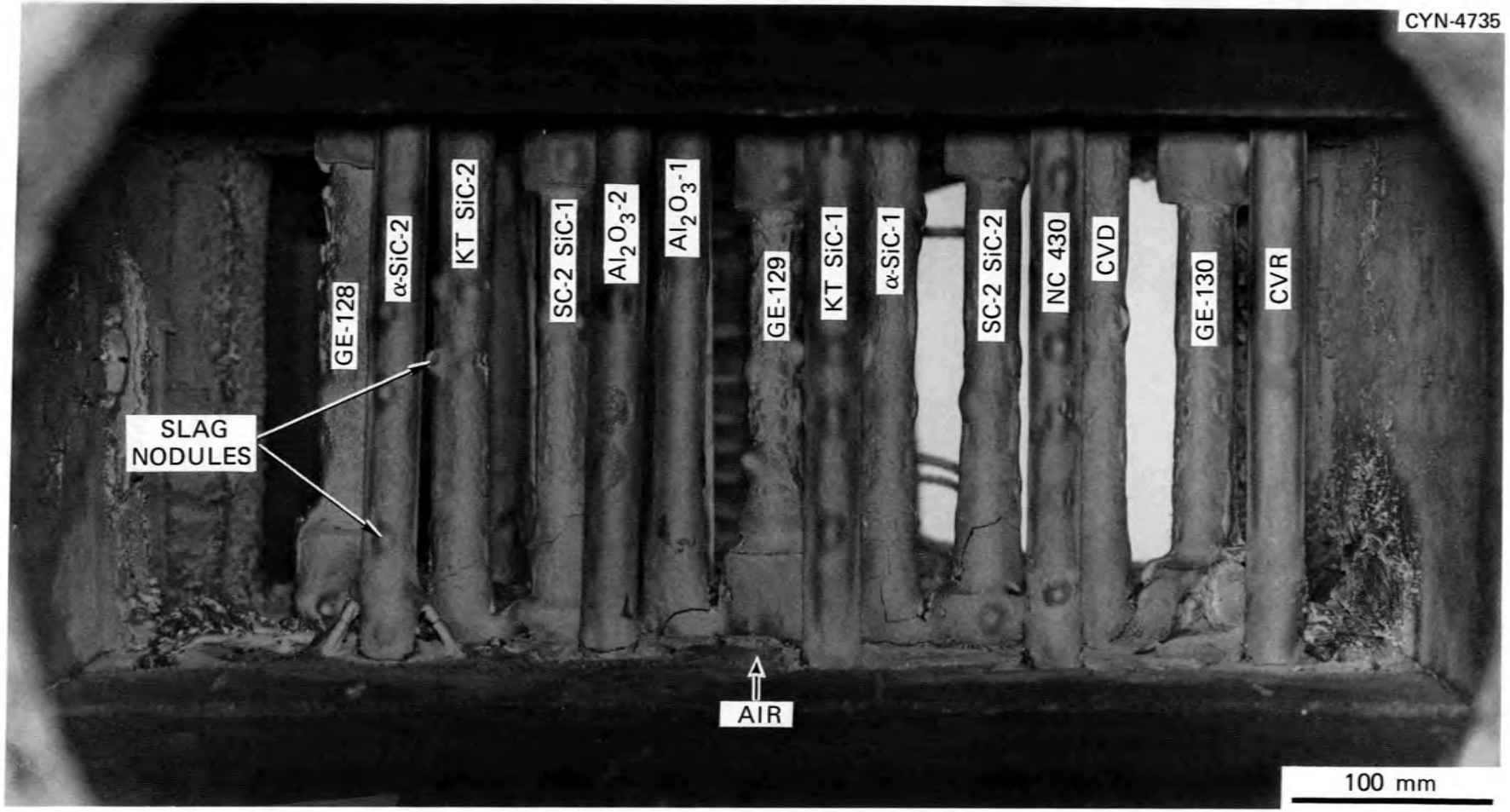

Fig. 14. Post-test tube array illustrating residual slag nodules on upstream surfaces of ceramic tubes after long-term exposure.

Fig. 15. Post-test tube array illustrating condition of downstream surfaces of ceramic tubes after long-term exposure.

the exposure, the downstream surfaces were shielded from direct impingement of the flue gas particles. Consequently, the flow and spreading processes occurring in the downstream slag were not severely perturbed by the flue gas during the exposure.

Following the visual observations of the tube-header array, the tubes were removed from the header blocks. The GE-128 sialon and SC-2 SiC (tube 2) specimens fractured upon their removal suggesting that cracks had formed in the respective tubes as a result of thermal stresses generated during the 240-h exposure. All surviving tubes, as well as unfractured portions of the GE-128 sialon and SC-2 SiC tubes, were examined using x-radiography. The CVD SiC tube was found to contain a longitudinal crack that ran almost the entire length of the downstream surface. Since subsequent visual observations of the tube interior gave evidence of coal-slag penetration along the flaw surface, the crack probably formed during the early stages of the exposure. The radiographic analyses also revealed various amounts of corrosion loss (wall thinning) in the GE-128, GE-129, CVD SiC, NC 430 SiC, KT SiC (tube 2), Coors SC-2 SiC (both tubes), and an α-SiC (tube 2). The corrosion loss tended to be greater at very specific locations along the upstream surface near the air outlet end. However, in the KT SiC (both tubes), α-SiC (tube 2), CVR SiC, NC 430 SiC, GE-129, and GE-130 a significant degree of wall thinning occurred around the entire circumference. The radiographic examinations of several coal slag deposits revealed the presence of a considerable number of internal voids within many of the slag nodules along the upstream surface. In addition, small spherical deposits (less than 2 mm in diameter) were observed in the slag coating remaining on most of the silicon carbide tubes.

Visual examinations of the individual tubular elements indicated that the morphology of the coal slag deposited upon the silicon carbide and alumina tubes had several distinguishing characteristics. For example, the downstream slag layer, which was typically 0.5 to 1.0 mm in thickness, generally ranged in color from dark brown (for the Al_2O_3 tubes) to greenish yellow (for the siliconized silicon carbides). In

addition, coal slag deposits in the vicinity of the thermocouple junctions often exhibited a dark brown color which may have resulted from a reaction between the coal slag and the alumina cement used to attach the thermocouple. The downstream slag surface often was characterized by a rough texture and significant amounts of entrapped porosity. This slag was fairly resistant to removal by finger pressure, even on the SiC-based ceramics. Examination of the upstream tubular surfaces indicated that the coal slag was thicker in two longitudinal strips which were typically located along either side of the centerline of the upstream surface. These strips usually ranged in thickness from 2 to 3 mm. The larger droplet like slag nodules, which were previously observed in Figs. 10 and 11, were randomly positioned along these coal slag strips. Closer examination of several fractured nodules revealed the presence of significant internal porosity which agrees with the x-radiographic results. Consequently, it is possible that gas generation, perhaps due to chemical reactions between the hot slag and the ceramic, may have facilitated the formation of the slag nodules at the exposure temperature of 1230°C. Finally, the upstream tube surface between the longitudinal strips of thicker coal slag contained a 0.3 to 1.0 mm thick layer of poorly adherent coal slag.

An idealized view of the typical coal slag morphology described above is illustrated in Fig. 16. Again, it is important to note that the regions of thicker slag deposits (strips) did not occur along the lowest portion of the tube but were displaced toward the sides. A similar behavior is often observed in metal boiler tubes when subjected to corrosive coal slags.[9] Further examples of the slag morphology are given in Fig. 17 which shows the upstream and downstream characteristics of the post-test KT and SC-2 tubes. Both the slag strips and droplet like nodules can be clearly observed in the upstream view [Fig. 17(a)]. Alternately, the downstream view of the four tubes [Fig. 17(b)] reveals a fairly uniform slag layer except in regions adjacent to the thermocouple junction. The dark coloration of the slag on these areas (KT SiC - tube 1) again suggests that a reaction occurred between the coal-slag

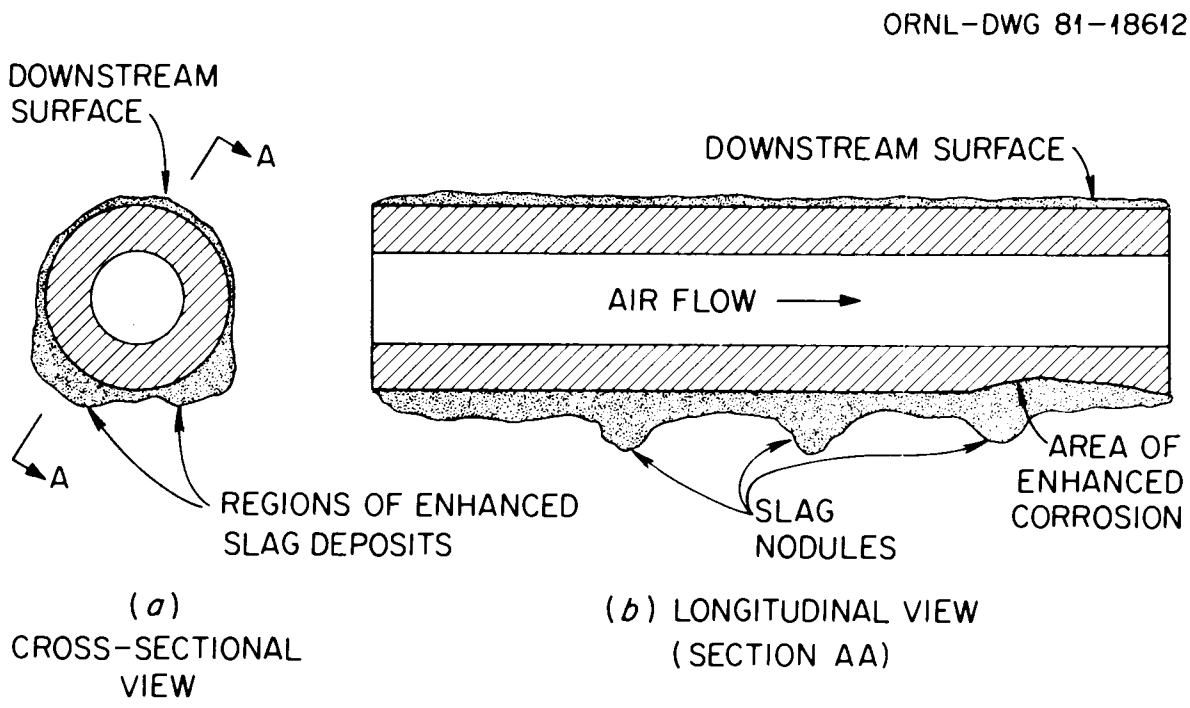

Fig. 16. Schematic representation of post-test slag morphology observed on silicon carbide and alumina tubes. (a) Typical cross section. (b) Longitudinal section parallel to AA.

constituents and the cement used to join the thermocouple junction to the tube. The photographs in Fig. 17 also indicate that there was considerable slag bridging between the outer surface of the SC-2 SiC (tube 1) and the support collar of KT SiC on the air outlet end. This bridging agrees with previous observations of the high fluidity of the coal slag during the high-temperature exposure. The aforementioned circumferential corrosion can be seen in the upstream surface of the KT SiC [tube 1 in Fig. 17(a)]. This enhanced wall thinning, which is further illustrated by the cross-sectional view in Fig. 18, may have resulted from the high temperatures near the air outlet end (Fig. 9). Since, as shown later, the degradation in the silicon carbide materials was dominated by chemical reactions at the ceramic-slag interface, one would expect an exponential dependence upon temperature.

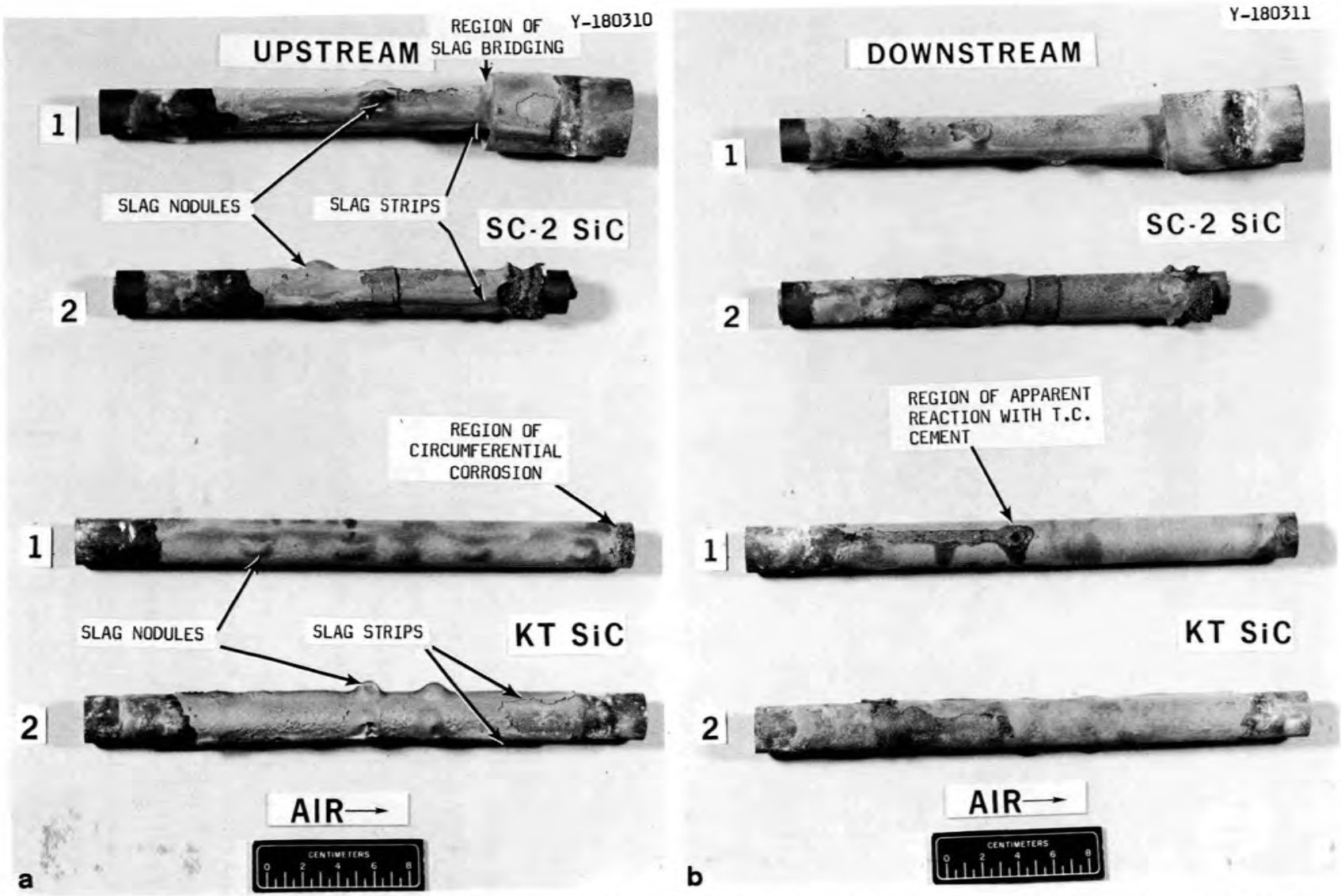

Fig. 17. Typical slag deposits on siliconized SiC tubes. (a) Upstream side of post-test KT SiC and SC-2 SiC showing residual slag morphology. (b) Downstream side of post-test KT SiC and SC-2 SiC revealing region of possible reaction between slag and thermocouple.

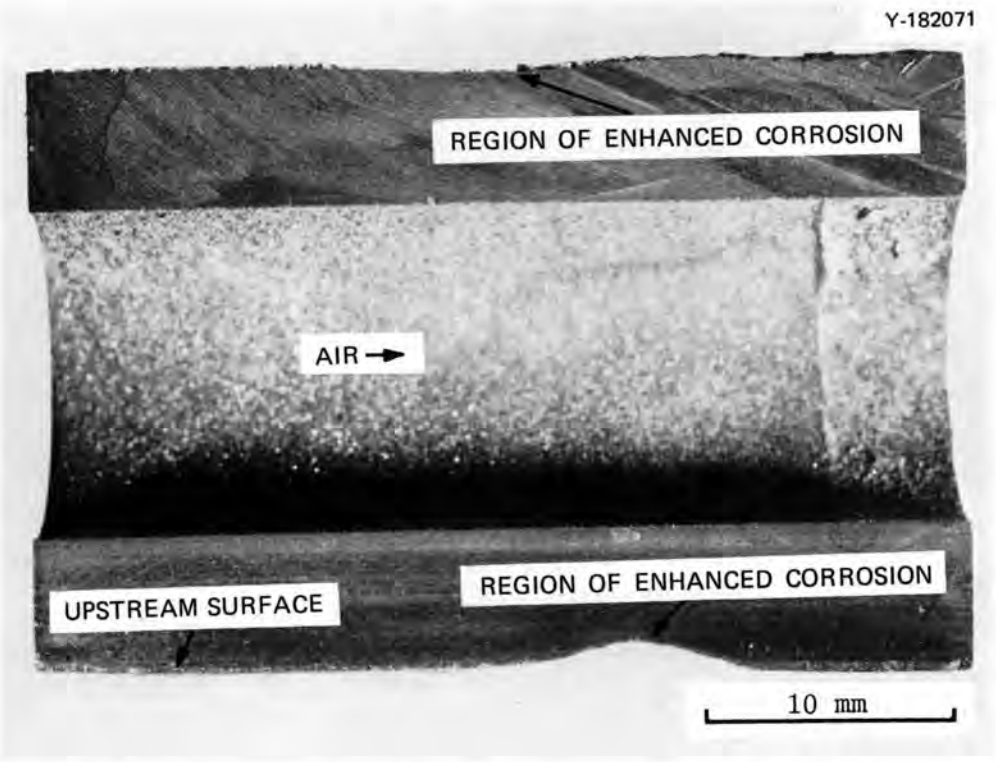

Fig. 18. Cross sectional view of post-test KT SiC illustrating enhanced corrosion near air outlet end.

Although the general slag characteristics are shown in Fig. 16, some minor variations occurred in the location and extent of the various slag features present on the silicon carbide and alumina tubes. However, in the case of the sialon ceramics, the slag appearance and behavior were quite different. For example, as shown in Fig. 19, the GE-128 sialon tubes were covered by a highly adherent porous slag layer which was quite resistant to removal by finger pressure. In addition, only one or two poorly developed nodules were observed along the upstream surface. The presence of a thin, white phase along the tube's interior and at the ceramic-slag interface also suggested that oxidation or other reactions occurred at these locations. In the case of the GE-129 and -130 sialons, thin, discontinuous coal slag layers were present on both the upstream and downstream surfaces [Figs. 19(a) and (b), respectively]. This slag also tended to be poorly bonded to the tubes.

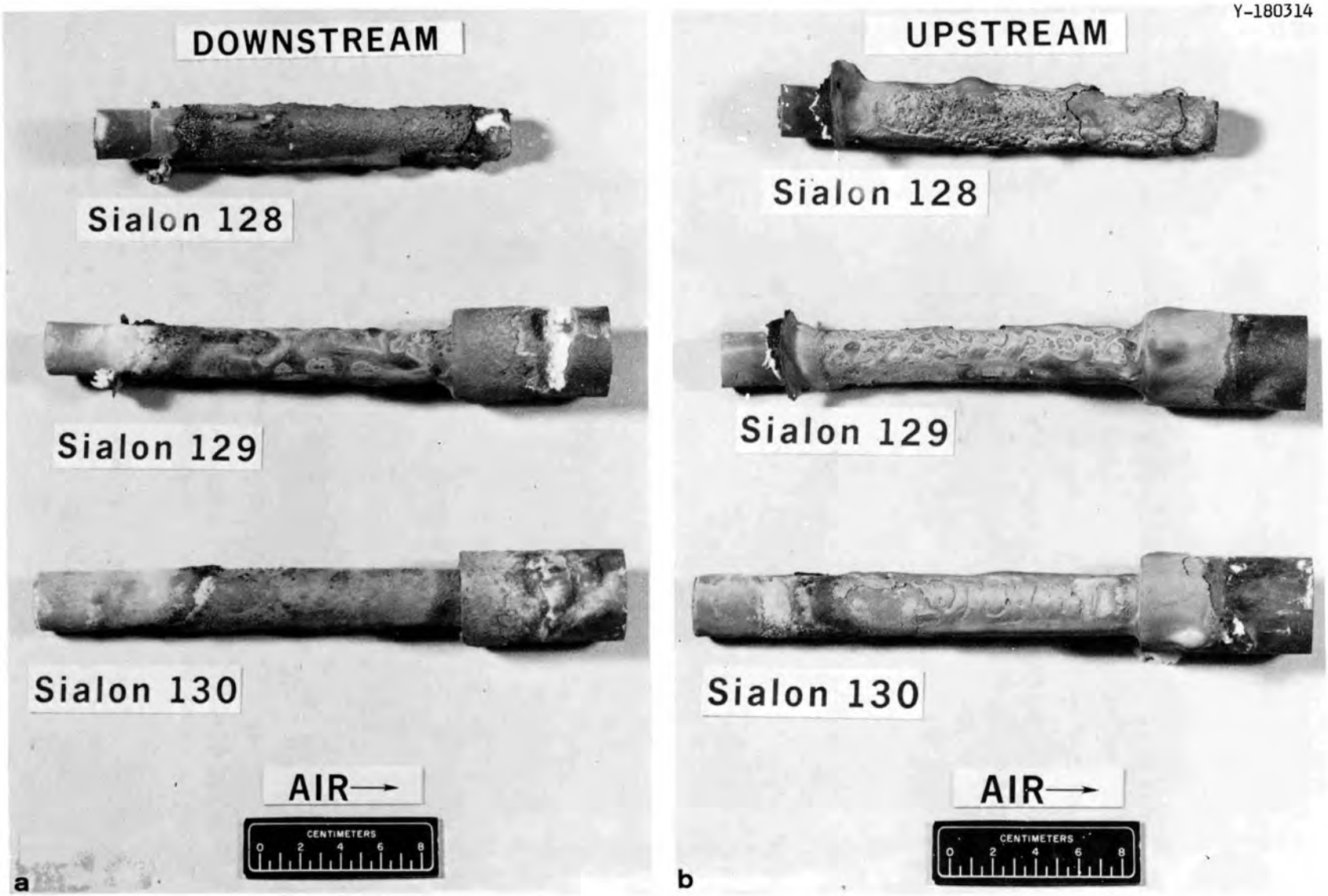

Fig. 19. Nature of slag deposit remaining on post-test sialon tubes. (a) Downstream. (b) Upstream.

It is possible that large amounts of gas were evolved from these materials during the 240-h exposure due to slag reactions which tended to debond the slag coating.

As previously indicated, the x-radiography analyses of several post-test tubes gave evidence of wall thinning in the upstream regions near the air outlet end. An example of this behavior is shown by the cross-sectional view of the SC-2 SiC tube in Fig. 20. In order to better quantify this material degradation, the post-test tubes were sectioned in a similar fashion as the tubular element in Fig. 20. The post-test

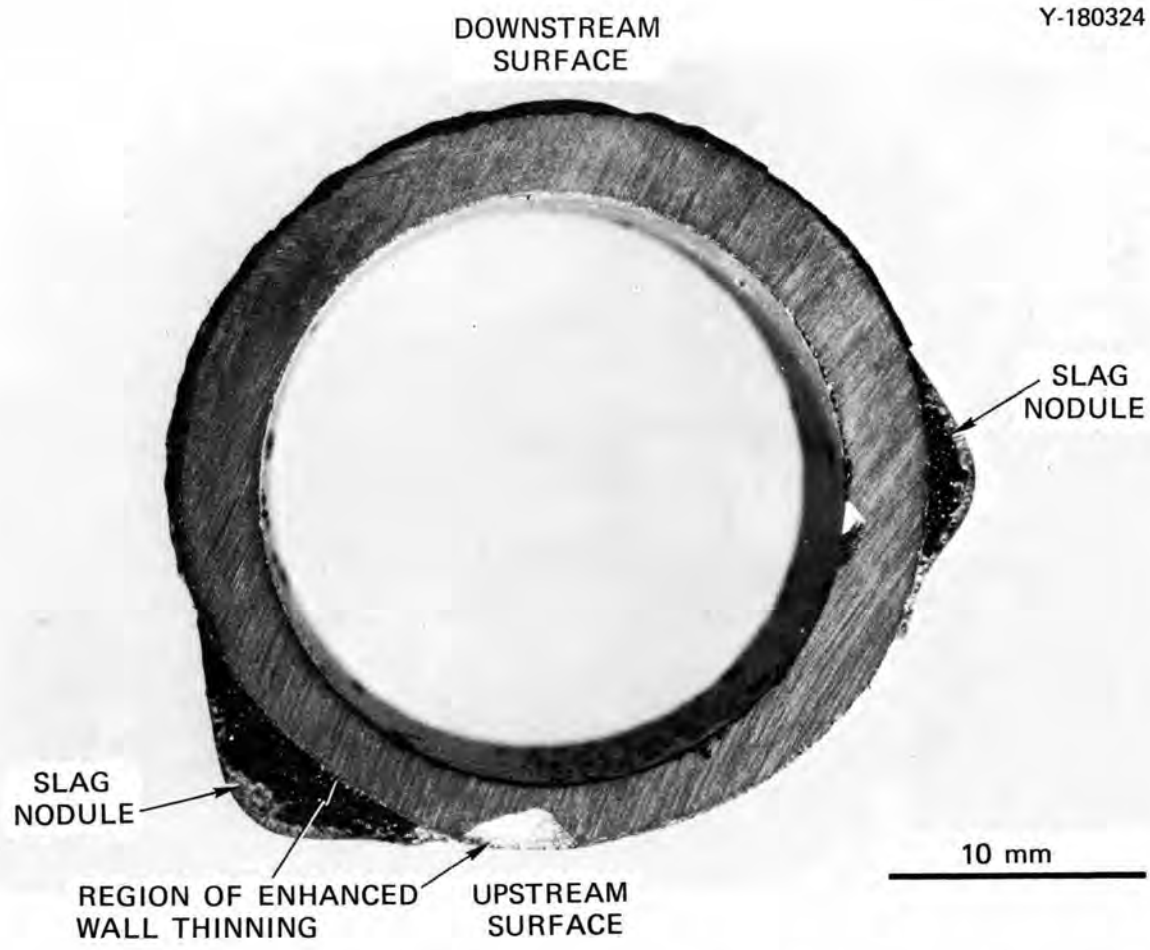

Fig. 20. Cross section of post-test SC-2 SiC showing wall thinning in upstream surface.

wall thicknesses were then measured in both the upstream and downstream regions. In all cases, the residual coal slag was removed prior to the measurements. Comparisons between the post-test thickness values and the average pretest thickness (Table 2) for various tubes are given in Table 7. The wall thinning in the upstream regions was significantly greater than that along the downstream surfaces. Furthermore, the extent of material loss from the tube wall was a strong function of the particular material. For example, in the upstream surfaces, the maximum wall thinning appeared to have occurred in the GE-128 and -129 sialons (78 and 56%, respectively) while less wall thickness loss was exhibited by the α-SiC, CVR SiC, CVD SiC, and Al_2O_3 (16, 7, 13, and 15%, respectively). The upstream thinning behavior of the siliconized silicon carbide (SC-2, KT, and NC 430 SiC) was intermediate between these two extremes.

The comparisons between the pre- and post-test wall thicknesses discussed above were subject to some measurement uncertainty. In part, this uncertainty resulted because the as-received and post-test thickness dimensions were not measured at identical positions along the length of each tube. Consequently, the comparisons in Table 7 are only valid for tubular elements where the pretest measurement was made in the same location as the subsequent post-test measurements. The large wall thickness dimensional variations in the as-received CVD SiC may explain why the downstream reduction in thickness value was positive for this material. A final factor responsible for the uncertainty in the Table 7 data concerns the considerable variations which occurred in the range of the post-test wall thicknesses. For example, the reduction in the upstream wall thickness was found to be a strong function of position along the tube length. The fact that the material degradation was enhanced at certain regions (typically near the air outlet end) indicates that the corrosion process occurring during the high-temperature exposure was highly localized. Although not indicated in Table 7, there was also evidence that considerable wall thinning occurred in the downstream regions adjacent to the thermocouple cement. In particular, subsequent measurements of the α-SiC (tube 2) revealed a 24% thickness reduction in the downstream wall that was located below the outermost thermocouple [(i.e., at L_3 in Fig. 3(b)].

Table 7. Comparison of the as-received and post-test wall thickness values for several tubular elements

Tube Designation	Thickness Value, mm				
		Post-Test[a]			
	As-received	Downstream	% Change	Upstream	% Change
SC-2 SiC (Tube 1)	3.125	2.885	(-7)	2.131	(-32)
SC-2 SiC (Tube 2)	2.955	2.647	(-10)	2.057	(-30)
KT SiC (Tube 1)	6.304	6.177	(-2)	5.082	(-19)
KT SiC (Tube 2)	3.285	2.946	(-10)	2.431	(-26)
α-SiC (Tube 2)	3.340	3.137	(-6)	2.822	(-16)
NC 430 SiC	3.925	3.566	(-9)	2.634	(-33)
CVR SiC	4.745	4.620	(-3)	4.420	(-7)
CVD SiC	3.120	3.546	(+14)	2.695	(-13)
Al_2O_3 (Tube 2)	2.770	2.920	(+5)	2.357	(-15)
GE-128	3.580	1.895	(-31)	0.594	(-78)
GE-129	4.250	3.045	(-28)	1.877	(-56)
GE-130	4.850	3.729	(-23)	3.940	(-19)

[a]The numbers in parentheses represent the percentage change in thickness which is given as: (post-test thickness minus pretest thickness)/pretest thickness.

As previously indicated, the extent of material degradation was highly dependent upon position along the tubular element. This behavior is illustrated in Fig. 21 which is a plot of the α-SiC (tube 1) upstream and and downstream wall thickness as a function of distance from the air inlet end. The gradual decrease in wall thickness with increasing distance from the air inlet end probably reflects the effect of increasing tube wall temperature on the corrosion rate (Fig. 9). For example, it is reasonable to expect that the higher temperatures caused an increase in slag fluidity and, thus, rate of material corrosion. Therefore, the substantial reduction in wall thinning near the air outlet end was probably due to a drop in temperature resulting from heat loss into the header block, or from stagnation of the gas at this location. Figure 21 also indicates that, for a given position along the tube, the rate of corrosion was significantly greater along the upstream surface compared to the down-stream side. This difference may also be due to a higher temperature in the upstream areas. However, it is also likely that the direct impingement of flue gas upon the upstream surface facilitated the corrosion mechanism by continually removing the ceramic-slag reaction products thereby making fresh surface of the ceramic available for attack. Finally, the data in Fig. 21 reveal that the maximum reduction (percentage) in the upstream and downstream wall thickness was —31 and —9%, respectively. The reason that these two percentages are larger than the corresonding values for α-SiC in Table 7 is that the Table 7 thickness measurements were made near the air outlet end of the tubes. Therefore, the post-test thickness values in this table are somewhat conservative.

MICROSTRUCTURE, MICROCOMPOSITION AND X-RAY PHASE ANALYSIS

The microstructure of the as-received and exposed ceramic materials as well as the coal slag was characterized using optical microscopy, scanning electron microscopy (SEM), and microprobe analyses. The post-test tubular specimens were sectioned such that the ceramic-slag interface remained intact. Examination of these interfacial regions provided insights into the nature of the reactions occurring between the ceramic and coal slag during the high-temperature exposure. The principal elements in

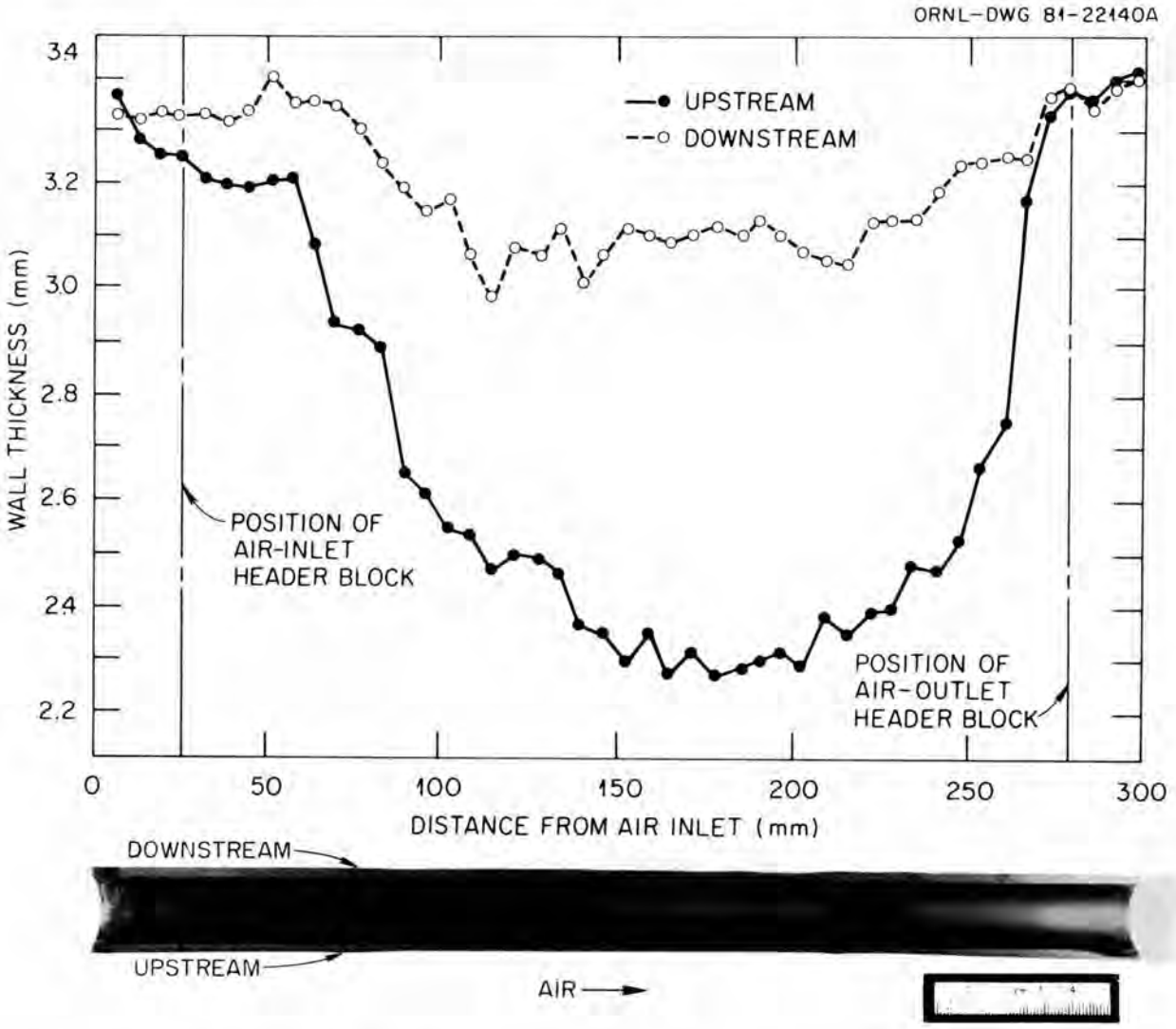

Fig. 21. Upstream and downstream tube wall thickness profiles of the α-SiC postexposed tube.

the various microstructural phases were also identified by microprobe measurements or energy-dispersive x-ray analyses performed in conjunction with the SEM examinations. The resulting information was supplemented by the microcompositional studies which included spark source mass spectroscopy and fast neutron activation analysis of both as-received and exposed samples of selected silicon carbides (Table 8). The post-test samples were prepared from the upstream regions of the tubes following removal of any residual coal slag. Therefore, the elemental variations were indicative of changes which occurred in the ceramic material due to the COM combustion exposure. Finally, several x-ray diffraction studies were used to identify the major phases received and exposed tubular elements as well as representative coal slag samples. The post-test analyses of the ceramic materials were again limited to upstream regions in each tube where the reaction with the coal slag was greatest. The crystalline phases were identified by matching the experimental d-spacings of the x-ray diffraction pattern with known spacings of specific materials given in the literature[6,10] or in the powder diffraction file published by the Joint Committee on Powder Diffraction Standards (JCPDS).[11] The results are summarized in Table 9. The following sections provide detailed discussions of the results of all three analyses for the various tubular materials. For convenience, materials having similar chemical and microstructural characteristics are considered together.

α-SiC

The as-received α-SiC had a uniform grain structure containing small graphitic inclusions less than 1 μm in diameter. These features are illustrated in Fig. 22 which is a bright-field micrograph of a polished cross section after etching. Although not visible in this figure, small metallic particles were situated along many of the grain boundaries. Further examination of the α-SiC microstructure revealed the presence of elliptical-shaped voids having major and minor dimensions of 100 μm and 30 μm, respectively. The major axis of these defects was generally

Table 8. Results of elemental analyses of as-received and exposed SiC tubes[a]

Element	Concentration, wt % ppm[b]							
	α-SiC		KT SiC		CVD SiC		SC-2 SiC	
	As-received	Exposed	As-received	Exposed	As-received	Exposed	As-received	Exposed
Al	50	30	400	>1000	100	70	500	700
B	60	200	2	9	6	0.5	800	300
Ca	20	30	30	700	30	200	100	300
Co[c]	>1000	>1000	400	>1000	>1000	>1000	>1000	>1000
Cr	30	10	30	100	30	20	200	100
Cu	3	2	10	100	8	2	20	700
Fe	80	70	1000	2000	200	200	2000	4000
Ga	0.3	<0.7	0.5	0.8	0.8	<0.2	0.3	0.5
K	5	10	10	30	20	20	20	30
La	3	1	4	<3	<1	1	4	4
Mg	20	3	40	30	10	20	1	20
Mn	1	2	20	20	3	3	50	20
Mo	6	5	6	9	9	6	10	20
Na	1	5	3	>200	10	20	2	30
Ni	8	20	40	1000	7	100	100	~3000
O[d]	0.068%	0.14%	0.10%	0.18%	0.10%	0.25%	0.12%	0.25%
P	0.5	3	2	8	2	5	20	20
S	20	40	30	60	50	30	50	100
Si	major	major	major	major	major	major	major	major
Ta	100	700	100	1000	200	300	70	700
Ti	30	200	70	400	70	300	70	300
Y	1	1	2	1	<0.2	0.3	2	1
V	10	10	40	20	4	8	30	40
Zn	0.6	0.8	3	2	6	2	2	4
Zr	2	2	9	9	1	0.9	20	30

[a] Determined by Spark-Source spectroscopic analysis (precision + 100, −50%) unless otherwise specified.

[b] Weight percent if % is shown.

[c] May represent contamination from grinding media used in sample preparation.

[d] Determined by neutron activation chemical analysis.

Table 9. Results of x-ray analyses of as-received and post-test tubes.[a]

Material	Condition	Crystalline Phases
α-SiC	As-received	α-SiC (33R), α-SiC (12H), graphite*
	Post-test	α-SiC (33R), α-SiC (12H), graphite, unidentified phase(s)
CVD SiC	As-received	β-SiC
	Post-test	β-SiC, unidentified phase(s)
CVR SiC	As-received	β-SiC, graphite
	Post-test	β-SiC, graphite, Si, unidentified phase(s)
KT SiC	As-received	α-SiC (33R), α-SiC (12H), Si, graphite
	Post-test	α-SiC (33R), α-SiC (12H), Si, graphite, unidentified phase(s)
SC-2 SiC	As-received	α-SiC (12H), Si, FeS
	Post-test	α-SiC (12 H), Si, FeS, unidentified phase(s)
NC 430 SiC	As-received	α-SiC (12H), Si
	Post-test	α-SiC (12H), Si, unidentified phase(s)
AD 998 Al_2O_3	As-received	α-Al_2O_3
	Post-test	α-Al_2O_3, unidentified phase(s)
Sialon 128	As-received	β-Si_3N_4 (14 H), $Si_3Al_{2.67}N_4D_4$, β-Sialon
	Post-test	β-Si_3N_4(14 H), $Si_3Al_{2.67}N_4O_4$, β′-Sialon, α-$Mg_2Al_4Si_5O_{18}$
Sialon 129	As-received	β-Si_3N_4 (14 H), β-Si_3N_4 (28 H), β′-Sialon
	Post-test	β-Si_3N_4 (14 H), β′-Sialon, unidentified phase(s)
Sialon 130	As-received	β-Si_3N_4 (14 H), β′-Sialon, unidentified phase(s)
	Post-test	β-Si_3N_4 (14 H), β′-Sialon, unidentified phase(s)
Coal Slag	Air Inlet Region[b]	$(Ca-Mg-Fe-Al)_2(Si-Al)_2O_4$, $Na,AlSi_3O_8$
	Slag Nodules[c]	$(Ca-Fe-Mg)SiO_3$, $(Ca-Ti-Mg-Al)(Si-Al)O_6$
	Slag Inclusions	$NiSi_2$, $FeSi_2$, Si

[a] Post-test analyses performed on upstream ceramic surface unless stated otherwise.

[b] Represents both upstream and downstream samples.

[c] Samples removed from both KT SiC and Al_2O_3 tubes.

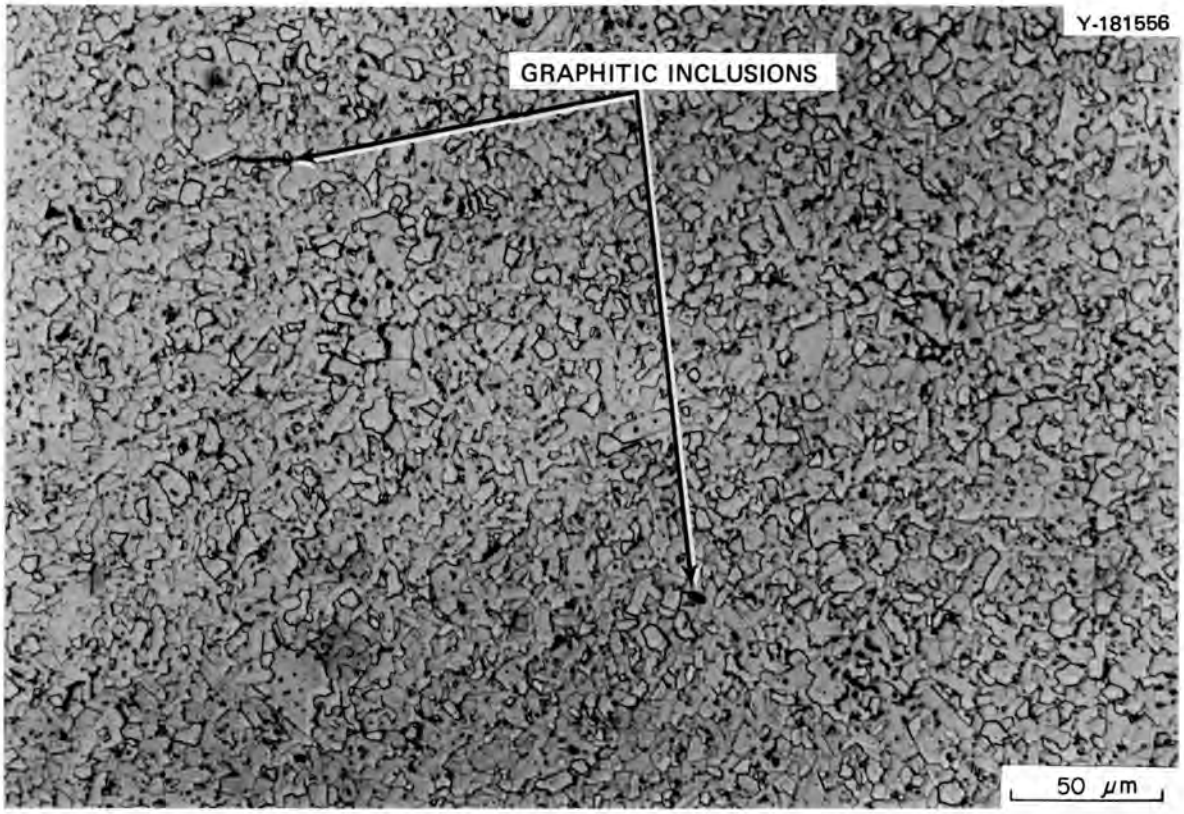

Fig. 22. Typical microstructure of as-received α-SiC.

oriented parallel to either the long axis of the tube or the tube circumference. It is likely that the voids resulted from delamination of the material during initial fabrication. These microstructural features were identical to those observed in the pretest α-SiC used in CRAF Test 2. Additional details concerning the α-SiC microstructure are given in a related report.[6]

The major crystalline phases detected in the as-received sintered silicon carbide (Table 9) were α-SiC (12H) and α-SiC (33R). The experimental d-spacings also indicated the presence of graphite which is consistent with the microstructural observations. The results of the elemental analyses (Table 8) revealed significant concentrations (>20 ppm) of Al, B, Ca, Co, Cr, Fe, Mg, O_2, S, Ta, and Ti in the pretest material. The Co and Cr may have been introduced during the grinding operation used for sample preparation prior to analysis. However, the B and Al which are typically used as sintering aids for densification of α-SiC, were probably

indicative of the intrinsic material composition. The source of the remaining elements is presently unknown.

Microstructural examinations of the ceramic-slag interface in the post-test α-SiC indicated that surface degradation involved a highly localized process consisting of several successive steps. The first step apparently involved a chemical reaction between the coal slag and small regions along the α-SiC surface. The size of these areas was typically on the order of 1 to 3 μm along the upstream surfaces and 4 to 9 μm along the downstream surfaces. Several isolated reaction sites along the upstream ceramic-slag interface are illustrated in Fig. 23(a). The high reflectivity of these reaction phases as compared with the bulk silicon carbide suggests that the ceramic-slag reaction produced significant changes in the microcomposition of the SiC. Once the reaction was completed, the newly created phase regions were transported away from the interface into the coal slag matrix. Upon removal from the interfacial region, these reaction phases were apparently dissolved or disintegrated via other chemical reactions with the coal slag. The disruption of the reaction product particles, which is shown in Fig. 23(b), was generally completed in the slag within 1 to 10 μm above the tube surface. The crack in the SiC in this figure was produced during metallographic specimen preparation. The removal of the reaction phases also resulted in the formation of micropits [(Fig. 23(a)]. It is likely that during the actual exposure, such voids were quickly filled by the fluid coal slag and the above corrosion process repeated. Since this localized corrosion phenomenon occurred fairly uniformly on the surface of the α-SiC tube, the macroscopic surface recession rates were fairly uniform on a local scale of tens to hundreds of micrometers.

Additional insights into the chemical nature of the ceramic-slag reaction phase on the α-SiC surface were obtained from microprobe analysis of a typical upstream region illustrated in Fig. 24(a). The distribution of Si, Ca, Fe, and Ni, which were the major elements detected, is shown in Fig. 24(b) through (e), respectively. The coal slag matrix contained high concentrations of Ca, Si, and Fe as expected while Ni was concentrated at the tube-slag interface. The results of the x-ray diffraction studies (Table 9) indicated that Ca, Si, and Fe were primarily in the form of a

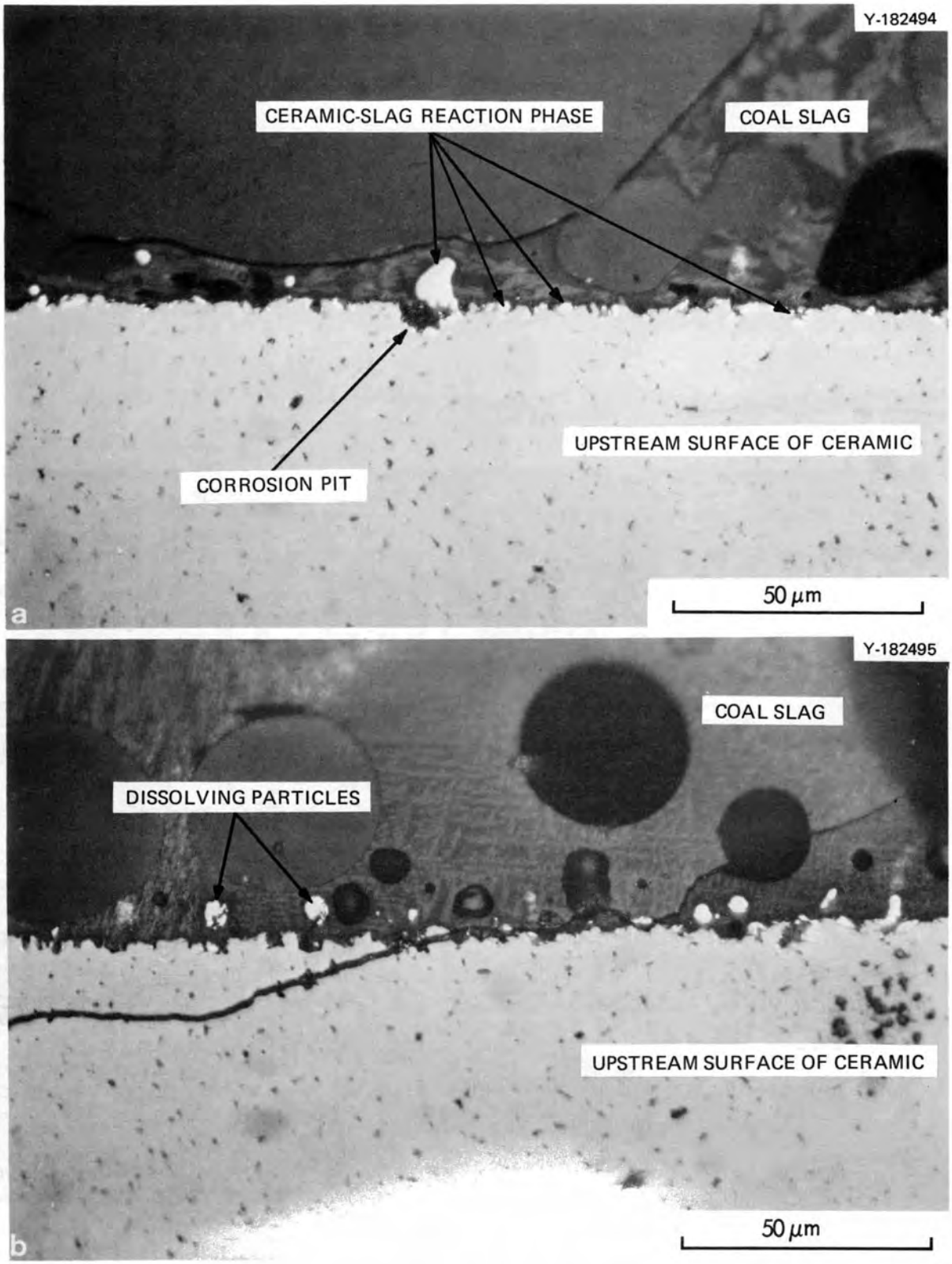

Fig. 23. Micrographs of ceramic slag interface in exposed α-SiC illustrating (a) formation of isolated slag-ceramic reaction phase, and (b) dissolution of reaction phase particles in coal-slag matrix.

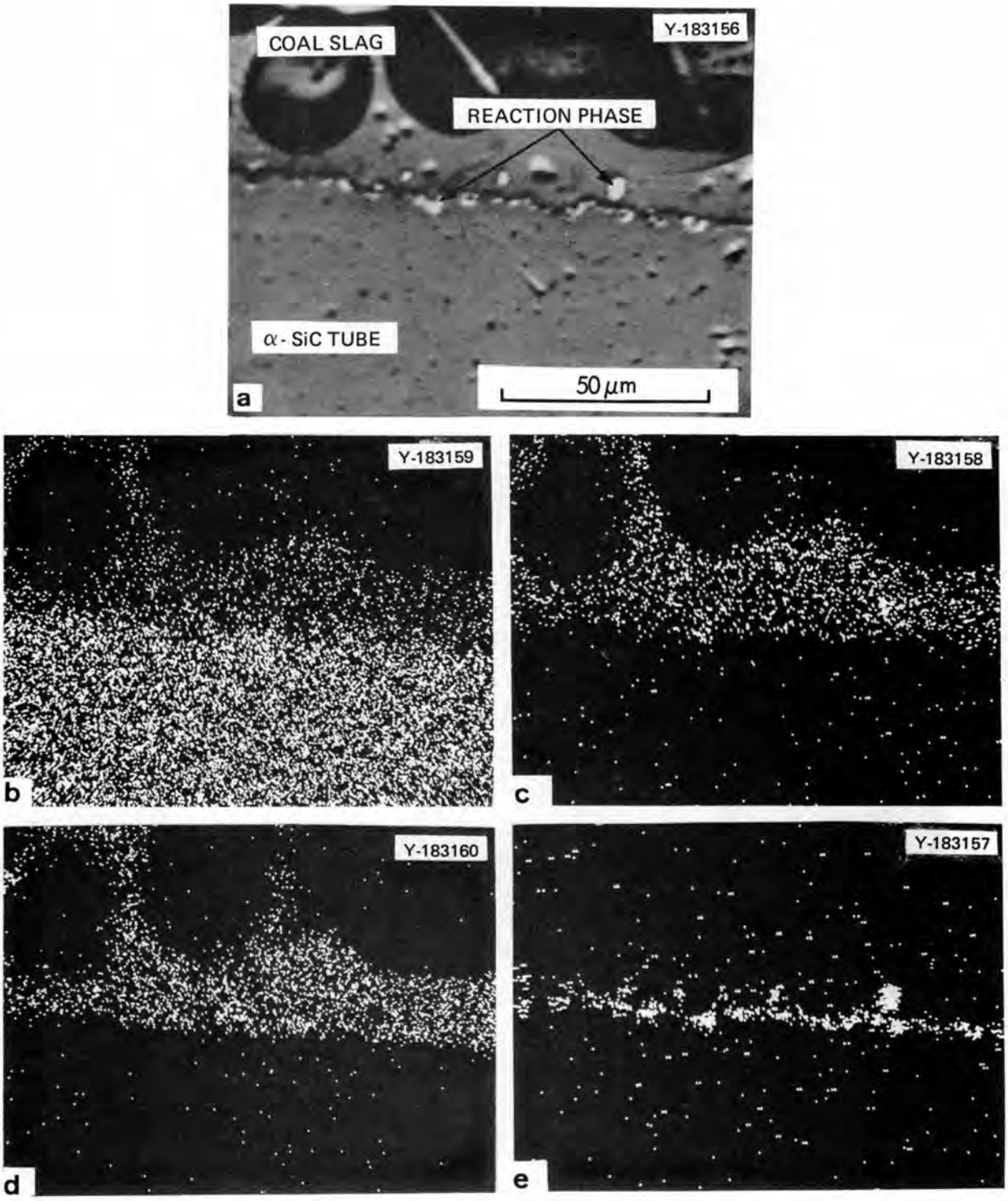

Fig. 24. Results of microprobe analysis of upstream α-SiC surface. (a) Backscattered SEM image of ceramic-slag interface and elemental distributions of: (b) Si, (c) Ca, (d) Fe, and (e) Ni.

calcium silicate, which contained solid solution additions of Fe, Al, and other minor elements. Additional details concerning the chemical nature of the coal slag matrix will be given in a subsequent section. The principal elements associated with the ceramic-slag reaction phase [(Fig. 24(a)] were Si, Ni, and Fe. Generally, the limited dimensions of these regions precluded their further analysis by x-ray diffraction techniques. However, in a few cases, the size of this phase was on the order of 1 to 2 mm in diameter. Initial evidence of these extensive ceramic-slag reaction areas was provided by the radiographic examinations which revealed the presence of highly absorbing spherical inclusions within the coal slag. Because of their larger size, these inclusions were apparently able to survive in the slag much longer than did the smaller particles shown in Fig. 23. Therefore, several samples, which were representative of the ceramic-slag reaction phase, were available for x-ray diffraction analysis. The major chemical compounds subsequently identified were $FeSi_2$, $NiSi_2$, and Si. The low oxygen potential required for the presence of silicon in the iron and nickel silicides suggests that the oxygen partial pressure was quite low at the ceramic-slag interface during the combustion gas exposure. Finally, it should be mentioned that the above results are quite similar to those obtained in a previous laboratory-scale slag exposure test involving siliconized silicon carbide.[12]

The x-ray diffraction analysis of the post-test α-SiC, which was performed following removal of the residual coal slag, revealed the presence of unidentified phase(s) in addition to those detected in the as-received material (Table 9). At present, the source of the phase(s) is unknown. Some minor changes were also observed in the postexposure elemental concentrations (Table 8). For example, B, O, Ta, and Ti exhibited significant concentration increases while the Al, Cr, and Mg concentrations dropped slightly during the exposure. Again, the reasons for these variations are uncertain.

CVD and CVR SiC

A typical cross-sectional view of an etched as-received CVD SiC metallographic specimen is illustrated in Fig. 25. In general, the microstructure was quite similar to that observed in the CRAF Test 2 material.[6] The only significant difference was in the lack of uniformity in the outer surface of the CVD SiC used in this test. As shown in Fig. 25, the surface topography was characterized by hemispherical ridges approximately 1 mm in diameter. The microstructure of the as-received CVR SiC as shown in Fig. 26 was also characterized by typical CVD SiC deposits along the inner and outer diameters; however, the region within the tube interior consisted of isolated SiC grains, carbon, and possibly limited amounts of free silicon. The lack of a densified structure in this region was probably due to an incomplete reaction between the carbon and silicon to form silicon carbide during tube fabrication.

The major crystalline phase in the as-received CVD and CVR silicon carbides was β-SiC (Table 9). Its formation was primarily a result of the chemical vapor deposition processes employed in the fabrication of both materials. The x-ray data also gave evidence of significant amounts of graphite in the as-received CVR SiC which agrees with previous microstructural results. The results of the microcompositional analyses* (Table 8) revealed high concentrations (>50 ppm) of Al, Fe, S, O, and Ta in the CVD SiC. These elements were probably incorporated into the material during the high-temperature CVD deposition process. Potential sources of contamination include the chemical reactants used to deposit the SiC and the graphite mandrels upon which the SiC was deposited.

Examination of the post-test metallographic CVD and CVR SiC specimens indicated that surface degradation in both materials was quite similar to that in the α-SiC. The upstream CVD and CVR SiC surface regions shown in Fig. 27(a) and (b), respectively, indicate that a localized reaction occurred between the coal slag and ceramic surface. The high-reflectivity reaction product phase illustrated in both micrographs is

*No CVR SiC sample was analyzed

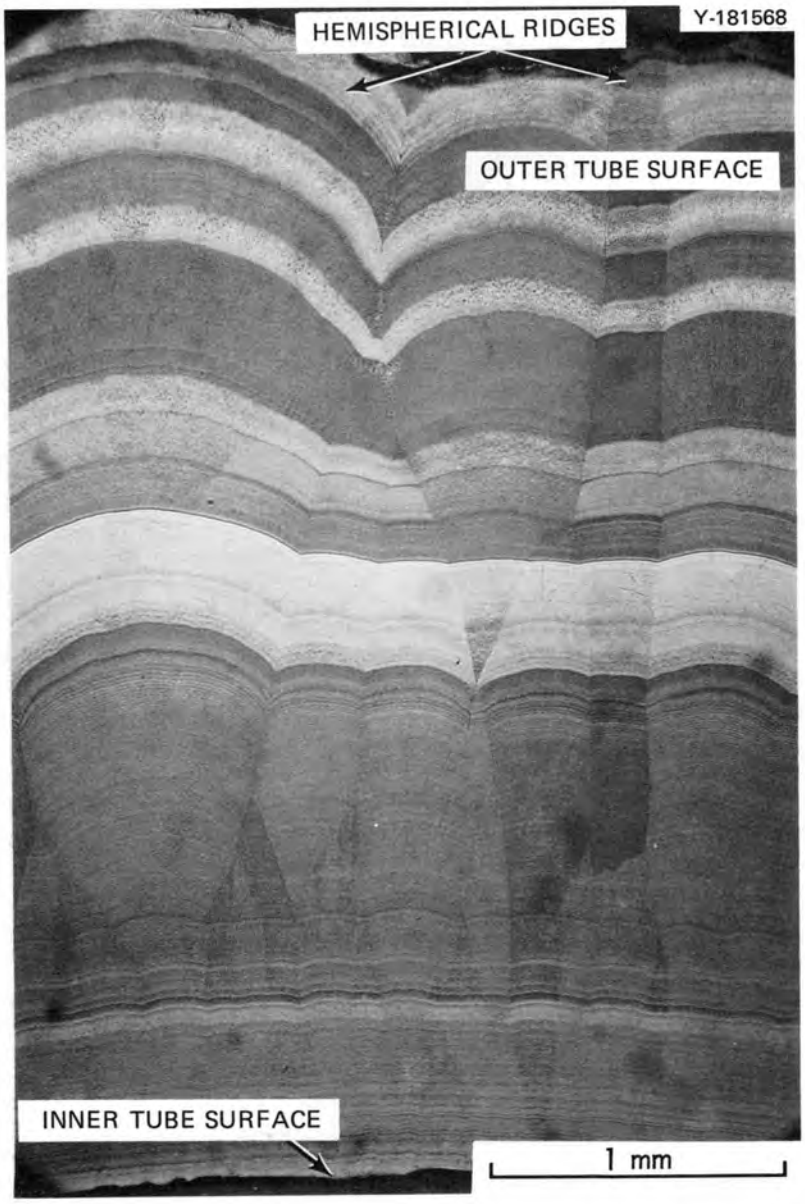

Fig. 25. Micrograph of as-received CVD SiC illustrating lack of uniformity along outer surface.

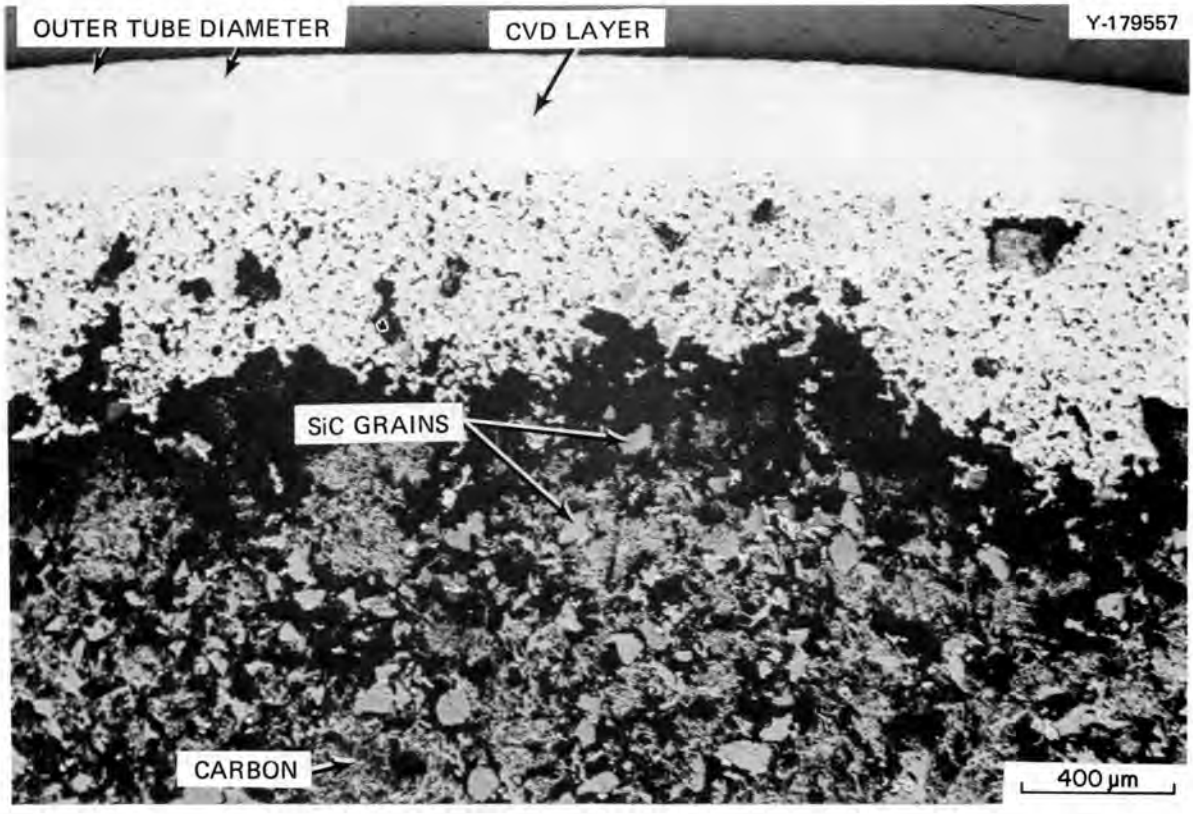

Fig. 26. Micrograph of as-received CVR SiC showing CVD layer along outer diameter and lack of sample reaction at tube interior.

almost identical in appearance to that observed along the upstream α-SiC surface (Fig. 23). Furthermore, the surface degradation appeared to follow the same sequential steps as in the α-SiC material including (1) reaction at the ceramic-slag interface resulting in the formation of isolated regions of a high-reflectivity phase, (2) subsequent transport of this phase into the coal slag matrix while forming micropits in the ceramic surface, and (3) dissolution of the reaction product phase by the coal slag. Although the mechanism of ceramic material removal in the CVR, CVD, and α-SiC tubular specimen was characterized by this reaction sequence, some minor variations in the nature of the coal-slag attack of the three materials were also observed. In the case of α-SiC, the ceramic-slag reaction was generally limited to small hemispherical regions along the ceramic surface (Fig. 23). However, the coal-slag attack at the CVR SiC

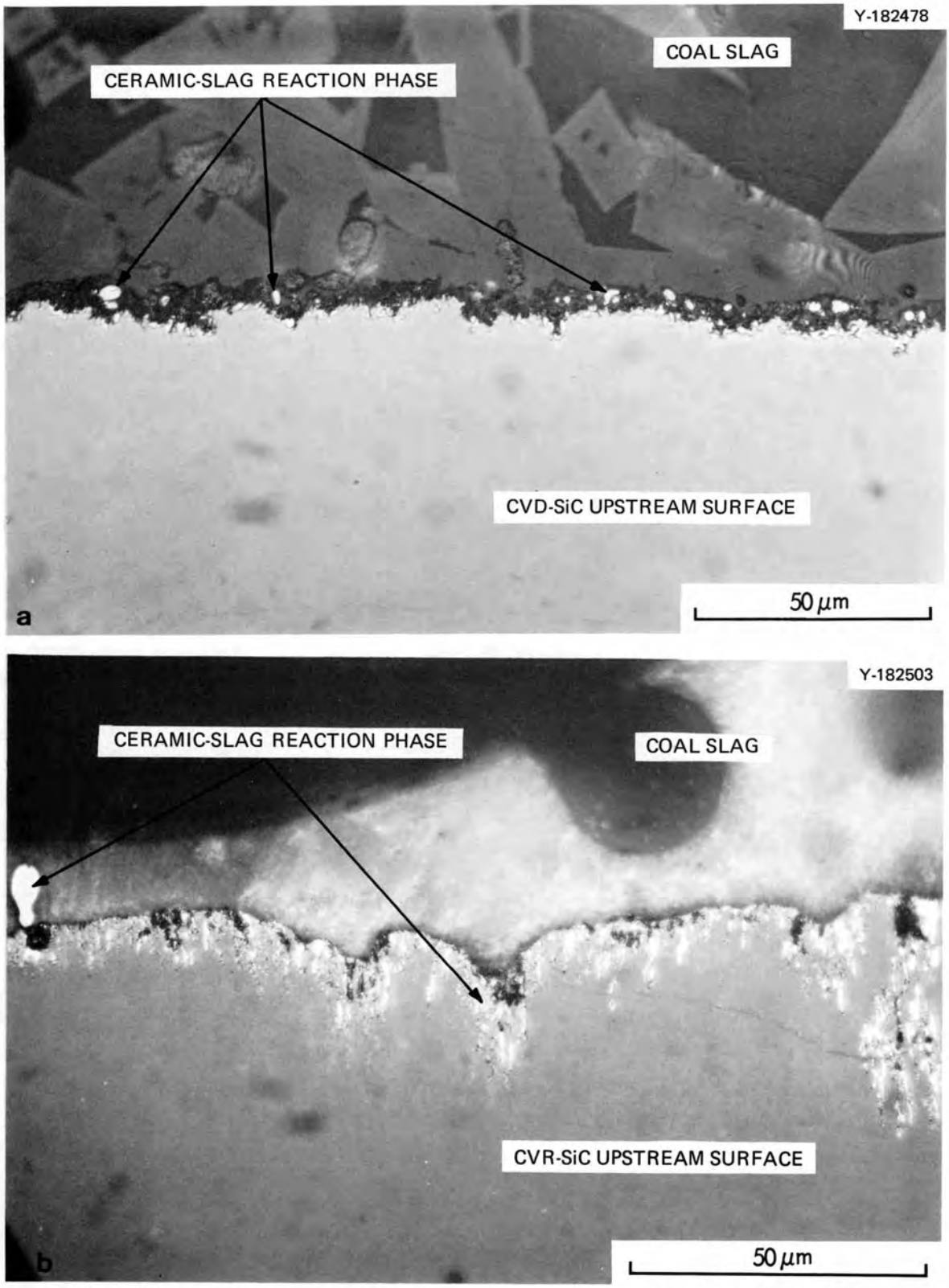

Fig. 27. Upstream surface regions in post-test metallographic samples of (a) CVD SiC and (b) CVR SiC illustrating formation of ceramic-slag reaction zone.

surface proceeded more extensively perpendicular to the ceramic-slag interface in what appeared as cylindrical regions with diameters of about 5 to 10 μm [Fig. 27(b)]. Thus, the reaction phase product was observed to be deposited in narrow elongated regions when viewed in longitudinal sections as shown in Fig. 27(b). This preferential attack was probably related to the microstructural features (which were present along the outer tubular surface of the CVR SiC tube) associated with the CVD coating. For example, the columnar growth of the β-SiC crystalline phase, which is characteristic of the microstructure of SiC formed by chemical vapor deposition, generally leads to the formation of long vertical boundaries parallel to the radial direction in the tube,* where the SiC growth cones intersect with each other. Therefore, it is possible that, during the combustion exposure, these boundaries in the CVR-SiC were highly susceptible to coal-slag penetration. The fact that this preferential corrosion was somewhat limited in the CVD SiC [(Fig. 27(a)] may reflect differences in the microstructure of the CVD SiC produced by the two manufacturers.

An elemental x-ray analysis was performed on the upstream CVD SiC surface region shown in Fig. 28(a). High concentrations of Fe and Ni were again present in the ceramic-slag reaction phase. In addition, the coal-slag matrix consisted primarily of Ca and Si with minor amounts of Fe, Al, K, and Na. The distributions of Si, Ca, Fe, and Ni in this upstream region are shown in Fig. 28(b) through (e), respectively. As with the α-SiC, these results suggest that Fe and Ni were intimately involved in the surface degradation process in the CVD SiC. Again, it is possible that the reaction phase was composed of an iron or nickel silicide.

The post-test x-ray diffraction studies revealed several minor changes in the nature of the phases associated with the post-test CVD and CVR SiC materials (Table 9). For example, a small amount of silicon was detected in the postexposure CVR SiC. Its formation may have been a result of

---

*These boundaries are readily visible when the CVD material is etched. For reference, see Fig. 25 in this report and Fig. 36 in the CRAF Test 2 report.[5]

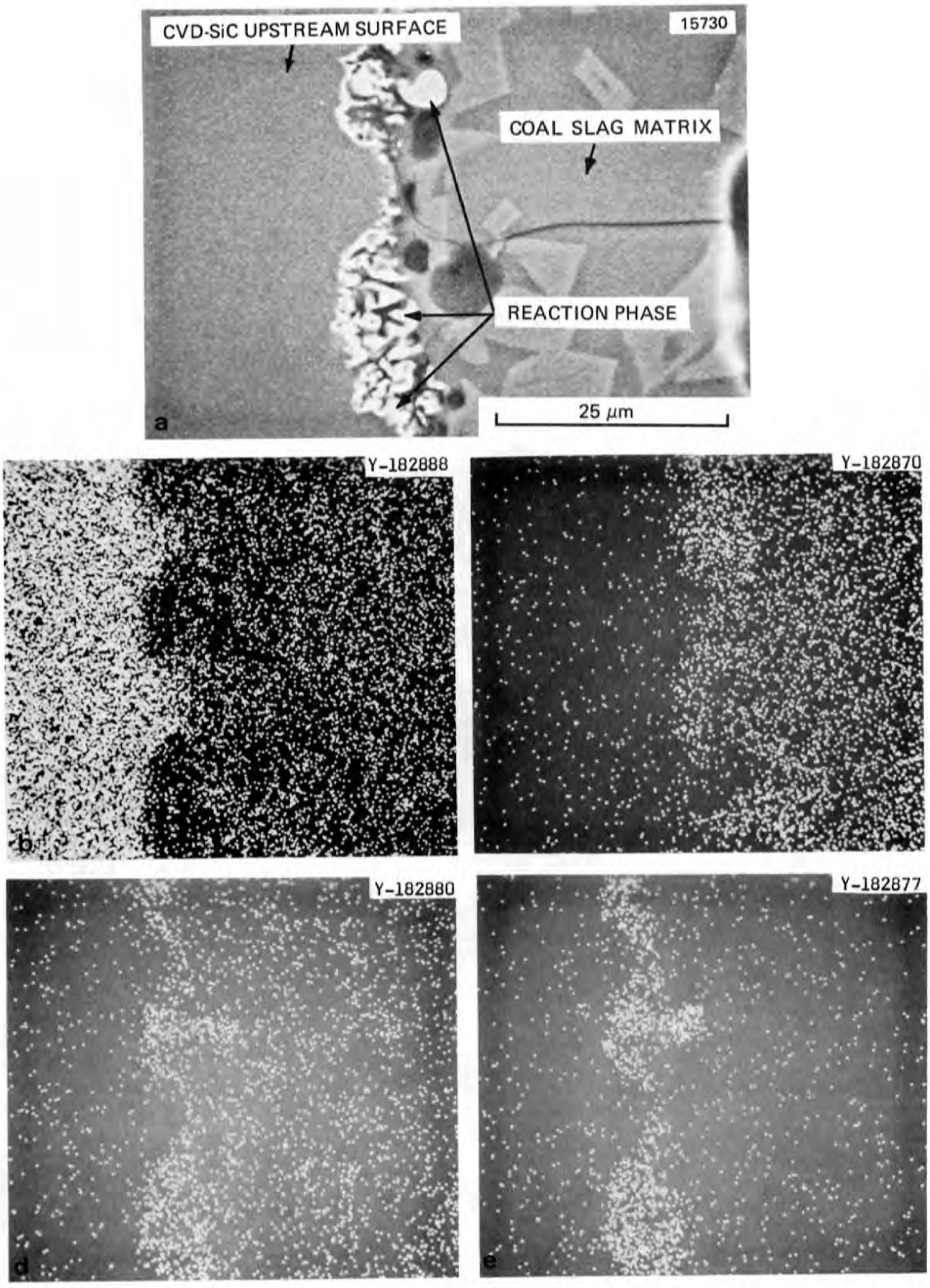

Fig. 28. Results of SEM examination of upstream surface of post-test CVD SiC illustrating (a) backscattered micrograph and associated elemental distributions of (b) Si, (c) Ca, (d) Fe, and (e) Ni.

chemical changes occurring within the poorly developed interior of the tube wall. In addition, unidentified phases appeared in both materials following the combustion exposure. These phases may have been representative of slag remnants present on the tubular surfaces. Finally, as shown in Table 8, changes also occurred in the concentration of several minor elements present in the CVD SiC. In particular, the post-test sample exhibited significant increases in Ca, Ni, Ti and O. These increases were apparently a result of selective elemental transport from the coal slag matrix into the bulk of the CVD SiC ceramic.

KT, SC-2, and NC 430 SiC

As previously indicated, these three materials were all forms of siliconized silicon carbide which typically has a microstructure consisting of SiC grains in a silicon matrix. This characteristic feature is illustrated in the micrographs of the as-received KT, NC 430, and SC-2 SiC (Figs. 29 through 31, respectively). It should be noted that the NC 430 SiC

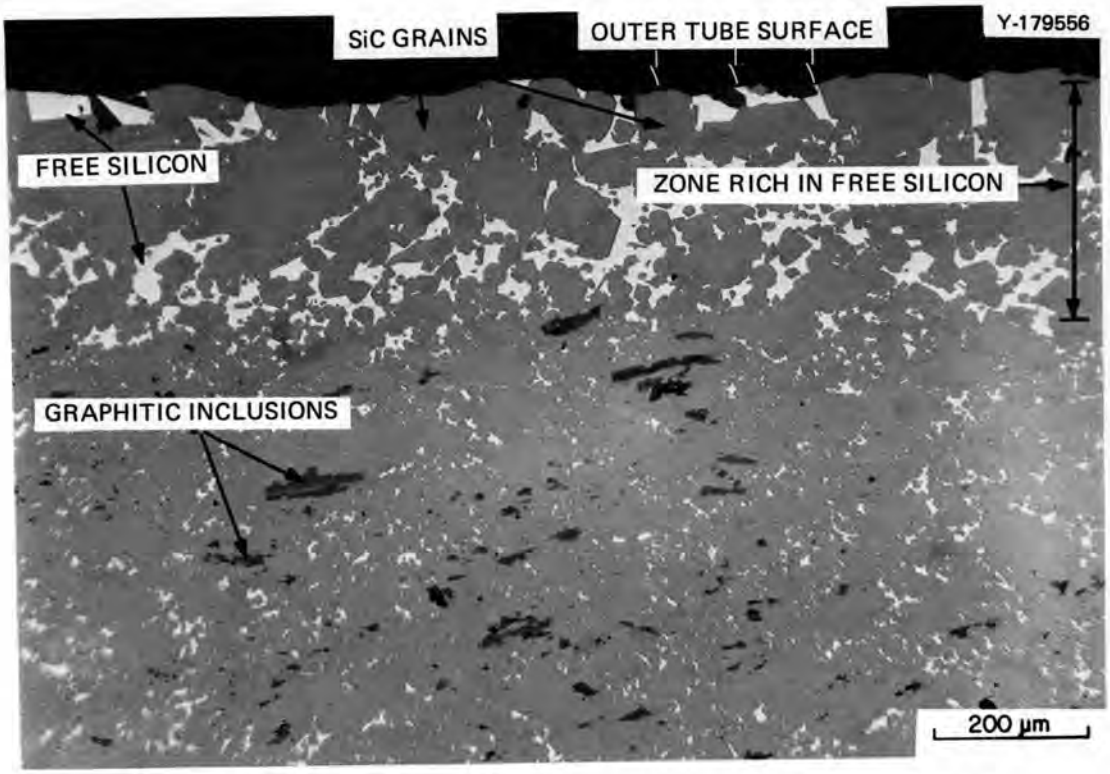

Fig. 29. Microstructure of as-received KT SiC illustrating presence of graphite inclusions and rich free silicon zone along outer tube diameter.

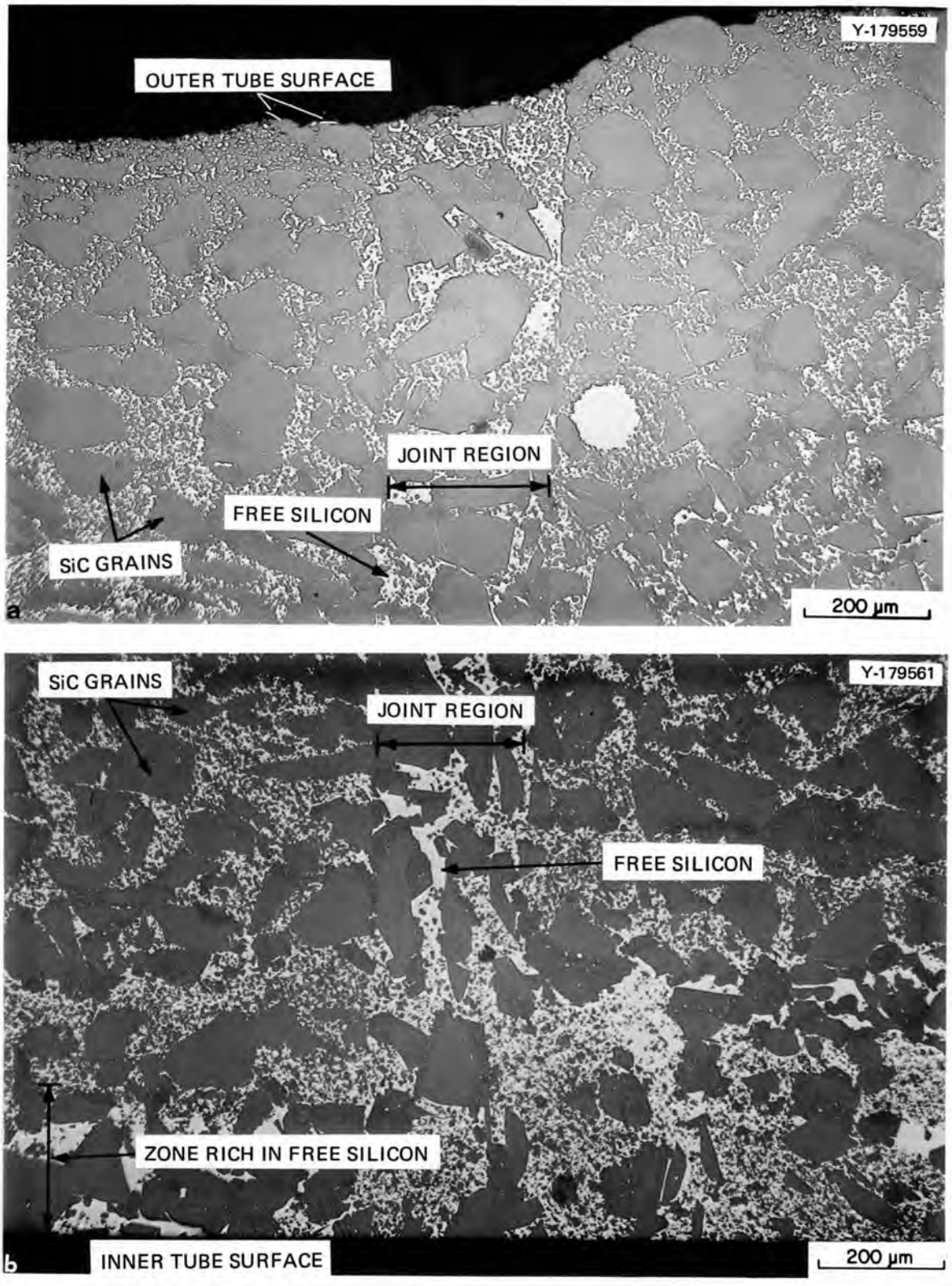

Fig. 30. Microstructure of as-received NC-430 SiC illustrating nature of butt joint in vicinity of (a) outer and (b) inner tube surface regions.

micrographs were taken in the region of the butt-joint near both the outer and inner tube diameters [(Fig. 30(a) and (b), respectively)].

Several interesting features are present in the microstructures of these three siliconized silicon carbides. For example, it is apparent that a zone, rich in free silicon, existed in both the KT SiC along the outer tube surface and the NC 430 SiC along the inner surface. In the case of the KT material, the SiC grains within this zone were significantly larger than those within the tube interior. A similar variation in grain size was not observed in the NC 430 microstructure. However, the SiC grains in the NC 430 material were characterized by a bimodal distribution which was fairly uniform throughout the tube wall. These microstructural features in the KT and NC 430 SiC were sharply contrasted by the uniformity in both the size and distribution of the small SiC grains present in the SC-2 SiC. As discussed later, these differences in microstructures were apparently responsible for variations in the pretest C-ring fracture strength. Figure 29 also reveals the existence of numerous graphitic regions in the KT SiC. In addition, small metalliclike inclusions were observed in the silicon phase in both the KT and SC-2 SiC materials. Because of their small size, the inclusions are not visible in either Figs. 29 or 31. Previous studies[5,6] have indicated that the metallic regions in the KT SiC consist of high concentrations of iron and nickel. Finally, as shown in Fig. 30, the joint region in the NC 430 SiC contained slightly more free silicon than the bulk material. No other major differences were found.

Elemental analyses were performed on selected samples of KT and SC-2 SiC. The results (Table 8) revealed fairly large concentrations of Al, Fe, O, Ta, and Ti in both materials. In addition, significant amounts of B, Ca, Cr, Mg, and Ni were found in the SC-2 SiC. It is likely that the Fe, Ni and Ti were associated with the metalliclike inclusions previously observed in the silicon phase. The source of the remaining elements is currently unknown.

The major crystalline phases in all three pretest siliconized SiC materials were α-SiC and Si (Table 9). Graphite was also detected in the KT SiC, which is consistent with the metallographic examinations. However, the presence of FeS in the SC-2 SiC is somewhat puzzling, especially in light of the low elemental sulfur concentration found in the

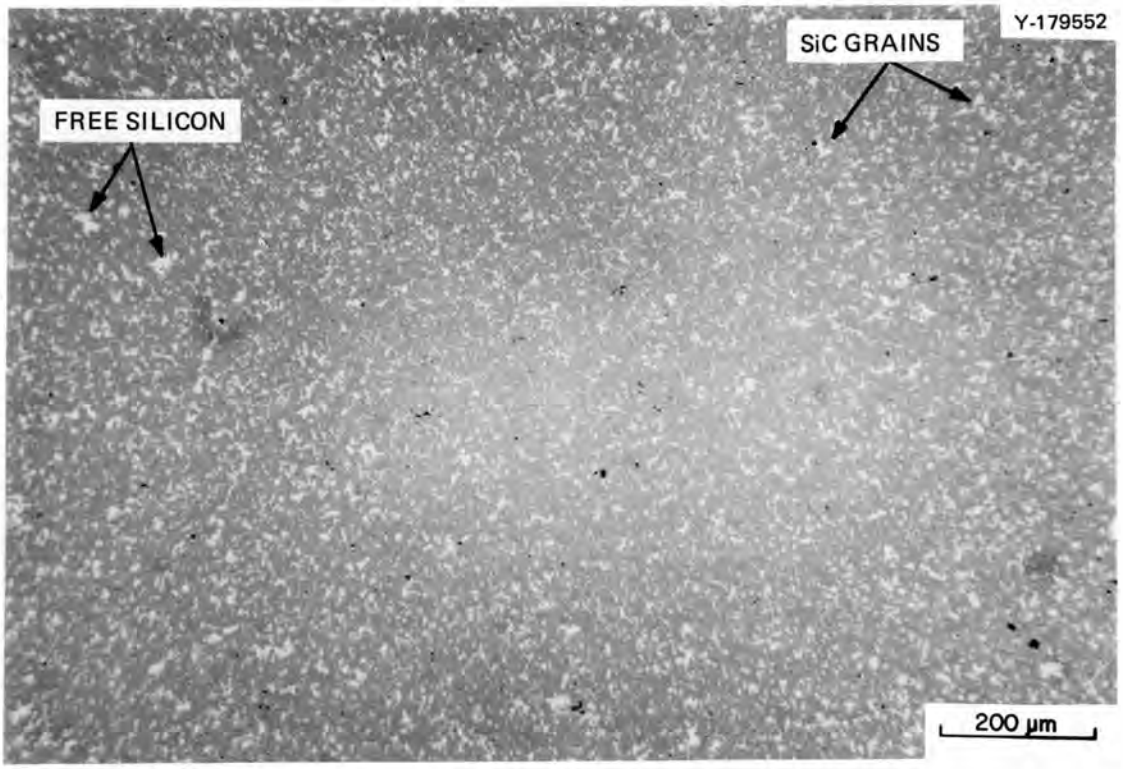

Fig. 31. Microstructure of as-received SC-2 SiC illustrating uniformity in SiC grain size and silicon distribution.

as-received material (Table 8). It is possible that a compound having a crystal structure similar to that of FeS was actually present in the pre-test SC-2 silicon carbide.

The metallographic examination of the post-test siliconized silicon carbides indicated that the surface corrosion was again due to a localized reaction between the coal slag and ceramic material. In the case of the KT and NC-430 SiC materials, this reaction resulted in the formation of a secondary phase, which was very similar to that observed at the ceramic-slag interface along the upstream surfaces of CVD, CVR, and α-SiC [(Figs. 23, 27(a), and 27(b)]. For example, Fig. 32 illustrates a typical upstream surface area in the postexposed KT SiC tube. In general, isolated regions of the ceramic-slag reaction phase, which were about 3 µm in extent, were present along the entire upstream surface. Results of an

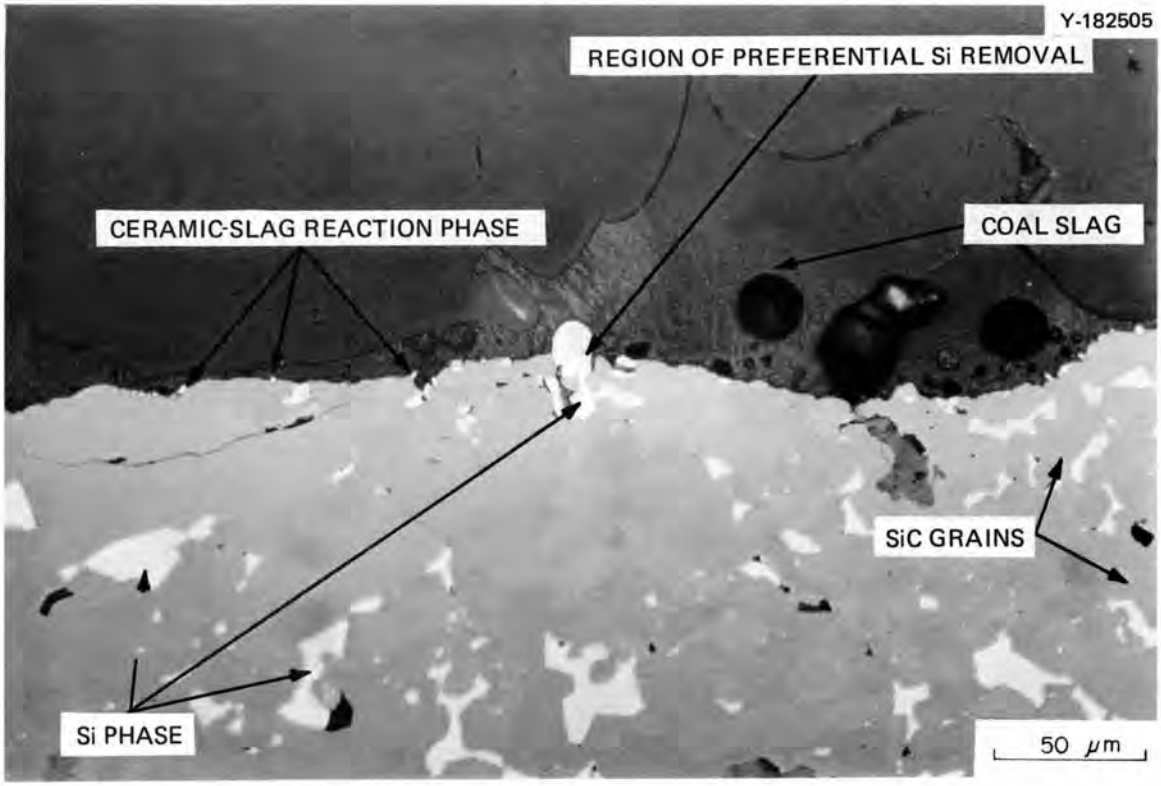

Fig. 32. Upstream surface of postexposure KT SiC illustrating location of ceramic-slag reaction phase.

elemental x-ray analysis of these regions again revealed high concentrations of iron and nickel, similar to results discussed previously for other SiC ceramics. Figure 32 also gives some indication that the free silicon phase in the KT SiC microstructure was preferentially attacked by the coal slag. However, this behavior was usually confined to a limited number of areas along the tubular surface and, therefore, did not dominate the surface degradation process. In fact, a high magnification SEM examination of the ceramic-slag interface in the post-test KT SiC suggested that the corrosion rates of the silicon phase and the adjacent SiC grains were quite comparable. A similar degradation behavior was observed in the post-test NC 430 SiC. There was also no evidence of any preferential surface recession occurring in the joint region in the tubular specimen of this material.

Further microstructural analyses of the KT and NC 430 SiC materials indicated that the isolated regions of ceramic-slag reaction phase, which formed at the tube surfaces, attained a certain maximum size, then were transported away from the surface into the coal slag where they were disrupted by the slag matrix. Again, this behavior is almost identical to that observed for the post-test α-SiC tube. Additional details of the dissolution or disruption mechanism are illustrated in Fig. 33. In particular, Fig. 33(a) is an SEM backscattered image of a particle of the reaction phase in the process of disruption or dissolution, which was observed in the slag on the KT tube. Based upon present data, the specific mechanism is unknown whereby the primary corrosion product phase reacts with the liquid siliceous coal slag. It is apparent, however, that during the dissolving process, extensive penetration of the primary reaction phase regions by the coal slag occurred only at selective locations. This non-uniform attack ultimately resulted in the fragmentation of the original particle. These smaller fragments were then subject to further reaction with the siliceous slag. The disintegration of these reaction-phase particles again suggests that they were highly unstable in the presence of the chemical constituents in the coal slag once they left the vicinity of the SiC tube surface. Figure 33(a) also reveals the presence of a zone around the dissolving particle which is essentially devoid of the crystals which normally coexisted with the siliceous melt. Therefore, it is likely diffusion processes* of some type were involved in the reaction mechanism which led to the disappearance of the primary corrosion product phase. Since there was evidence that the radius of the depleted zone was proportional to the associated particle size, the required diffusion of certain species inward to the corrosion product particle may have limited the disintegration rate when the particle was large. This probably explains why many of the larger particles of the ceramic-slag reaction product were only partially dissolved by the coal slag. Finally, it should be mentioned that the reaction-product particle shown in Fig. 33(a) contained heavy

*Diffusion through the reaction zone would be required for the transport of the reactants (coal-slag constituents) to the particle site and possibly the transport of the reaction products away from the region.

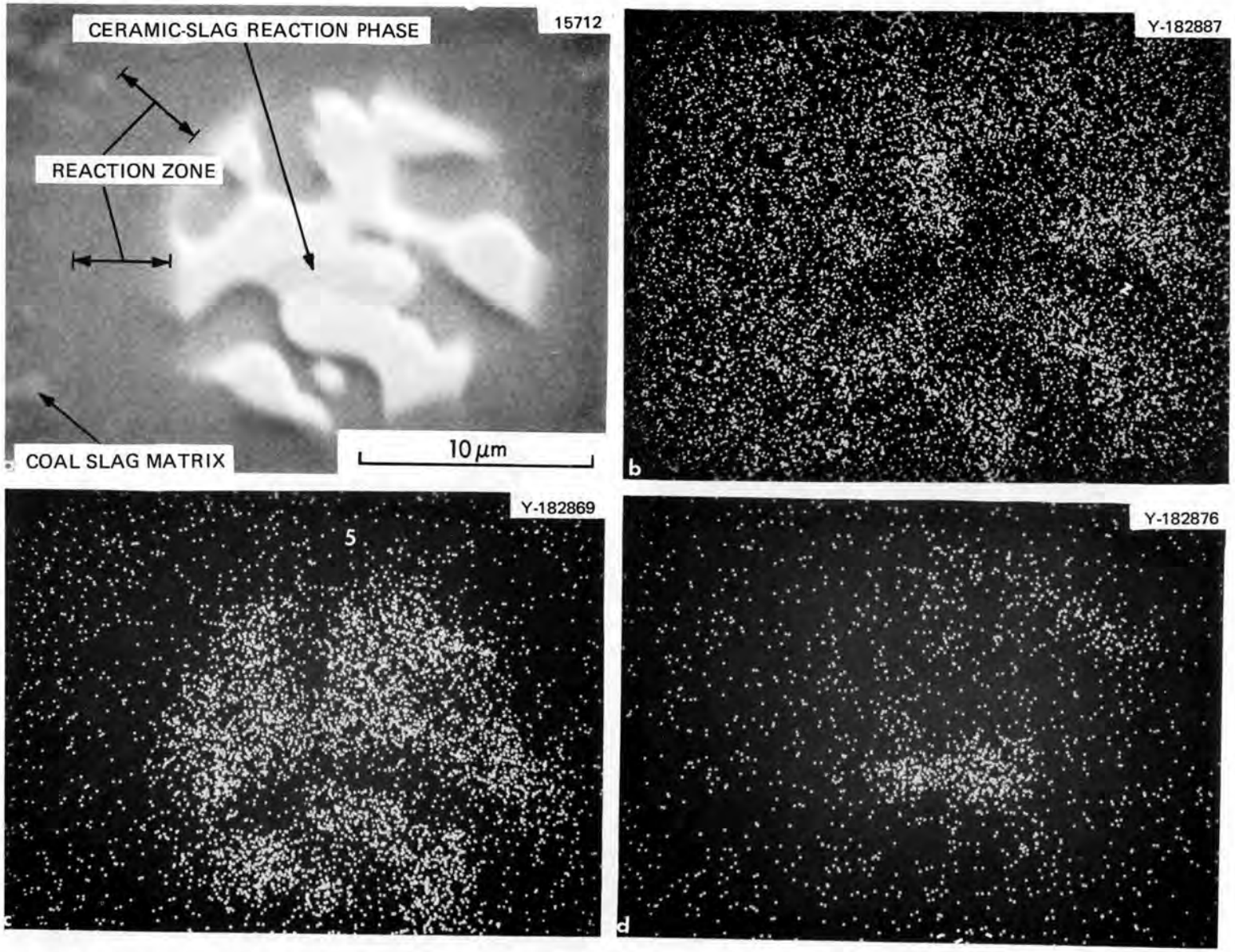

Fig. 33. (a) SEM backscattered image of dissolving particle of ceramic-slag reaction phase present in coal slag for KT SiC tube. Elemental distributions of Si, Fe, and V are shown in (b) through (d), respectively.

elements consisting primarily of Si, Fe, Ni and V. The vanadium was inhomogeneously distributed within the particle and may have come from the No. 6 fuel oil.[6] The distributions of the Si, Fe, and V are illustrated in Fig. 33(b) through (d), respectively. It is apparent that the primary reaction product has a lower silicon concentration than the surrounding siliceous slag, while the iron concentration in this material is much higher than in the surrounding melt. Also, note that the iron concentration in the previously noted depleted zone is much lower than in either the primary reaction phase or the siliceous melt some distance away from the particle. This appears to contradict previous x-ray diffraction results which suggested that the reaction phase was composed of an iron (or nickel) silicide. Reasons for this discrepancy are not clear.

The reaction process at the slag-ceramic surface interface in the SC-2 SiC was slightly different from that in the other siliconized silicon carbides. Although surface corrosion did occur in this material, the high-reflectivity ceramic-slag reaction phase, which was generally characteristic of the corrosion process, was not observed in the post-test SC-2 microstructure (Fig. 34). It is possible that the extremely small SiC grain size in the SC-2 resulted in a limit to the size of the primary reaction product particles which precluded their observation at the tube surface. If these particles were very small for the SC-2 case, they would experience rapid dissolution by the coal slag. Figure 34 also reveals the existence of several gas bubbles which are adjacent to corrosion pits in the upstream surface. The size of each bubble varies directly with that of the associated pitted region. This behavior is consistent with most reported SiC corrosion mechanisms,[13,14] since they typically involve the evolution of CO_2 or CO gas. The cracks shown in Fig. 34 were probably introduced during the preparation of the metallographic specimen and are, therefore, artifacts. However, similar cracking was not generally observed in the as-received metallographic samples. Therefore, it is possible that the localized slag-ceramic reaction significantly weakened the tubular surface regions making them susceptible to fracture during metallographic polishing. The presence of residual thermal stresses generated as a result of a thermal expansion mismatch between the ceramic and coal slag could also have facilitated the observed cracking.

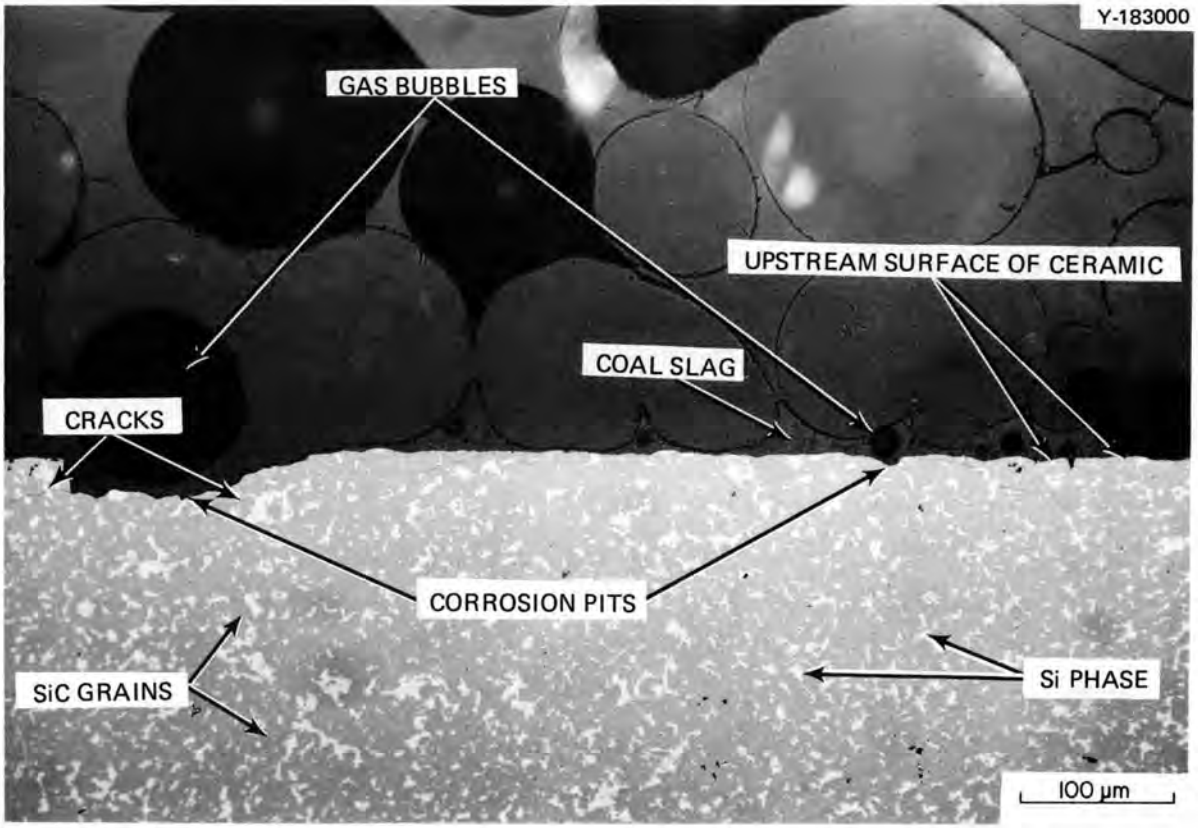

Fig. 34. Upstream surface of post-test SC-2 SiC illustrating apparent absence of preferential attack of silicon phase by coal slag.

As shown in Table 8, the concentrations of several elements including Al, Ca, Fe, Ni, Na and Ti were substantially increased in the post-test NC 430 and KT SiC tubes. Therefore, during high-temperature exposure, these elements, which were associated primarily with the constituents in the coal slag, underwent selective diffusion into the ceramics. It is possible that the presence of the free silicon phase in the microstructure of these two ceramics facilitated this transport process. In particular, the tendency of silicon to form low-melting eutectics with metallic elements at elevated temperatures could have provided a sufficient driving force for the diffusion of iron or nickel into either the KT or NC 430 SiC. Finally, the x-ray data for the post-test siliconized silicon carbides (Table 9) reveal the presence of unidentified phase(s) in addition to those detected in the as-received materials.

AD 998 Al_2O_3

The microstructure of the as-received aluminum oxide is illustrated in Fig. 35. The dense fine-grained structure is typical of the AD 998 material. Figure 35 also reveals a high degree of texturing in the Al_2O_3 grains along the outer surface. These grains, which are slightly elongated, appear to be preferentially oriented such that the long dimension lies parallel to the tube circumference. This texturing apparently resulted during the green-state fabrication of the material. Finally, as shown in Table 9, the major chemical phase in the AD 998 was corundum (α-Al_2O_3).

The microstructural examination of the Al_2O_3 tube following CRAF Test 3 indicated that the nature of the surface degradation resulting from exposure to the coal slag was significantly different from that for the silicon carbides. As shown in Fig. 36, the coal-slag appeared to uniformly react with the entire Al_2O_3 surface resulting in the formation of a 25-μm-wide reaction zone. However, the primary phase formed in the reaction zone was unstable in the presence of the coal slag as indicated by its limited thickness and apparent fragmentation at its interface with the siliceous melt. Therefore, the surface corrosion of the Al_2O_3 was apparently characterized by the following steps: (1) reaction between the alumina and the coal slag to form a primary reaction product, (2) subsequent reaction of this product with the overlying slag, and (3) further reaction at the alumina-slag interface. The primary reaction or corrosion product was relatively uniformly distributed on the Al_2O_3 surface in contrast to the more localized reaction mode observed for the SiC ceramics. Figure 36 also shows numerous blocklike crystals in the coal-slag matrix. These crystals were quite similar to those observed in the massive slag deposits remaining on the tubular elements studied in CRAF Test 2. These blocky crystals were not observed in the slag on the postexposed SiC tubes.

Additional insights into the chemical nature of the microstructural features discussed above were obtained from the x-ray elemental analysis performed in conjunction with the SEM examination. An SEM backscattered micrograph of a typical upstream surface region in the postexposed Al_2O_3 tube is illustrated in Fig. 37(a). The major elements with masses greater

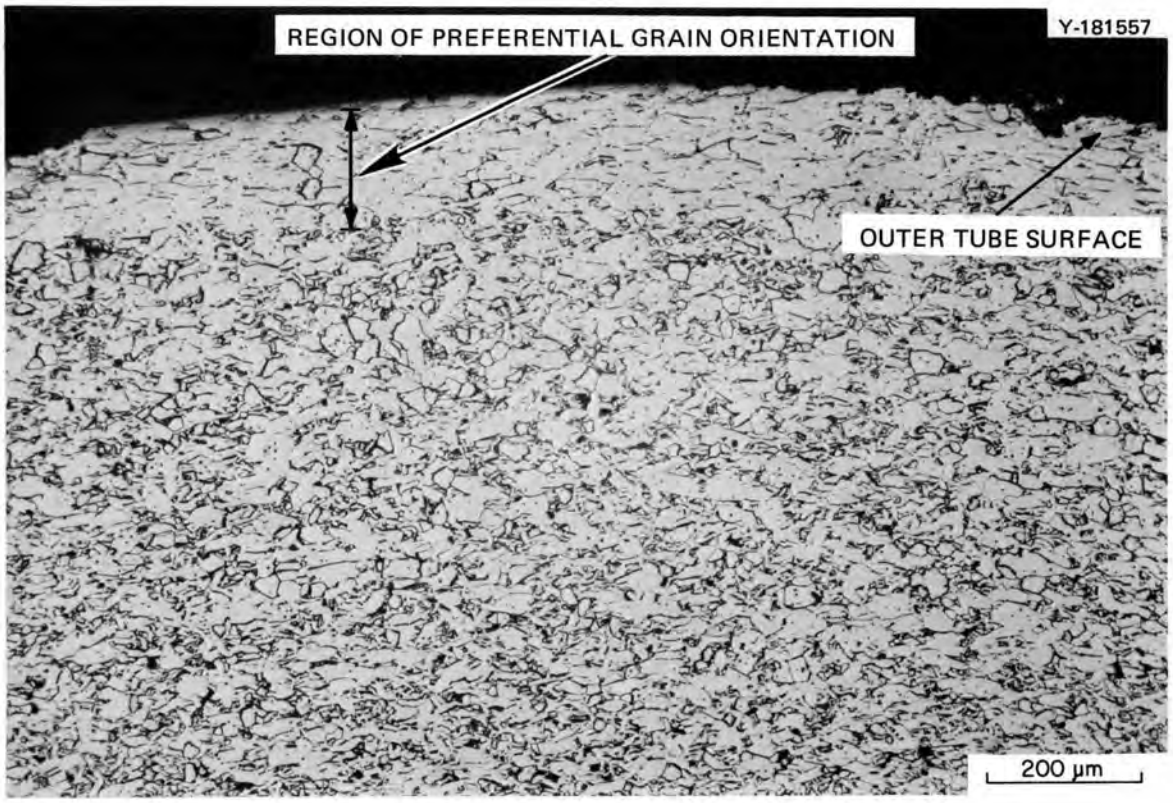

Fig. 35. Typical microstructure of as-received AD 998 Al_2O_3 .

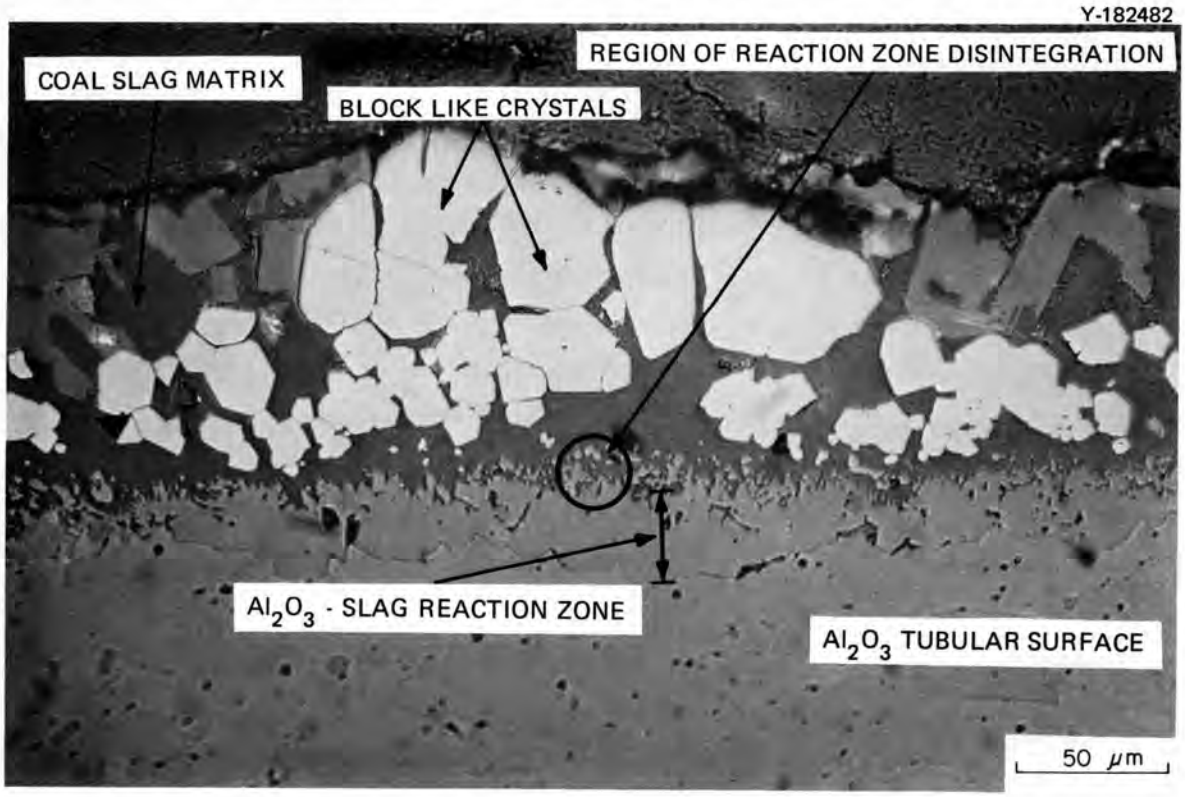

Fig. 36. Upstream region in post-test Al_2O_3 illustrating formation of ceramic-slag reaction phase.

than Na associated with this area were Al, Si, Ca, and Fe, the distributions of which are shown in Fig. 37(b) through (e), respectively. It is apparent that the Al_2O_3 slag reaction zone contained primarily Al and Fe. Although not indicated in Fig. 37, minor amounts of Ni were also present in the reaction zone. It is likely that the reaction between the coal slag and alumina led to the formation of an iron-nickel aluminate compound. This behavior was distinctly different from that observed in CRAF Test 2 in which a COM having an acidic-ash coal was burned in the combuster.[6] In the CRAF Test 2 exposure, massive coal-slag deposits bonded to the Al_2O_3 via the formation of a 6 to 12 m aluminosilicate reaction zone. This variation in behavior was probably due to the rather large differences in the coal-ash chemistry associated with the coals in the respective COM fuels. In the present study, for example, the large concentration of Ca* in the coal ash promoted the formation of a calcium silicate in the slag matrix, thereby reducing the availability of SiO_2 for reaction with the alumina tube. A similar Fe-Ni-Al (hercynite) layer was observed in postexposed alumina tubes used in a previous long-term exposure (CRAF Test 1) involving only the combustion of a No. 6 fuel oil.[5] During the high-temperature exposure in Test 1, fluid nodules having a morphology almost identical to those observed in the present experiment, formed on all the tubular elements. However, in CRAF Test 2, the slag deposits were quite viscous at the exposure temperature. Therefore, it is possible that the high fluidity of the coal-slag in the present experiment also tended to promote the formation of the iron-nickel aluminate as a primary corrosion product.

The information in Fig. 37 also indicates that the large blocklike crystals present in the coal slag contained high concentrations of iron. As previously discussed, these crystals were observed in the slag deposits remaining on all tubular elements used in CRAF Test 2. However, in the present study, the blocklike crystals were only present in the coal slag on the post-test Al_2O_3. It is possible that their formation resulted from the disintegration of the Ni-Fe-Al compound formed at the Al_2O_3-slag interface.

---

*The weight percent of CaO in the coal ash was 25.12 in CRAF Test 3 and 2.72 in CRAF Test 2.

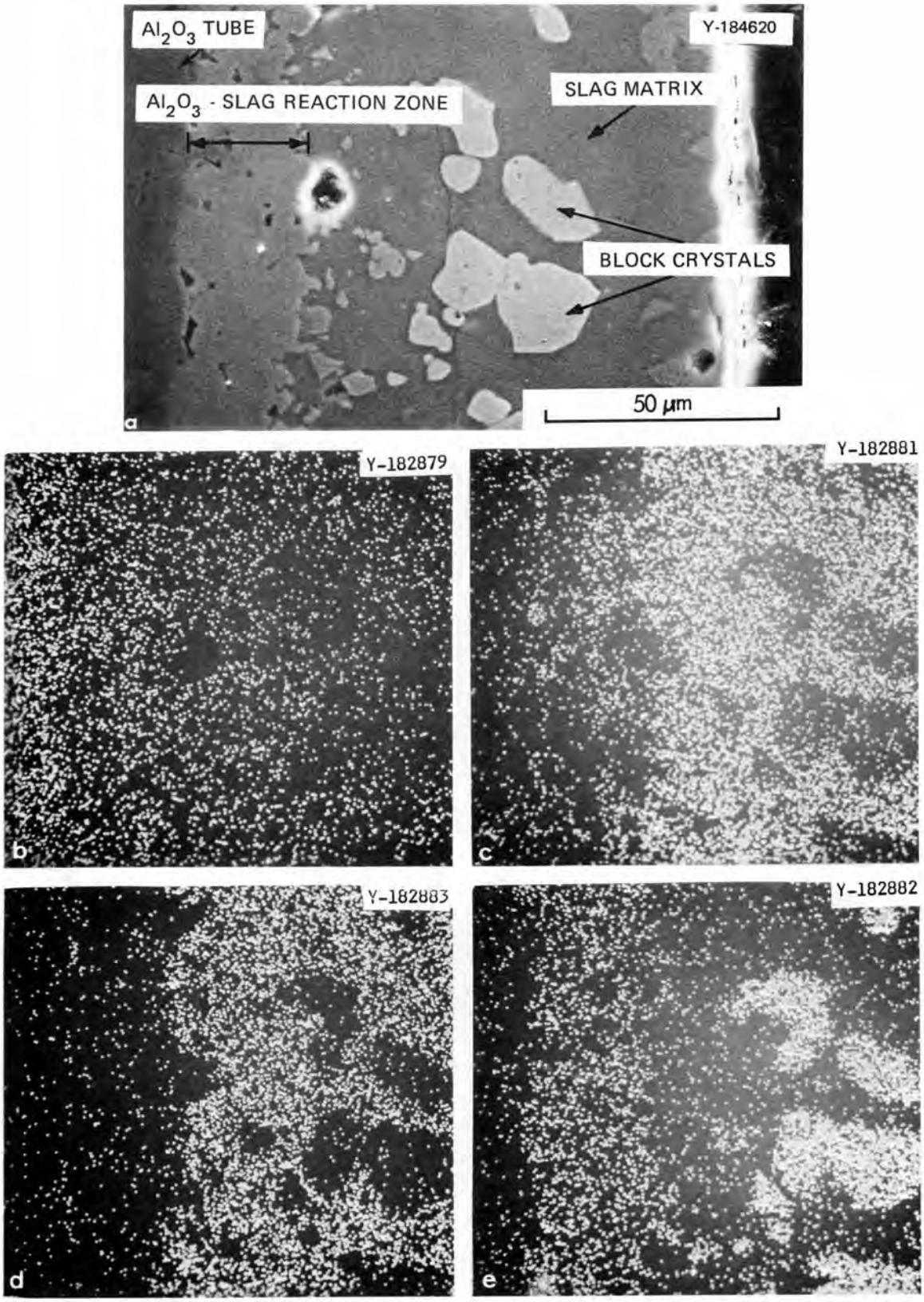

Fig. 37. Results of x-ray elemental analysis. (a) Typical upstream region in post-test Al_2O_3 and distributions of (b) Al, (c) Si, (d) Ca, and (e) Fe.

The α-Al_2O_3 or corundum structure was the major phase detected in the post-test alumina tubes (Table 9). The unidentified phase(s) were presumably the primary corrosion product formed at the Al_2O_3-slag interface.

Sialon Ceramics

Since the microstructures of all three pretest sialons were similar, only the GE-128 material will be discussed. For example, Fig. 38(a) shows a typical cross-sectional view of the as-received GE-128 sialon including the outer tube surface. It is apparent that, within the tube interior, the sialon ceramic was characterized by considerable porosity plus numerous inclusions of a high-reflectivity phase. Subsequent microprobe analyses revealed major concentrations of Mg, Al, Si, and Fe [(Fig. 38(b)] within the ceramic. The presence of these elements would be expected on the basis of the green-state sialon compositions given in Table 2. As shown in Fig. 38(c), the high-reflectivity inclusions contained minor amounts of Ti, Cr, and Ni in addition to those elements detected in the sialon matrix. These metallic elements were evidently introduced into the GE-128 as impurities during the fabrication of the tube. Finally, Fig. 38(a) reveals a region of structural inhomogeneity along the outer tube surface. This inhomogeneous region generally appeared as isolated patches along the outer diameter and a narrow, continuous layer along the inner diameter. Furthermore, the microprobe analysis indicated that its elemental composition was similar to that of the sialon matrix. Since neither oxygen nor nitrogen can be detected in such analyses, it is possible that the regions resulted from variations in the local concentrations of these elements.

As shown in Table 9, the major phases in all three sialons were β-Si_3N_4 and β'-sialon ($Si_2Al_4O_4B_4$). An additional compound, $Si_3Al_{2.67}N_4O_4$, was also detected in the GE-128 material. Identification of the phases in all three sialons was complicated by lack of available x-ray data for the wide range of possible sialon compositions. This explains why several of the phases in the GE-130 sialon could not be identified.

Examination of the exposed sialon materials indicated that the corrosion behavior was quite similar in all three of the sialon formulations.

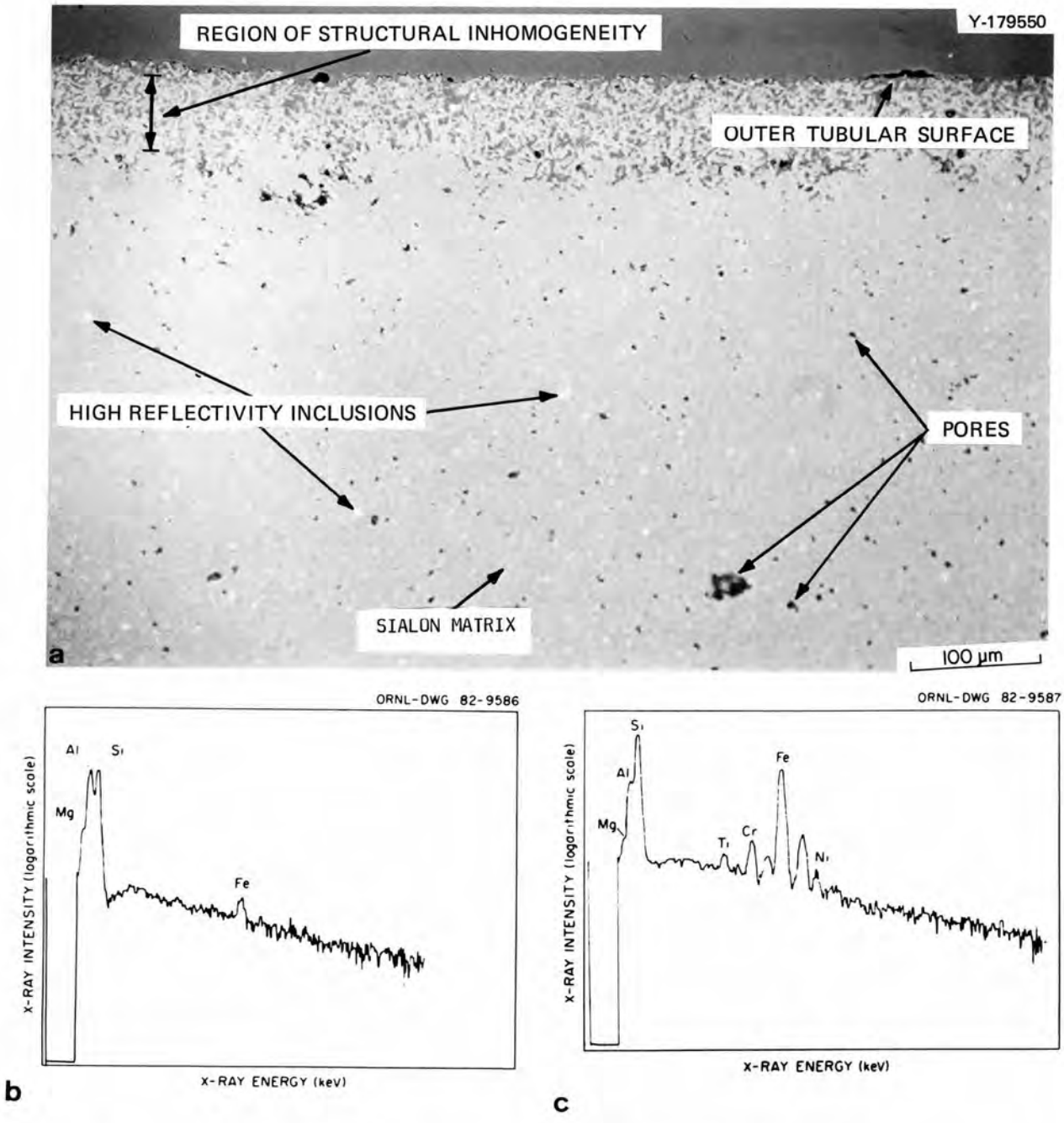

Fig. 38. (a) Bright-field micrograph of pretest GE-128 sialon illustrating microstructural characteristics typical of all as-received sialon materials. Results of microprobe analyses of slag matrix and high-reflectivity inclusions are shown in (b) and (c), respectively.

Therefore, only the GE-128 sialon will be discussed here. There was evidence that the corrosion of the sialon occurred via a localized reaction at the sialon coal-slag interface. For example, Fig. 39(a), which is a typical upstream region in the GE-128 sialon tube, reveals the presence of an apparent reaction zone at the ceramic-slag interface. The appearance of numerous pores in the vicinity of this reaction zone suggests that the reaction was accompanied by large amounts of gas evolution. The inner tubular surfaces of all three sialons tended to oxidize during the high-temperature exposure. This oxide layer, illustrated in Fig. 39(b) for the GE-128 sialon, was essentially identical to that formed along the outer surface of the GE-128 material in the CRAF Test 2 study.[5]

The x-ray diffraction studies (Table 9) revealed minor changes in the type of phases present in the postexposed sialon materials. In the GE-128 sialon, α-$Mg_2Al_4Si_5O_{18}$ was detected in addition to the phases present in the as-received material. It is likely that the magnesium-aluminum silicate was associated with the oxide scale observed along the inner tubular surface. Similar results have been obtained in previous studies.[5,7] Also, unidentified phases were found in the post-test GE-129 and -130 specimens.

Coal Slag

Previous metallographic and SEM observations revealed considerable internal structure within the slag nodules which were deposited upon the various post-test tubular elements. Susequent examination of these slag nodules indicated that the microstructure consisted of large pores ranging from 10 to 250 μm in diameter and elongated crystals dispersed in a glassy-type matrix. These features are illustrated in Fig. 40 which is a bright field micrograph of a slag nodule on the postexposed α-SiC. It should be noted that additional metallographic examinations of the slag deposits on different tubes revealed a substantial variation in the distribution and size of the associated crystals. In the case of the α-SiC, these crystals were only present near the outer surface of the slag nodules (the region adjacent to the combustion atmosphere). Furthermore, the crystallites generally exhibited a rather complicated dendridic pattern. Only in a few areas were there crystals with a blocklike morphology. However, as shown in Fig. 41, the slag crystals associated with the

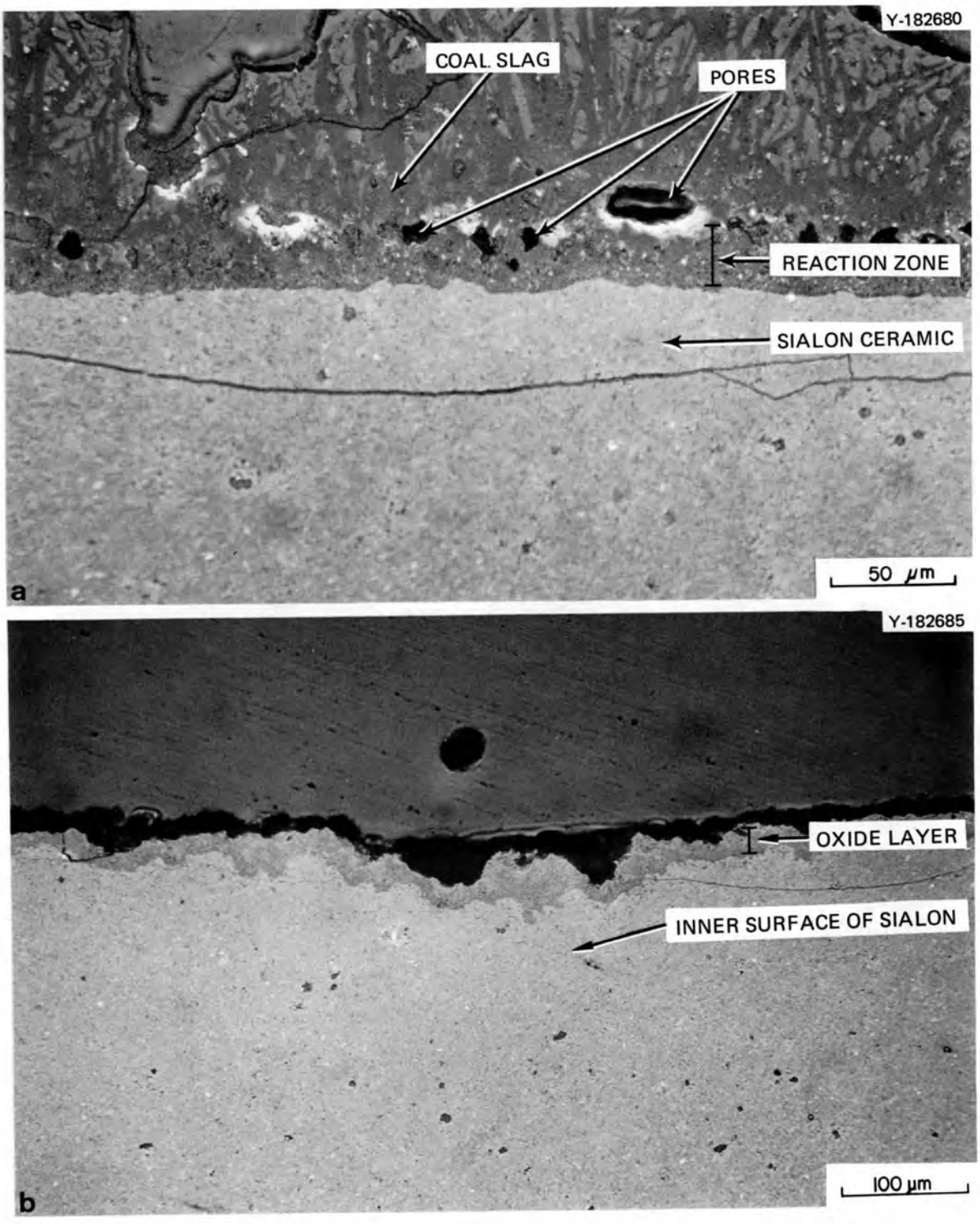

Fig. 39. Bright field micrographs of post-test GE-128 sialon illustrating (a) reaction zone along upstream surface and (b) oxide layer formation along inner tubular surface.

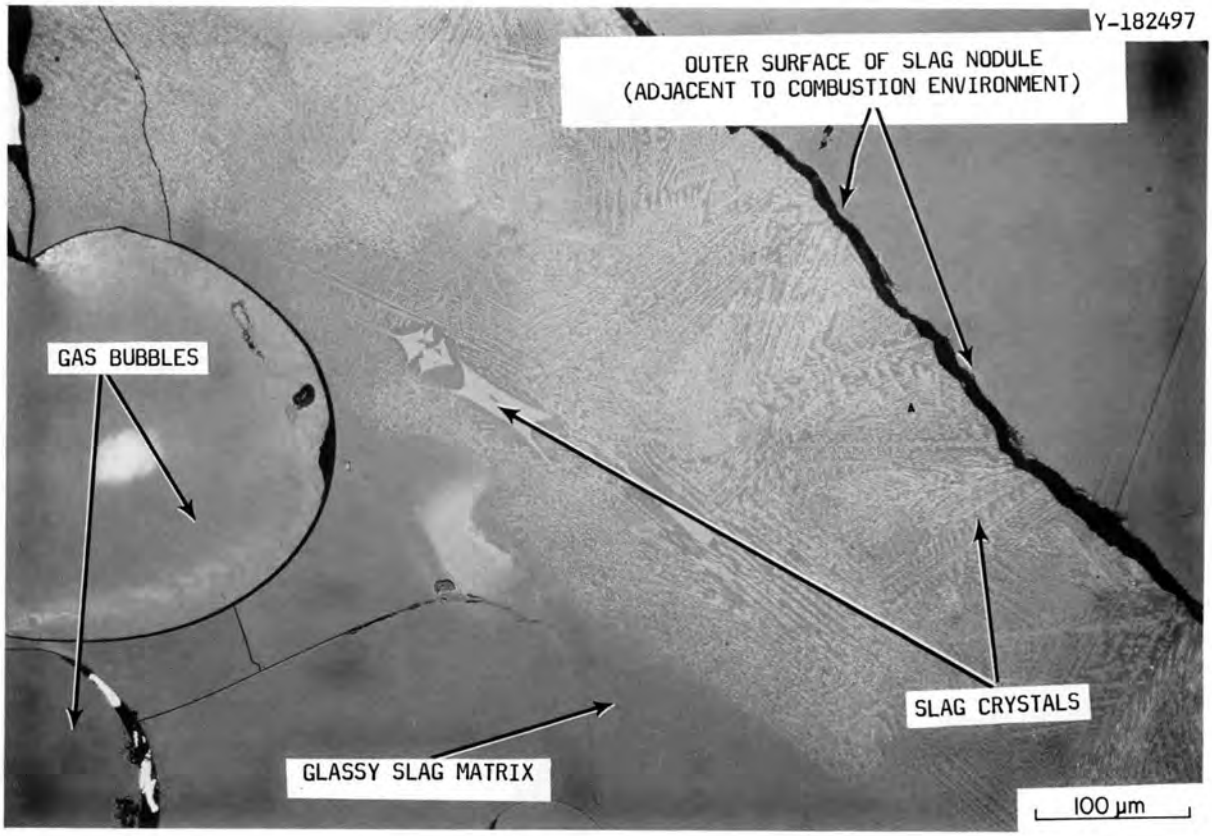

Fig. 40. Typical microstructure of coal-slag nodule on postexposed α-SiC tube.

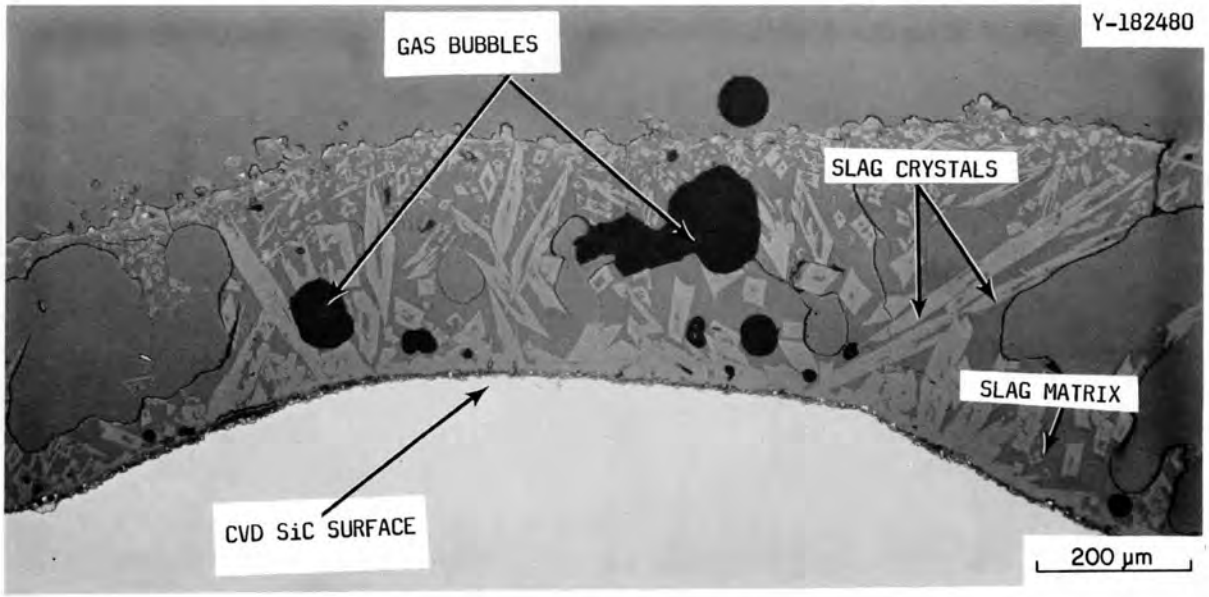

Fig. 41. Micrograph of coal-slag deposit on postexposed CVD SiC illustrating presence of elongated slag crystals.

post-test CVD tube appeared as discrete rhombohedral shaped units which were distributed throughout the slag nodule. In addition, many of the crystals contained small internal regions which were apparently composed of slag matrix material. Reasons for the wide variability in the morphology and distribution of the crystallites in coal slag from the various ceramic tubes are currently unknown.

The principal elements in the slag as revealed by x-ray elemental analyses were Ca, Si, Al, Fe, Mg plus smaller amounts of Ti, Na, and K. The relative concentrations of these elements did not vary significantly between the slag matrix and the various crystallites. This suggests that the crystals were precipitated from the coal-slag matrix during either the high-temperature exposure or during cool down from the exposure temperature. Further information concerning the concentration of the various elements in the slag were obtained from wet chemical analyses.* The results, which are given in Table 10, again confirmed that large amounts of Si, Fe, Al, Ca and Mg were present in the coal slag. With the exception of the Si and Ca, the concentrations of the equivalent oxides in the coal slag were in good agreement with the respective values determined from the original ash analysis of the coal (Table 10). During the exposure, however, there was a tendency for the equivalent SiO_2 concentration to increase while both the CaO and SO_3 decreased. The SO_3, being highly volatile, would be expected to be depleted from the ash during the combustion and carried away as SO_2 in the combustion gas. Despite these variations, the general similarity between the coal-slag and coal-ash compositions strongly suggests that the chemical species responsible for the degradation of the tubular elements were associated with the coal ash and not the No. 6 oil used as a carrier for the coal to the burner. Consequently, the use of the COM fuel to study effects of the coal combustion products upon the chemical and structural stability of candidate ceramic HX materials was quite successful. Finally, the x-ray diffraction studies (Table 9) indicated that the major phase in the slag was a calcium silicate in which the Si was partially replaced by Al and the Ca partially replaced by Mg, Fe, Al and Ti. The present results do not permit determination of whether the calcium

*Wet chemical analysis by Spectrochemical Labs., Pittsburgh, Pa.

Table 10. Results of wet chemical analysis of coal slag samples.

Concentration, wt %		
Equivalent oxide	Coal slag	Vendors' ash analysis
SiO_2	45.77	24.47
Fe_2O_3	10.72	8.87
Al_2O_3	14.17	12.81
CaO	18.75	25.12
MgO	7.08	8.35
NiO	0.40	N.D.
SO_3	0.055	15.35
P_2O_5	0.51	0.53
Na_2O	1.10	0.76
K_2O	0.52	0.42
TiO_2	0.27	0.77
SrO + BaO	0.16	0.40
Mn_3O_4	N.D.	0.11
V_2O_5	0.03	N.D.[a]
LOI[b]	0.17	N.D.[a]
Base/acid	0.63	1.14

[a]N.D. means not detected.

[b]Loss on ignition.

silicate crystals were present in the slag at the exposure temperature or crystallized from the melt during cool down from the exposure temperature.

Thermal Expansion

The thermal expansion of materials considered for use in high-temperature HXs is very important because stresses produced in these components due to temperature gradients normally existing within an HX are directly related to the thermal expansion. In addition, a major concern in the use of structural ceramics in HXs is the ability of the structure to withstand stresses generated by thermal expansion under thermal transient conditions. The thermal expansion of specimens cut from the ceramic tubes was measured in a differential push rod dilatometer* against an NBS sapphire reference specimen in air using a heating rate of 0.05° c/s (3°C/min).

As shown in Figs. 12 and 13, a total of three thermal expansion specimens were prepared for each material, one from an as-received tube and two from a postexposed tube. The two specimens from the exposed tube were cut as shown in Fig. 13 with the long axis parallel with the tube axis. One specimen each was cut from the upstream side and the downstream side of the exposed tube.

Previous thermal expansion data obtained for structural ceramic materials were reported following the combustion gas exposures in CRAF Tests 1 and 2. These earlier measurements were obtained using a push rod dilatometer† whose design did not permit continuous comparison with a reference standard specimen. Using this method to obtain thermal expansion values for the specimen, it was necessary to subtract the expansion of the dilatometer push rod structure from that of the specimen. For the case of Al_2O_3 dilatometer hardware, this value can be a substantial number relative to that of the specimen expansion. Due to minor differences in

---

*Dilatronic System, Model IIS, product of Theta Industries, Inc., Port Washington, N.Y.

*Harrop thermal dilatometric analyzer, Model TD-716, product of Harrop Laboratories, Columbus, Ohio.

push rod alignment from specimen to specimen, it was very difficult to accurately determine the value of small differences in $\Delta L/L$ between different specimens. Measurements of the thermal expansion, $\Delta L/L$, for a variety of specimens from these earlier combustion gas exposure experiments using this particular dilatometer indicated that the exposure resulted in significant changes in the thermal expansion of both SiC and Al_2O_3 based ceramics. For example, the results from the CRAF Test 2 indicated that the thermal expansion of the ceramic at a given temperature increased more when it was located on the upstream side of the tube than when it was located on the downstream side. These results, although reproducible using the non-reference standard containing dilatometer, were troublesome for several reasons. For the thermal expansion of a given material to change at a given temperature, it is necessary for either a phase change to occur in the solid, or for the elemental impurity concentrations in the major phases to change to such an extent that the impurities substantially affect the atomic vibrational modes in the solid which determine the thermal expansion. The compositional phase and microstructural analyses results obtained for the exposed ceramics from Tests 1 and 2 did not indicate that the substantial phase or compositional changes had indeed occurred. This left the explanation for the observed thermal expansion changes in doubt. Therefore, several thermal expansion samples from CRAF Test 2, including as-received and post-test (upstream) specimens, were remeasured using the newly acquired differential push rod dilatometer.

Results for two of the specimens of KT SiC from CRAF Test 2 are shown in Fig. 42. The data show that $\Delta/L_0 = 0.44\%$ for the as-received ceramic at 1000°C, and that the upstream exposed specimen had essentially the same expansion as the unexposed material. The $\Delta L/L_0$ values at 1000°C obtained earlier for the same specimens, using the nondifferential dilatometer, were 0.48 and 0.56%, respectively.[6] These earlier values apparently contained errors which made the earlier reported $\Delta L/L$ differences due to coal-slag exposure appear significant. Similar duplication measurements on the α-SiC, CVD SiC, and AD 998 Al_2O_3 specimens from CRAF Test 2 in the differential dilatometer show that the differences in the expansion curves (shown in Figs. 60–63 of ref. 6) were artifacts introduced by the dilatometer previously employed. In fact, subsequent measurements with the

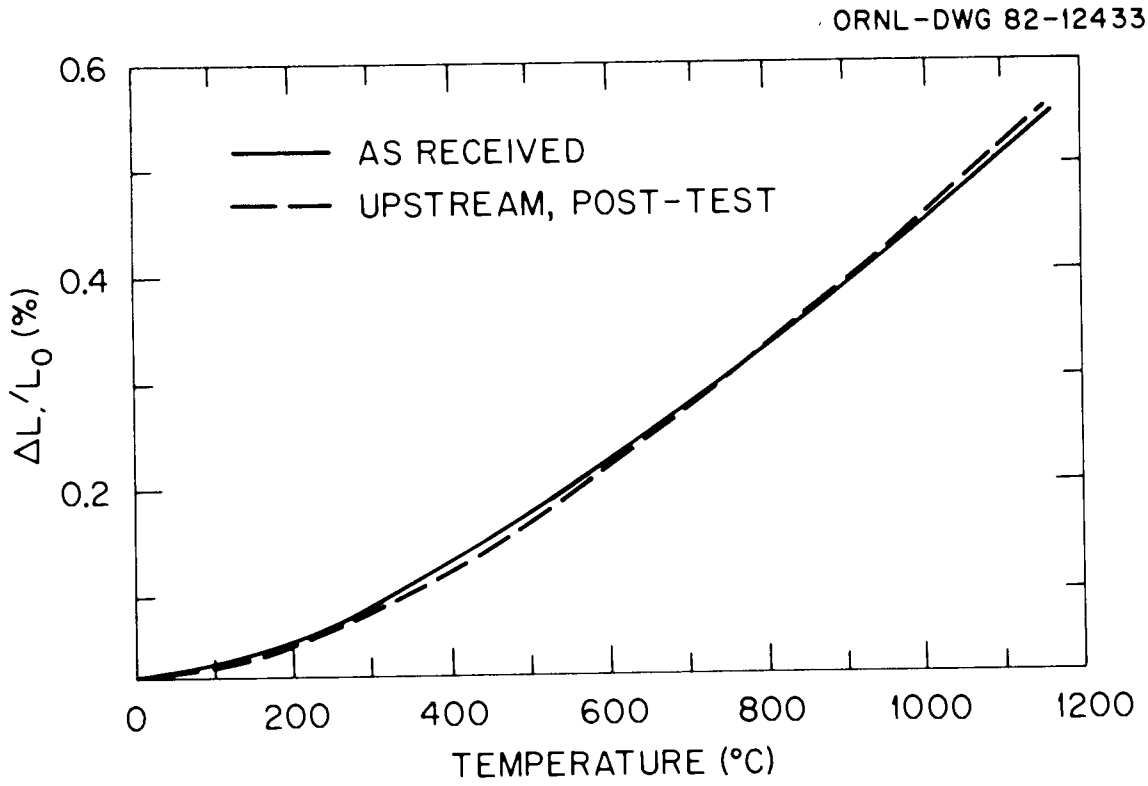

Fig. 42. Additional tests on KT SiC from CRAF Test 2 show no significant differences in thermal expansion between as-received and upstream specimens.

differential dilatometer revealed no significant thermal expansion changes in any of these CRAF Test 2 samples due to the long-term exposure.

Figure 43 shows the thermal expansion in terms of $\Delta L/L$ for three CRAF Test 3 KT SiC specimens having histories as noted in the figure. The accuracy of these measurements is estimated conservatively to be about 10%. From Fig. 43, therefore, the conclusion can be made that for the KT SiC ceramic there was no significant change of the thermal expansion due to the coal-slag exposure or due to specimen location in the exposed ceramic tube.

Thermal expansion curves for three CVD SiC specimens from the present experiment are shown in Fig. 44. In this case, no significant $\Delta L/L$ changes were observed. Interestingly, the $\Delta L/L_0(\%)$ values for this material at 524 and 1000°C were 0.20 and 0.44%, respectively, the same as observed for KT SiC. This result suggests that the expansion of the KT SiC specimens was controlled by the expansion of the SiC phase, since the thermal expansion values were identical.

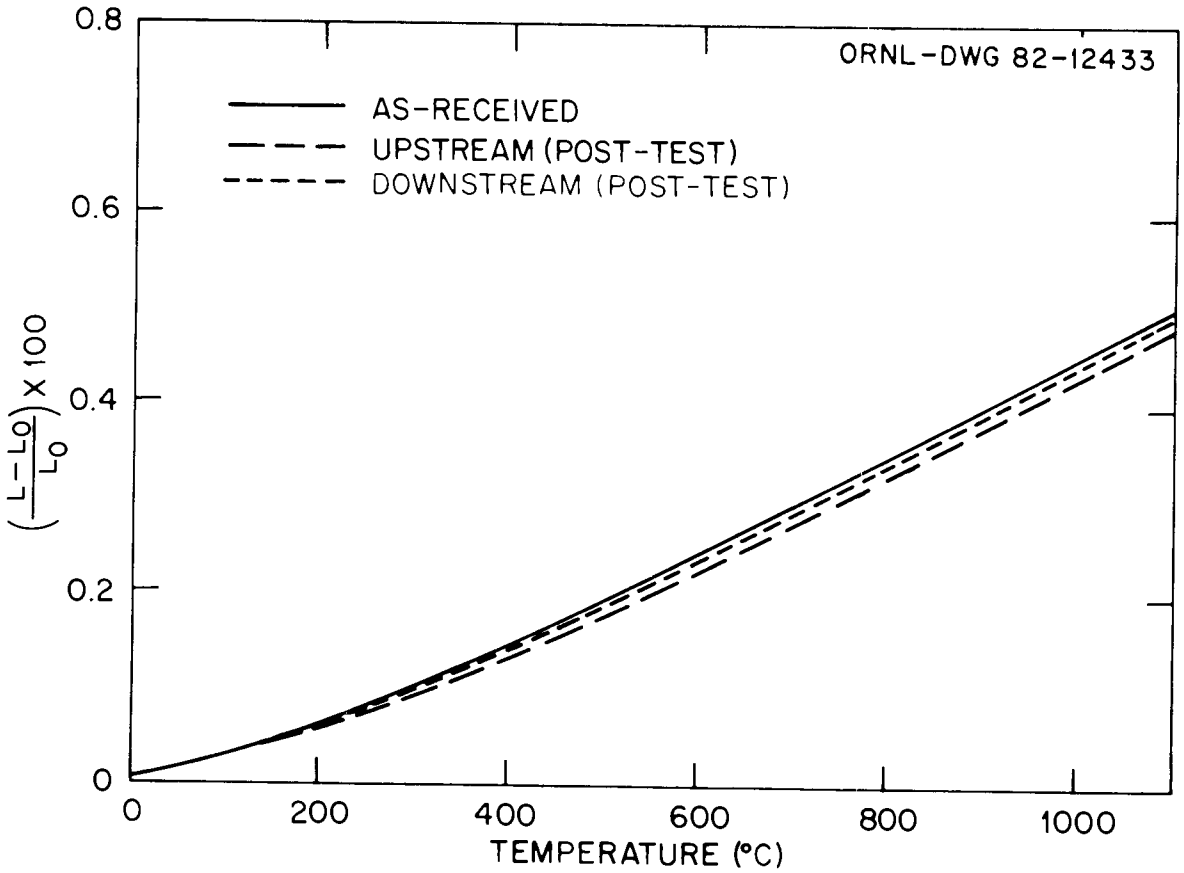

Fig. 43. Thermal expansion of KT SiC following long-term test exposure.

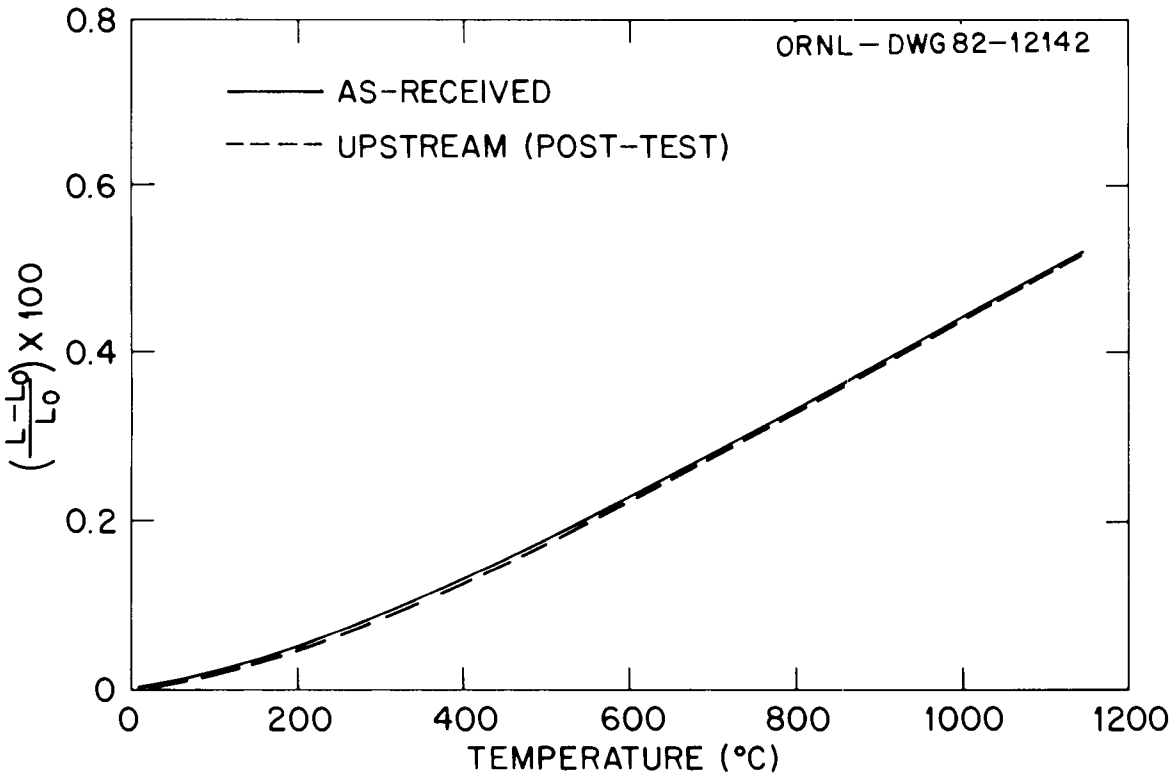

Fig. 44. Thermal expansion of CVD SiC before and after test exposure.

Thermal expansion curves for three specimens of sintered α-SiC are shown in Fig. 45. As for the SiC ceramics discussed previously, there was not a significant change in $\Delta L/L_0$ due to the exposure, with the $\Delta L/L_0$(%) values for as-received, exposed upstream, and exposed downstream specimens at 1000°C being 0.44, 0.44, and 0.43 %, respectively. The $\Delta L/L_0$(%) value for the as-received α-SiC at 524°C was 0.203, the same as for the KT and CVD materials.

Thermal expansion curves for three specimens of the AD 998 Al_2O_3 ceramic are given in Fig. 46. For this material, there was no significant difference in the thermal expansion of the three specimens with the upstream and downstream values being superimposed upon each other. The $\Delta L/L$ value of 0.787% at 1000°C illustrates the much higher thermal expansion of Al_2O_3 compared to SiC, which at this temperature is 78.8% greater for Al_2O_3 than SiC, based upon the SiC value of 0.44%.

Helium Permeability

The room temperature helium leak rate was determined for both the as-received and surviving (uncracked) post-test tubes with the exception of the CVD SiC. Actual measurements were made while maintaining 101-, 247-, and 446-kPa helium pressure differentials across the tube wall. The use of higher pressure differentials resulted in large leak rates through the epoxy resin which was used to attach the required fixturing to the ceramic tubes. The associated measurement apparatus, described in refs. 5 and 6 had a detection limit of 5.0×10^{-16} m^3/s. The resulting helium permeability values are given in Table 11. As indicated in the table, several tubular elements, including α-SiC (tube 2, post-test), Al_2O_3 (tube 2, pre- and post-test), and GE-129 (pretest) had leak rates too high to be measured. It is possible that these materials contained flaws (undetected by the radiographic examinations) which acted as fast diffusion paths for helium diffusion. For the remaining tubes that were measured, the pretest helium leak rates at the 101-kPa pressure differential were near the detection limit. Furthermore, these pretest values increased by, at most, an order of magnitude as the pressure differential was raised to 446 kPa. In the case of measurements for postexposed tubes, the increase in

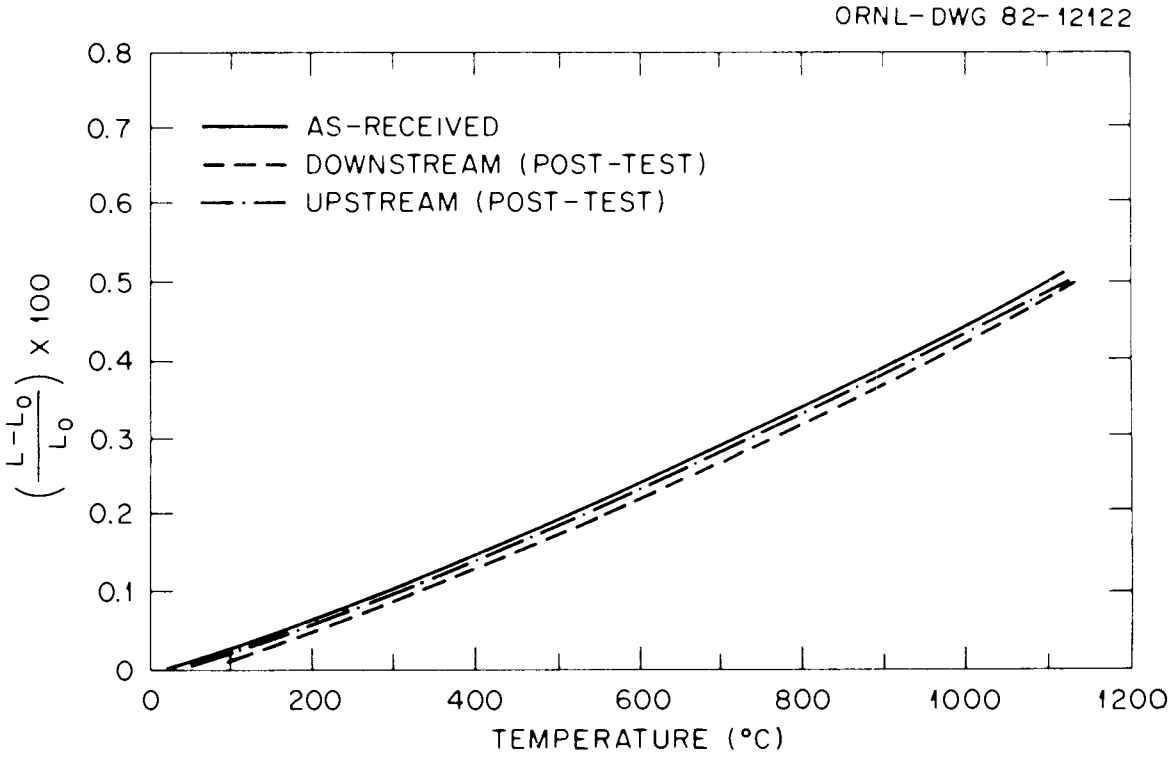

Fig. 45. Alpha-SiC expansion characteristics before and after test exposure.

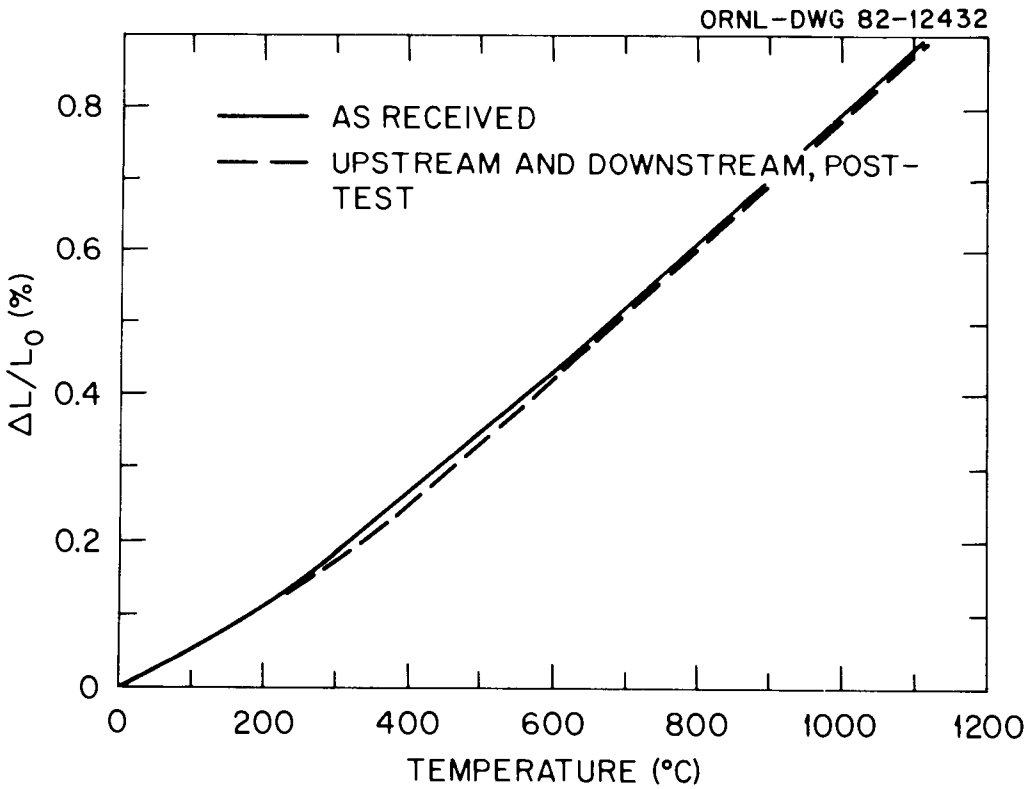

Fig. 46. Expansion characteristics of AD 998 Al_2O_3 before and after test exposure.

Table 11. Room temperature helium permeability data of pretest and surviving post-test ceramic tubes in CRAF Test 3.

Material		He permeability at prescribed pressure differential, m^3/s		
		101 kPa	247 kPa	446 kPa
(A) KT SiC				
Tube 1	Pre	$<5.0 \times 10^{-16}$	$<5.0 \times 10^{-16}$	$<5.0 \times 10^{-16}$
	Post	$<5.0 \times 10^{-16}$	$<5.0 \times 10^{-16}$	$<2.9 \times 10^{-14}$
Tube 2	Pre	$<5.0 \times 10^{-16}$	3.3×10^{-15}	4.6×10^{-15}
	Post	5.2×10^{-15}	2.5×10^{-14}	1.2×10^{-13}
(B) α-SiC				
Tube 1	Pre	$<5.0 \times 10^{-16}$	5.6×10^{-16}	7.0×10^{-16}
	Post	$<5.0 \times 10^{-16}$	2.6×10^{-15}	2.0×10^{-14}
Tube 2	Pre	$<5.0 \times 10^{-16}$	$<5.0 \times 10^{-16}$	9.6×10^{-16}
	Post	*a*	*a*	*a*
(C) SC-2 SiC				
Tube 1	Pre	$<5.0 \times 10^{-16}$	$<5.0 \times 10^{-16}$	6.0×10^{-15}
	Post	4.9×10^{-14}	1.1×10^{-13}	2.4×10^{-13}
Tube 2	Pre	$<5.0 \times 10^{-16}$	$<5.0 \times 10^{-16}$	$<5.0 \times 10^{-16}$
	Post	*b*	*b*	*b*
(D) Al_2O_3				
Tube 1	Pre	$<5.0 \times 10^{-16}$	$<5.0 \times 10^{-16}$	4.6×10^{-15}
	Post	$<5.0 \times 10^{-16}$	$<5.0 \times 10^{-16}$	$<5.0 \times 10^{-16}$
Tube 2	Pre	*a*	*a*	*a*
	Post	*a*	*a*	*a*
(E) CVR SiC	Pre	$<5.0 \times 10^{-16}$	$<5.0 \times 10^{-16}$	$<5.0 \times 10^{-16}$
	Post	$<5.0 \times 10^{-16}$	$<5.0 \times 10^{-16}$	$<5.0 \times 10^{-16}$
(F) NC 430 joint	Pre	$<5.0 \times 10^{-16}$	$<5.0 \times 10^{-16}$	4.3×10^{-15}
	Post	3.3×10^{-14}	4.6×10^{-14}	7.1×10^{-14}
(G) GE 128 sialon	Pre	6.6×10^{-16}	6.6×10^{-16}	3.2×10^{-15}
	Post	*b*	*b*	*b*
(H) GE 129 sialon	Pre	*a*	*a*	*a*
	Post	*b*	*b*	*b*
(I) GE 130 sialon	Pre	$<5.0 \times 10^{-16}$	$<5.0 \times 10^{-16}$	$<5.0 \times 10^{-16}$
	Post	5.6×10^{-14}	*a*	*a*

[a]Tube was too leaky to be measured.

[b]Tube was extensively cracked.

pressure differential resulted in a two-order of magnitude increase in the leak rates for materials such as KT SiC (tubes 1 and 2) and α-SiC (tube 1). The post-test GE-130 exhibited a substantial leakage for pressure differentials greater than 101 kPa. Reasons for these variations are presently unknown. Table 11 indicates that at a given pressure differential, the helium permeabilities for several postexposed materials were greater than the respective pretest values. This behavior may have been due to enhanced helium leakage through the preferentially thinned regions present in the post-test tubes.

FRACTURE STRENGTH

The room-temperature, C-ring, fracture strengths were determined for pre- and post-exposed samples of Al_2O_3, KT SiC, SC-2 SiC, α-SiC, NC 430 SiC, and CVR SiC which had been cut from the tubular specimens. Complete details of the fabrication and testing procedures are given in ref. 5. In the case of the as-received NC 430 SiC tube containing a butt-joint, C-ring samples were prepared from the bulk material some distance from the actual joint. In addition, rectangular bars were fabricated from an NC 430 SiC tube such that the butt-joint was located at the midspan of each bar. These bars were then loaded to fracture in four-point bending to determine the flexure strength of the joint. Several rectangular bars prepared from pretest tubes of α-SiC and Al_2O_3 were also measured in order to provide a comparison between the C-ring and bend-bar fracture strengths. Since the surface condition of the specimens was expected to strongly influence the resulting strength values, several surface treatments were applied. For example, the surfaces of the α-SiC bend samples were ground with a 150 μm silicon carbide wheel prior to testing while the C-ring and bend bar samples* were treated by ball milling all samples in 240-grit silicon carbide for 1 h. No C-ring samples were fabricated from the CVD SiC or sialon materials because the large dimensional variations in the tubes would have necessitated complex and expensive machining processes to obtain samples suitable for testing.

*These were prepared from CRAF Test 2 tubular elements.

The as-received and postexposed C-ring tensile strengths and respective standard deviations calculated for the five SiC materials and Al_2O_3 are given in Table 12. The modulus of rupture or flexure strength values for the KT SiC and Al_2O_3 reported by the vendor is also included. There is considerable difference between the vendor's value and the respective C-ring strengths determined in this work. A primary reason for these differences is that the manufacturer's data were presumably collected from bend-bar fracture specimens fabricated from generic materials which were considerably different from those used in this study. For example, it is likely that the strength-controlling surface flaws in the bend bars used to measure the modulus of rupture flexure strength were different from those in the tubular elements measured here because of variation in the respective processing and fabrication techniques. This was partially confirmed by the fact that the strength of the α-SiC bend bars fabricated from the tubular material was 375.3 ± 42.3 MPa (54.4 ± 6.1 ksi) which is considerably larger than the respective C-ring strength (Table 12). Observations of the C-ring tubular surfaces revealed the presence of large defects that were apparently responsible for the lower strength values. Such defects in the α-SiC bend bars were eliminated during the previously described grinding process.

When special care was taken to obtain surface uniformity for both the C-ring and bend bar samples (as in the case of the Al_2O_3), there was good agreement between the respective strength values: 149.0 ± 11.9 mPa (21.6 ± 1.7 ksi) for the C-ring specimens and 162.5 ± 10.5 mPa (23.6 ± 1.5 ksi) for the bend bars. That the latter strength was slightly larger may partly reflect a volume effect.[15] The as-received C-ring strength for the Al_2O_3 material used in CRAF Test 3 (Table 12) was significantly larger than the respective CRAF Test 2 value.[5] These differences suggest that the nature of the surface flaws in the alumina tubular elements was strongly dependent upon the batch from which the material was prepared by the manufacturer. Table 12 also indicates a substantial variation in the pretest C-ring strengths calculated for the three types of siliconized silicon carbide. The variations were apparently related to differences in the size of the SiC grains present in each material. For example, metallographic examinations revealed that the SiC grain size along the tensile surface

Table 12. Room-temperature C-ring fracture strengths determined for as-received and exposed materials.

Material	Reported by vendor		As received[a]		Exposed[a]		Percent change after exposure[b]
	MPa	(ksi)	MPa	(ksi)	MPa	(ksi)	
Al_2O_3	186	(27.0)	241.3 ± 21.5	(35.0 ± 3.1)	174.3 ± 44.5	(25.3 ± 6.5)	-28
α-SiC			263.5 ± 30.3	(38.2 ± 4.4)	255.2 ± 47.0	(37.0 ± 6.8)	-3
NC 430 SiC			174.4 ± 17.6	(25.3 ± 2.5)	108.6 ± 22.9	(15.8 ± 3.3)	-38
KT SiC (thin wall)	142	(20.0)	202.9 ± 12.8	(29.4 ± 1.8)	107.7 ± 15.3	(15.6 ± 2.2)	-47
KT SiC (thick wall)	142	(20.0)	178.6 ± 8.2	(25.9 ± 1.2)	72.1 ± 21.7	(10.5 ± 3.1)	-60
SC-2 SiC			238.8 ± 23.2	(34.6 ± 3.4)	92.8 ± 51.6	(13.5 ± 7.5)	-61
CVR SiC			85.1 ± 2.6	(12.3 ± 3.8)	71.4 ± 20.3	(10.3 ± 2.9)	-16

[a]Numbers following ± sign represent standard deviation.

[b]Defined as (exposed minus as-received strength) as-received strength.

increased in the order, SC-2 SiC, KT, SiC, and NC 430 SiC. Assuming that the average grain size was directly related to the flaw size, as is often observed in large-grain ceramic materials, one would predict that the strength would increase in the reverse order, which is consistent with the experimental data in Table 12. It is also interesting that the strength of the joint at midspan was 194.6 ± 13.3 MPa (28.2 ± 1.9 ksi) which is comparable with the C-ring strength (Table 8). This behavior is consistent with the fact that the fracture in the flexure bars was generally adjacent to, but not through, the joint region. Therefore, the flexure strength was more representative of the bulk material. Finally, the low pretest C-ring strength value for the CVR SiC probably reflected the microstructural inhomogeneity in this material due to lack of complete reaction between the carbon and free silicon within the interior of the tube.

A comparison of the pre- and post-test C-ring fracture strengths in Table 12 further reveals that the long-term exposure to the coal slag led to significant strength losses in all materials with the possible exception of the α-SiC. It is likely that the localized attack of the coal slag on the tubular surfaces significantly increased the severity of existing flaws, thus reducing the C-ring fracture strength. The fact that the strength loss was greatest for the siliconized silicon carbides may reflect the more frequent occurrence of large corrosion pits in these materials. As indicated previously by the metallographic observations, these pits were formed as a result of preferential removal of the silicon phase. Although the average strength of the post-test α-SiC was only slightly smaller than the as-received material, the standard deviation was increased significantly. This behavior suggests that the width of the flaw distribution was substantially increased during the exposure. The strength degradation phenomenon raises potentially serious questions concerning the use of ceramic HX materials in combustion environments composed of very fluid basic coal slags. For example, in actual HX applications, the tubular elements will be required to support some degree of stress whether it be thermal or mechanical in nature. If the weakening process promoted by exposure to the coal slag is fairly rapid, then the tubes will be subject to premature fracture.

SUMMARY AND CONCLUSIONS

The 240-h exposure of the ceramic tubes to the combustion products of the basic-ash coal resulted in the formation of relatively thin deposits of coal slag on all the tubes. Compared to results reported previously for long-term exposure of similar ceramic tubes to the combustion products of No. 6 oil and an acidic-ash coal, the tubes in the present experiment exhibited extensive and nonuniform wall thinning. The corrosion loss was much more extensive on the upstream side of the tubes which faced toward the combustor than on the opposing downstream side of the tubes. The fraction of the tube wall thickness loss during the exposure was substantial for all of the materials during the 240-h coal-slag exposure with percentage losses ranging from about 10% to around 80%. Siliconized SiC tubes had upstream wall losses from approximately 20 to 33%, while sintered α-SiC had a value of about 16%, with the CVD SiC tube having the lowest value of 13%. The maximum Al_2O_3 tube wall loss was moderate, being around 15%, while the three types of sialon ceramic tubes had maximum wall thickness losses from about 20% to around 78%. The observed material losses from the upstream side of the tubes of this wide variety of ceramic materials demonstrate that under the high-temperature fluid basic coal-slag conditions employed in this exposure, none of these materials have sufficient corrosion resistance to serve for long time periods as HX surfaces unless very thick sections are employed in the HX design.

The mechanisms whereby these materials experience degradation in the presence of the coal slag appear to depend rather strongly upon the composition of the ceramic itself. The SiC based ceramics corroded via formation of phases at the ceramic-slag interface which were tentatively identified as iron and nickel silicides, with iron and nickel coming from the slag and the silicon presumably coming from the SiC. These phases form as small regions on the SiC surface by a process which produces a pit or channel in the SiC surface. These intermetallic type phases then become detached from the SiC surface and are transported into the fluid slag whereupon the smaller particles react with the slag and disappear. Development of the corrosion pits and channels in the outer surface of the SiC-based tubes results in substantial reductions in fracture strength of

most of these ceramics when the material is subsequently fractured at room temperature. The α-SiC exhibited the lowest reduction (—3%) in average fracture strength of all the SiC ceramics studied. Siliconized SiC specimens showed strength reductions from approximately 28 to 60%. The highly heterogeneous CVR SiC exhibited a modest strength reduction of 16%; however, the initial strength of this ceramic was the lowest of all the materials included in this experiment.

The AD 998 Al_2O_3 ceramic experienced wall thinning by a corrosion process in the coal slag via a mechanism quite different from that observed for the SiC-based materials. The Al_2O_3 ceramic-slag interface became uniformly coated with a phase rich in Al, Ni, and Fe, which appeared to be an Fe-Ni aluminate. This primary reaction product phase then reacted on the slag side with the fluid slag. The data suggest that continuous formation of the spinel phase on the Al_2O_3 surface and its dissolution in turn in the slag resulted in continuous transport of the aluminum in the Al_2O_3 into the slag. This process produced a microscopically rough surface on the Al_2O_3 which contributed to a fracture strength reduction of about 28% due to the slag exposure.

Exposure to the hot coal slag increased the room temperature helium permeability of all the surviving tubes by about one order of magnitude. The room temperature C-ring fracture strength for the five types of SiC and one type of Al_2O_3 ceramic decreased by about 3 to 60% due to the exposure. Siliconized types of SiC had strength reductions of approximately 38 to 61%. Sintered α-SiC showed the smallest strength reduction of 3%. The high purity Al_2O_3 had a strength loss of about 28%.

The thermal expansions of the SiC and Al_2O_3 based ceramics were essentially unchanged by long-term exposure to the fluid coal slag. This result is contrary to conclusions made earlier for SiC and Al_2O_3 ceramic specimens exposed to an acidic coal-slag environment. The earlier conclusions that these combustion gas exposures tended to cause increases in the thermal expansion were due to inaccuracies in the push-rod dilatometer employed. Measurements of specimens from the current experiment as well as those from CRAF Test 2 using a new differential push-rod dilatometer clearly show that the thermal expansion of these materials was unaffected by the exposure to either the acidic or basic coal slags.

ACKNOWLEDGMENTS

The authors express appreciation to James Hickerson of the Pittsburgh Energy Technology Center for his support in sponsoring this program at ORNL. Metals and Ceramics Division personnel whose contributions were particularly significant in making the work successful include: J. F. Willmering, for operating the CRAF; S. B. Waters and L. L. Hall for specimen preparation; W. H. Warwick for ceramography; and O. B. Cavin for x-ray diffraction. In addition, the assistance of H. W. Dunn and F. L. Ball in the Analytical Chemistry Division for scanning electron microscopy and electron microprobe analyses is also appreciated. Special thanks are expressed to J. I. Federer and C. S. Yust for reviewing the manuscript; and to K. F. Russell for figure preparation. In addition to these important contributions, major credit for the manuscript preparation is given to Margaret Manning, Fauna Stooksbury, and Felicia Foust who produced this report from our original draft.

REFERENCES

1. V. J. Tennery and G. C. Wei, *Recuperator Materials Technology Assessment,* ORNL/TM-7578, February 1978.

2. V. J. Tennery, *Economic Application, Design Analyses, and Material Availability for Ceramic Heat Exchangers,* ORNL/TM-7580, January 1981.

3. W. Kays and A. L. London, *Compact Heat Exchangers,* McGraw-Hill Book Company, New York, 1964.

4. M. Combs et. al., *High-Temperature Ceramic Heat Exchanger Development, Final Technical Report,* AiResearch Manufacturing Company of California Report 79-15721, Torrance, Calif., January 1979.

5. V. J. Tennery and M. K. Ferber, *Evaluation of Tubular Ceramic Heat Exchanger Materials in Acidic Coal Ash from Coal-Oil-Mixture Combustion,* ORNL/TM-7958, December 1981.

6. G. C. Wei and V. J. Tennery, *Evaluation of Tubular Ceramic Heat Exchanger Materials in Residual Oil Combustion Environments,* ORNL/TM-7578, March 1981.

7. A. Gatti and M. J. Noone, *Methods of Fabricating Ceramic Materials,* AFML-TR-77-135, General Electric Co., Philadelphia, December 1977.

8. G. K. Layden, *Development of SiAlON Materials,* CR-135290, United Technologies Research Center, East Hartford, Conn., December 1977.

9. Babcock and Wilcox, *Steam, Its Generation and Use,* 38th ed., New York, 1975, p. 15-1—15-26.

10. K. H. Jack, "X-Ray Data for SiAlONs and Other Nitrogen Ceramic Phases," unpublished data, Department of Metallurgy and Engineering Materials Crystallographic Laboratory, University of Newcastle Upon Tyne, England.

11. Joint Committee on Powdered Diffraction Standards, *Powder Diffraction File,* Swarthmore, Pennsylvania, 1979.

12. R. Perkins, *Reaction of Silicon Carbide with Fused Coal Ash,* Report EPRI AF-294, Electric Power Research Institute, Palo Alto, California, November 1976.

13. P. A. Gulbransen and S. A. Jansson, "The High Temperature Oxidation, Reduction and Volatilization Reactions of Silicon and Silicon Carbide," *Oxid. Metals* 4(3), 181–201 (1972).

14. G. Ervin, Jr., "Oxidation Behavior of Silicon Carbide," *J. Am. Ceram. Soc.* 41(9), 347–52 (1958).

15. S. A. Batdorf, "Fundamentals of the Statistical Theory of Fracture," pp. 1–30 in *Fracture Mechanics of Ceramics,* Vol. 3, ed. R. C. Bradt, D.P.H. Hasselman, and F. F. Lange, Plenum Press, New York, 1978.

INTERNAL DISTRIBUTION

1. Central Research Library
2. Document Reference Section
3–5. Laboratory Records Department
6. Laboratory Records, ORNL RC
7. ORNL Patent Section
8. P. F. Becher
9. R. A. Bradley
10. W. H. Butler
11. A. J. Caputo
12. P. T. Carlson
13. J. A. Carpenter, Jr.
14. J. V. Cathcart
15. G. M. Caton
16. W. R. Clark
17. J. H. DeVan
18. S. A. David
19. J. R. DiStefano
20. D. Easton
21. D. M. Eissenberg
22. J. I. Federer
23–27. M. K. Ferber
28. C. B. Finch
29. B. E. Foster
30. G. M. Goodwin
31. W. L. Greenstreet
32. J. P. Hammond
33–35. M. R. Hill
36. J. K. Huffstetler
37. J. E. Jones, Jr.
38. R. R. Judkins
39. C. C. Koch
40. W. J. Lackey, Jr.
41. C. J. McHargue
42. L. E. McNeese
43. A. J. Moorhead
44. R. K. Nanstad
45. P. L. Rittenhouse
46. A. C. Schaffhauser
47. M. Siman-Tov
48. G. M. Slaughter
49. J. O. Stiegler
50. G. M. Stocks
51–55. V. J. Tennery
56. R. J. Walsh
57. G. C. Wei
58. J. R. Weir, Jr.
59 M. H. Yoo
60. C. S. Yust
61. Alan Lawley (Consultant)
62. T. B. Massalski (Consultant)
63. R. H. Redwine (Consultant)
64. K. M. Zwilsky (Consultant)

EXTERNAL DISTRIBUTION

65. AIRESEARCH MANUFACTURING COMPANY, 111 South 34th Street, P. O. Box 5217, Phoenix, AR 85010

    David R. Richerson

66. AIRESEARCH MANUFACTURING COMPANY OF CALIFORNIA, 2525 W. 190th St., Torrance, CA 90509

    David M. Kotchick

67–68. ARGONNE NATIONAL LABORATORY, 9700 South Cass Avenue, Argonne, IL 60439

    Dave Kupperman
    Roger B. Poeppel

69. BABCOCK AND WILCOX COMPANY, P. O. Box 1260, Lynchburg, VA 24505

    Bill Long

70. BETHLEHEM STEEL CORPORATION, HOMER RESEARCH LABORATORY, Bethlehem, PA 18017

R. H. Herron

71. CARBORUNDUM COMPANY, P.O. Box 832, Niagara Falls, NY 14302

Robert Naum

72. COMBUSTION ENGINEERING, INC., P.O. Box 828, Valley Forge, PA 19482

J. R. Friedrichs

73. COORS PORCELAIN COMPANY, 600 9th Street, Golden, CO 80401

Donald W. Roy

74. DORNIER-SYSTEM GmbH, Postfach 1360, 7990 Friedrichshafen 1, Federal Republic of Germany

Gerd Willmann

75. ELECTRIC POWER RESEARCH INSTITUTE, 3412 Hillview Avenue, Palo Alto, CA 94304

W. T. Bakker

76. GAS RESEARCH INSTITUTE, 8600 West Bryn Mawr Avenue, Chicago, IL 60631

Charles J. Dobos

77. GENERAL ATOMIC COMPANY, P. O. Box 81608, San Diego, CA 92138

R. W. Schleicher

78. HAGUE INTERNATIONAL, 3 Adams Street, South Portland, ME 04106

John W. Bjerklie

79. HOT WORK INTERNATIONAL, 606 North Broadway, Lexington, KY 40408

John Newby

80. INDUSTRIAL PROGRAMS, OFFICE OF ASSISTANT SECRETARY, Conservation and Solar Energy, Forrestal Building, 1000 Independence Avenue, Room 2H085, Washington, DC 20585

James W. Osborne

81. KYOCERA INTERNATIONAL, INC., 8611 Balboa Avenue, San Diego, CA 92123

    Edwin H. Kraft

82. Leyda, W. E., 1192 Overlook Drive, Alliance, OH 44601

83. LOS ALAMOS NATIONAL LABORATORY, Los Alamos, NM 87545

    F. D. Gac

84. LUCAS RESEARCH CENTRE, Shirley Solihull, West Midlands B90 4JJ, England

    Roger Hunt

85. NORTON COMPANY, Industrial Ceramics Division, Worcester, MA 01606

    David P. Reed

86. ROCKWELL INTERNATIONAL CORPORATION, Rocketdyne Division, 6633 Canoga Avenue, Canoga Park, CA 91304

    Harry W. Carpenter

87. RUSTIN TURBINES, 3 Adams Street, South Portland, ME 04106

    Roger Lowder

88. Smith, R. L., P. O. Box 98, Chassell, MI 49916

89. SOLAR TURBINES, INC., P. O. Box 80966, San Diego, CA 92138

    Michael E. Ward

90. THERMAL TRANSFER, 1100 Roco Road, Monroeville, PA 15146

    Gordon L. Hanson

91. UKAEA, SPRINGFIELDS NUCLEAR POWER DEVELOPMENT LABORATORIES, Salwick Preston PR4 ORR, United Kingdom

    Peter Kennedy

92. UNITED STATES STEEL CORPORATION, 125 Jameson Lane, Monroeville, PA 15146

    Bill Vance

93. UNITED TECHNOLOGIES RESEARCH CENTER, 400 Main Street, East Hartford, CT 06108

D. J. McFarlin

94–95. DOE, OFFICE OF FOSSIL ENERGY, Technical Coordination Staff, Route Symbol FE 3, C-155-GTN, Washington, DC 20545

J. P. Carr
S. J. Dapkunas

96. DOE, IDAHO OPERATIONS OFFICE, 550 2nd Street, Idaho Falls, ID 83401

W. H. Thielbahr

97–98. DOE, OFFICE OF COAL UTILIZATION SYSTEMS, MS E-178, GTN, Washington, DC 20545

Jorgen Birkeland
T. K. Lau

99. DOE, MORGANTOWN ENERGY TECHNOLOGY CENTER, P.O. Box 880, Morgantown, WV 26505

J. M. Hobday

100. DOE, PITTSBURGH ENERGY TECHNOLOGY CENTER, P.O. Box 10940, Pittsburgh, PA 15236

James D. Hickerson

101–102. DOE, OAK RIDGE OPERATIONS OFFICE, P.O. Box E, Oak Ridge, TN 37830

E. E. Hoffman
Office of Assistant Manager for Energy Research and Development

103–129. DOE, TECHNICAL INFORMATION CENTER, OFFICE OF INFORMATION SERVICES, P.O. Box 62, Oak Ridge, TN. 37830